Zinc oxide nanophotonics - toward quantum photonic technologies

Sumin Choi

Submitted in total fulfillment of the requirements of the degree of Doctor of Philosophy

2016

School of Mathematical and Physical Sciences

University of Technology Sydney

Declaration of Authorship

I certify that the work in this thesis has not previously been submitted for a degree nor has it been submitted as part of requirements for a degree except as fully acknowledged within the text.

I also certify the thesis has been written by me. Any help that I have received in my research work and the preparation of the thesis itself has been acknowledged. In addition, I certify that all information sources and literature used are indicated in the thesis.

Signature of Student:

Date: 13/10/2016

Abstract

Zinc oxide (ZnO) is a large bandgap (3.37 eV at room temperature) semiconductor and is a good candidate for short wavelength photonic devices such as laser diodes. A large exciton binding energy (60 meV) at room temperature in addition to the advantages of being able to grow various nanostructure forms have made ZnO suitable for a wide range of applications in optoelectronic devices.

Driven by the rapid advance of nanophotonics, it is necessary to develop single photon sources (SPSs) and optical resonators in new class of materials. In particular, SPSs are required for a wide range of applications in quantum information science, quantum cryptography, and quantum communications. ZnO has been investigated for classical light emitting applications such as energy efficient light emitting diodes (LEDs) and ultraviolet (UV) lasers. Significantly ZnO has recently been identified as a promising candidate for quantum photonic technologies. Thus in this thesis the optical properties of ZnO micro- and nano-structures were investigated for ZnO nanophotonic technologies, specifically their applications in single photon emission and optical resonators.

Firstly, the formation of radiative point defects in ZnO nanoparticles and their photophysical properties were investigated. In particular, using correlative photoluminescence (PL), cathodoluminescence (CL), electron paramagnetic resonance (EPR), and x-ray absorption near edge spectroscopy (XANES) it is shown that green luminescence (GL) at 2.48 eV and an EPR line at g = 2.00 belong to a surface oxygen vacancy ($V_{O,s}^{+}$) center, while a second green emission at 2.28 eV is associated with zinc vacancy (V_{Zn}) centers. It is established that these point defects exhibit nanosecond lifetimes when excited by above bandgap or sub-bandgap (405 nm and 532 nm excitation wavelength) excitation. These results demonstrate that point defects in ZnO nanostructures can be engineered for nanophotonic technologies.

ZnO nanoparticles were consequently studied for the investigation of room temperature single photon emission from defect centers in ZnO nanoparticles. Under

the optical excitation with 532 nm green laser, the emitters exhibit bright broadband fluorescence in the red spectral range centered at 640 nm. The red fluorescence from SPSs in ZnO defect center is almost fully linearly polarized with high signal-to-noise ratio. The studied emitters showed continuous blinking; however, it was confirmed that bleaching can be suppressed using a polymethyl methacrylate (PMMA) coating. Furthermore, passivation by hydrogen treatment increase the density of single photon emitters by a factor of three.

ZnO/Si heterojunctions were fabricated and used to investigate electrically driven light emission from localized defects in ZnO nanostructures at room temperature. It is shown that excellent rectifying behaviors were observed with the threshold voltages at ~ 18 V and ~ 7 V for ZnO nanoparticles and thin film-based devices, respectively. Both devices exhibit electroluminescence (EL) in the red spectral region ranging from ~ 500 nm to 800 nm when 40 V and 15 V were applied to ZnO nanoparticles/Si and ZnO thin film/Si, respectively. The emission is bright and stable for more than 30 minutes, providing an important prerequisite for practical devices.

Finally, ZnO optical resonators were fabricated and investigated to enhance the visible light emission. Hexagonal ZnO microdisks with diameter ranging from 3 μm to 15 μm were grown by a carbothermal reduction method. Optical characterization of ZnO microdisks was performed using low temperature (80 K) CL imaging and spectroscopy. The green emission is found to be locally distributed near the hexagonal boundary of the ZnO microdisks. High resolution CL spectra of the ZnO microdisks reveal whispering gallery modes (WGMs) emission. Two different sizes (5 μm and 9 μm) of the ZnO microdisks were simulated to analyze the nature of light confinement in terms of geometrical optics. Respective analysis of the mode spacing and the mode resonances are used to show that the ZnO microdisks support the propagation of WGMs. The results show that the experimentally observed WGMs are in excellent agreement with the predicted theoretical positions calculated using a plane wave model. This work could provide the means for ZnO microdisk devices operating in the green spectral range.

Acknowledgements

First of all, I would like to acknowledge the Higher Degree Research at UTS, UTS International Research Scholarship for the travel funding and PhD program during my PhD candidature.

I would like to thank the technical support to all technical staff, Geoff McCredie, Katie McBean, Angus Gentle, Herbert Yuan, and Mark Berkahn for providing the important technical assistance with our experiments. Nothing would have worked well without you.

I would also like to thank Mark Lockrey, Olivier Lee, and Liangchen Zhu for their help using the cathodoluminescence characterization. They helped me a lot with the data collection of publishable results and analysis with the cathodoluminescence system. I wish to acknowledge Trong Toan Tran and Amanuel Berhane for their help with photoluminescence measurements. Thank you for collecting important results in quantum emitters in nanomaterials.

I would like to extend my thanks to our invaluable collaborators particularly Sevak Khachadorian, Christian Nenstiel and Axel Hoffmann at Technology of University Berlin. I appreciate your kindness for providing enormous data in the zinc oxide nanophotonics in Berlin. I also acknowledge the Australian Synchrotron beam line scientists for measurements of zinc oxide nanostructure, assisted by Bruce Cowie, Anton Tadich and Lars Thomsen.

I wish to express my sincere gratitude to research students and colleagues in Microstructural Analysis Unit for their useful discussions and research ideas: particularly Chris Elbadawi, Russell Sandstorm, Suranan Anantachaisilp and David McPherson. You guys made my stay at UTS enjoyable.

In particular, I would like to thank my supervisors A/Prof. Cuong Ton-That, Prof. Matthew Phillips and A/Prof. Igor Aharonovich for the continuous help with finance and the paper work during my study. Thank you for your efforts and time during my PhD candidature and I would never have been able to start and finish my PhD without

you guys. I have gained an enormous amount of thorough understanding in theoretical and experimental quantum photonics. You are my best mentor and outstanding supervisor.

Finally, I wish to thank my family, particularly Michelle Sun Min Lee who always supported me throughout my PhD study. Nothing would have been possible without you. This thesis is dedicated to you.

Contents

List of Figures

List of Tables

Abbreviations

APD – avalanche photo diode

ASE – amplified spontaneous emission

CB – conduction band

CCD – charge coupled device

CL – cathodoluminescence

CW – continuous wavelength

DAP – donor-acceptor pair

DFT – density functional theory

DL – deep-level

EL – electroluminescence

EPR – electron paramagnetic resonance

ESR – electron spin resonance

FPMs – Fabry-Pérot modes

FWHM – full width at half maximum

GL – green luminescence

HBT – Hanbury Brown and Twiss

LDA – local density approximation

LED – light emitting diode

LPB – lower polariton branch

NBE – near-band edge

PL – photoluminescence

PMMA – polymethyl methacrylate

RL – red luminescence

SEM – scanning electron microscope

SPSs – single photon sources

sccm – standard cubic centimeters per minute

TEM – transmission electron microscopy

TCSPC – time correlated single photon counting

UPB – upper polariton branch

UV – ultraviolet

VB – valence band

W-H – Williamson-Hall

WGMs – whispering gallery modes

XANES – x-ray absorption near edge spectroscopy

XRD – x-ray diffraction

YL – yellow luminescence

ZPL – zero phonon line

Chapter 1

Introduction

In the past decade, the search for a solid-state nanophotonics platform has intensified. Among promising candidates like diamond and SiC, zinc oxide (ZnO) has been utilized for several cutting edge experiments in quantum optics and integrated nanophotonics [1]. ZnO has a direct bandgap of 3.37 eV at room temperature with a large exciton binding energy of 60 meV. The higher binding energy significantly enhances the efficiency of light emission at room temperature where practical devices operate. Consequently, it is no surprise that for many years ZnO has been the focal point of light emitting device studies. ZnO also exhibits excellent thermal conductivity and radiation hardness far exceeding that of GaN [2].

ZnO has a large number of intrinsic and extrinsic deep-level (DL) impurities and complexes that emit light of different colors, including ultraviolet (UV), blue, green, yellow, orange, and red [3-7]. The possibility to obtain luminescence across the visible spectral range from ZnO has great potential for the development of white light emitting diodes (LEDs), especially in its nanostructured form. As a result, it is currently attracting extreme global interest for nanophotonic device applications [8]. The luminescence spectrum of most ZnO samples shows a near-band edge (NBE) UV emission accompanied by a broad visible luminescence typically centered at around 510 nm. It is important to understand the origin of the visible emissions related to DL defects in ZnO for the development of efficient optoelectronic devices. The origin of the NBE was attributed to bound exciton complexes and their phonon replicas [9]. Visible luminescence is due to DL defects, such as zinc interstitials (Zn_i) or oxygen vacancies (V_O). Unfortunately, however, the chemical origin of these luminescence centers, especially the green and red emission, is not understood clearly and is a controversial topic requiring more investigation. Many studies have highlighted the

effects of the large surface-to-volume ratio in low dimensional structures, suggesting that the surface defect concentrations may be very large [10]. Reliable control of the optical properties of ZnO nanoparticles needs to be achieved to even broaden their use in light emitting devices.

1.1 ZnO for quantum applications

Given the importance of photons in generating spatially extended quantum states and the need for new sources of quantum light, this thesis is specifically focused on single photon sources (SPSs). Thus, the need to characterize defects in ZnO is further amplified with the recent applications of ZnO as host of SPSs for quantum technologies [11, 12] and their use in random lasing other advanced sensing technologies [13]. SPSs that generate non-classical states of light have been extensively explored over the past decade due to a variety of applications, including quantum cryptography, quantum computation, and metrology [14-16]. The use of SPSs in a quantum information application requires that there is only one photon in a specified spatial and partial mode.

In parallel to developing the SPSs, research into engineering of optical resonators had intensified [17-20]. ZnO has a modest refractive index $n = \sim 2$ in visible spectral range. However, an advantageous feature of ZnO is the ability to be grown in a variety of nano-structured geometrical shapes. Realization of different morphologies from ZnO nanostructures is pivotal for the development of nanotechnology devices, particularly these for high efficiency lighting solutions. These nanostructures show intense emission even at high temperatures, and the emission can be easily tailored due to their large surface-to-volume ratio, thus providing building blocks for nano-scale electronic components. The growth procedures for high quality ZnO have been already developed and are currently being used in industry, indicating that high quality crystalline ZnO can be manufactured easily and cheaply. In addition, ZnO has excellent piezoelectric and electrical properties [21-23]. Among various kinds of optical resonators, cavities that support whispering gallery modes (WGMs) are

particularly interesting due to their ease of fabrication. They have been widely used to study light matter interaction, non-linear processing and other nanophotonics phenomena in ZnO [24, 25]. Other family of cavities, including photonic crystals, are only emerging, and are not as established as cavities involving Si or GaAs [26, 27].

Recently, it has been demonstrated that electrically driven light emission can be realized with homo- and heterojunction nanostructures, where carrier injection occurs across the p-n junction. The controlled fabrication of ZnO SPSs, together with a recent emission enhancement by coupling the light to plasmonic structures or cavities, is expected to progress the technology beyond the current state of the art and enable low threshold lasers, integrated quantum photonics and other practical quantum information and metrology devices. However, engineering efficient SPSs excited by electrically from ZnO is challenging and requires sophisticated fabrication conditions and optimization of implantation of the single emitting defects. The greatest challenge for ZnO remains the fabrication of reliable, low resistivity, and stable p-type ZnO. As-grown ZnO is highly n-type so it has been a matter of wide investigation and research [2, 7, 28, 29] and in particular defects such as Zn_i and V_O which can compensate the acceptors. The main problem is to consistently produce stable p-doped ZnO, and it presents the core focus of current research. As a result, most of the current developed devices are based on heterojunctions [30, 31]. Excellent properties of ZnO can be best employed by building heterojunctions with other p-type semiconductors. Therefore, the growth of n-type ZnO on other p-type materials could offer an alternative way to realize ZnO-based p-n heterojunctions.

1.2 Aim of the research and thesis structure

The origin of visible luminescence in ZnO is still a subject under considerable debate and there are many open questions about the nature of single photon emission from ZnO. The general aim of the project is to study optical properties of ZnO for quantum nanophotonic applications.

The specific aims of this dissertation are summarized below:

- Identification of chemical origin of luminescent point defects in ZnO nanostructures using electron paramagnetic resonance (EPR), x-ray near absorption edge spectroscopy (XANES), x-ray diffraction (XRD), cathodoluminescence (CL), and photoluminescence (PL) spectroscopy
- Investigation of characteristics of single photon emission from ZnO nanostructures
- Fabrication of n-ZnO/p-Si heterostructures and generation of electrically driven light emission from the heterostructures, and
- Investigation of optical resonance from ZnO microstructure using CL spectroscopy.

Chapter 2 provides an introduction to ZnO and its physical and optical properties are briefly summarized. The generation mechanisms of ZnO SPSs are studied before ZnO can be used as a promising quantum platform. Then, a comprehensive range of topics pertaining to resonance in optical cavities, including WGMs, Fabry-Pérot modes (FPMs), polaritons is reviewed. Electrically pumped lasers, random lasing, and heterostructures using photonics in ZnO are also discussed.

Chapter 3 presents the experimental methodologies and setup involved in this thesis. A range of ZnO samples which have been synthesized and processed under different conditions will be studied. Those growth techniques and processes of heat treatment such as carbothermal reduction and annealing process are also described. Then characterization techniques such as CL and confocal microscopy to understand the ZnO nanophotonics are presented.

In chapter 4, photophysics of point defects in ZnO is discussed. Before SPSs in the visible luminescence from ZnO are studied, it is important to understand their generation mechanisms in ZnO nanostructures. This chapter is mainly devoted to investigations on the luminescence properties of ZnO nanoparticles. The control of the optical emission of ZnO nanoparticles through different annealing temperature and

atmospheres, and the structural quality after the annealing processes in the nanostructures are described. The results of correlative characterization techniques are discussed to investigate the point defects in ZnO nanoparticles, using EPR spectroscopy and XANES.

Chapter 5 reports single photon emission from ZnO nanoparticles. It presents how the SPSs are generated and observed by using the confocal microscopy. Then luminescence properties and the photon statistics of the SPSs in ZnO are described. The stability and the density of SPSs were found to be major issues in this thesis, so controlled ways to improve the stability and to increase the density of the emitters are discussed.

Chapter 6 describes novel approach to generate electrically driven light emission using ZnO which exhibits SPSs under the optical excitation. It focuses on the fabrication of heterostructure devices using n-type ZnO and p-type Si. The fabrication method of the heterojunctions is clearly presented, and its electrical and optical properties are discussed. The stability and photon statistics of the devices are investigated and potential integration in future is briefly commented on.

Observation of optical resonance from ZnO microcavities is presented in chapter 7. A fabrication technique of different sizes of ZnO microdisks is described and the CL characterization to observe those optical resonances are discussed. Using a plane wave model, theoretical calculations and experimentally observed CL spectra are compared to analyze the nature of the optical resonances.

Finally, chapter 8 concludes the thesis and future work is presented.

Chapter 2

Fundamentals of ZnO as a nanophotonic material

In this chapter the recent advances in studying single emitters in ZnO, engineering of optical cavities and practical nanophotonic devices including nano-lasers and electrically driven devices will be reviewed. This chapter is divided into four parts; (1) ZnO material which provides a review of the structural, physical, and optical properties of ZnO, (2) investigation of single photon emission from ZnO, (3) ZnO optical resonators, and (4) nanophotonic devices from hybrid or heterostructures using ZnO.

2.1 ZnO

2.1.1 Crystal structure of ZnO

Crystalline ZnO exists in the wurtzite, zinc blende, and rocksalt structure, with the most common form being the hexagonal wurtzite structure at ambient conditions. The wurtzite structure is a compact hexagonal structure at the base, the first neighbors are atoms of the other species and are placed on vertices of tetrahedron, and the second neighbors make the hexagonal structure. The crystal can be seen as many alternating planes composed by Zn^{2+} tetrahedrons and O^{2-} tetrahedrons along the *c*-axis, with lattice parameters $a = 0.35$ nm and $c = 0.52$ nm. A diagram of the unit cell is shown in Figure 2.1.

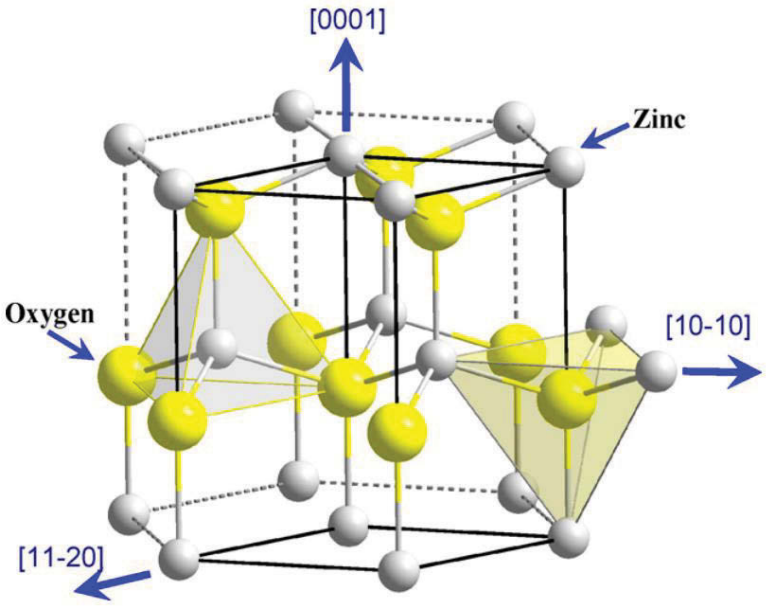

Figure 2.1. ZnO crystalline wurtzite structure. Directions of [0001], [11$\bar{2}$0], and [10$\bar{1}$0] and indicated. The lattice constants are a = 3.25 Å and c = 5.20 Å [10].

The c-plane (0001) of the wurtzite structure consists of alternating Zn^{2+} and O^{2-} layers leading to polarity along the c-axis, so the c-plane faces are polar and are terminated by either Zn or O ions. Contrary, the a-plane (11$\bar{2}$0) contains equal numbers of Zn^{2+} and O^{2-} atoms, making the a-axis non-polar, sp^3 orbital hybridization leads to a tetrahedral geometry [32] in which each Zn atom is bound to four O atoms and vice versa. The tetrahedron of the sp^3 bonds is slightly distorted, leading to an axis ratio of c/a = 1.602 for ZnO compared to c/a = 1.663 for ideal case [33].

2.1.2 Band structure of ZnO

ZnO is a direct bandgap semiconductor. The bandgap (E_g) of ZnO shows a temperature dependence that can be described by Varshni's formula: [34]

$$E_g(T)=E_g(0)-\frac{\alpha T^2}{T+\beta} \tag{2.1}$$

where $E_g(T)$ is temperature dependent energy gap, $E_g(0)$ is an energy gap at 0 K, T is an absolute temperature. α and β have empirically determined material constants with values of 5×10^{-4} eV/K and 900 K, respectively [21], where α represents the $T \rightarrow \infty$

limit of the gap entropy, so called the strength of electron-phonon coupling. At 300 K, the bandgap of ZnO is 3.37 eV which corresponds to a wavelength of 368 nm.

A complete understanding of the energy band structure of ZnO is important, in order to properly utilize the material in various optoelectronic device applications. The band structure of ZnO was first calculated in 1969 using Green's function [35] and followed up soon after with experimental results from x-ray induced photo-emission spectroscopy and UV photoemission measurements. The results were controversial and remained contradictory for many years [7, 36, 37]. More recently, advances in the computational power provided by advanced code and computers has allowed for the most detailed calculation of the structure of ZnO to date, using the linear-muffin-tin-orbital method [37].

2.1.3 Electronic properties of ZnO

Crystalline ZnO has a wide bandgap of 3.37 eV and an exciton binding energy of 60 meV at room temperature. The fraction of excitons at a given temperature is given by

$$N_{ex}(T) = 1 - e^{-\frac{E_{bx}}{kT}} \tag{2.2}$$

where N_{ex} is the fraction of excitons, E_{bx} is the binding energy of the exciton, k is the Boltzmann constant.

The thermal energy at room temperature is equivalent to 25 meV, compared to the GaN exciton binding energy of 21 meV [38]. Therefore, the probability of a GaN exciton being dissociated by thermal energy at room temperature is undesirably high compared with ZnO. This places a hard limit on the efficiency of future GaN-based optoelectronic devices. The exciton binding energy of ZnO on the other hand is 60 meV, considerably higher than that of room temperature. That means ZnO excitons will be significantly more abundant at 300 K and will remain bound at much higher temperature than GaN and extremely high optical emission can be achieved at room temperature and above (up to about 500 °C). At room temperature, the percentage of excitons that have been thermalized is 38 % for GaN and 10 % and for ZnO, so 90 % of excitons are still present in ZnO at room temperature. This clearly indicates why

ZnO may be the preferred choice for future optoelectronic devices. Moreover, since ZnO has a direct bandgap, this allows direct electron-hole recombination without requiring momentum conservation via phonon production. This greatly enhances the optical efficiency of the material and sets it apart from indirect semiconductors such as Si.

2.1.4 Defects in ZnO

Defects play a fundamental role in semiconductors. Defects are always presents as intrinsic point defects, dislocations and impurity atoms. They alter the electrical and optical properties of semiconductors, so it is essential that they are identified, understood and controlled during growth and processing. Therefore, it is critical to understand the behavior and incorporation of the point defects in ZnO for its successful application in nanophotonic devices.

The possible intrinsic native defects in ZnO are V_O, zinc vacancy (V_{Zn}), oxygen interstitial (O_i), Zn_i, oxygen antisite (O_{Zn}), and zinc antisite (Zn_O). This is in addition to native defect clusters, which are usually formed by the combination of two point defects or one point defect and one extrinsic element, e.g., a $V_O^{2+} V_{Zn}^{2-}$ cluster formed by Zn_i and V_O.

Defects often introduce levels within the bandgap of semiconductors [39, 40]. These defect levels include transitions between different charge states of the same defect, and can be estimated from the formation energy calculations. Based on density functional theory (DFT) within the local density approximation (LDA) and the LDA+U, first principles calculations have been extensively used to analyze the charge states, formation energies and migration barriers of native point defects in ZnO [41]. The electronic levels of the native defects in ZnO are shown in Figure 2.2. The stable charge state of the defect depends on the position of the Fermi level with respect to the energy level. The formation energies of native defects also depend heavily on Fermi level as well as growth conditions. Figure 2.3 shows the corrected formation energies for the relevant native point defects in ZnO depending on the Fermi level position. The kinks in the lines for a given defect are transitions between different charge states.

Donors and acceptors have reduced formation energies in p-type ZnO and n-type material, respectively. At thermodynamic equilibrium and in dilute cases that means no defect-defect interaction, the concentration of a point defect (c) follows a Boltzmann distribution [41] and is given by

$$c = N \times e^{-\frac{E^f}{kT}} \tag{2.3}$$

where E^f is the formation energy and N is the number of sites that the defects can be incorporated on. The above equation indicates that defects with low formation energies will occur in high concentrations. The Fermi level of a point defect is variable and is dependent on the growth or annealing conditions [42]. For instance, the formation energy of an Vo depends on the abundance of O and Zn atoms in the growth environment. Among the defects that behave as donors, Vo have the lowest formation energy (Figure 2.3), indicating that Vo and V_{Zn} are thermodynamically expected to most abundant defects in ZnO under equilibrium conditions.

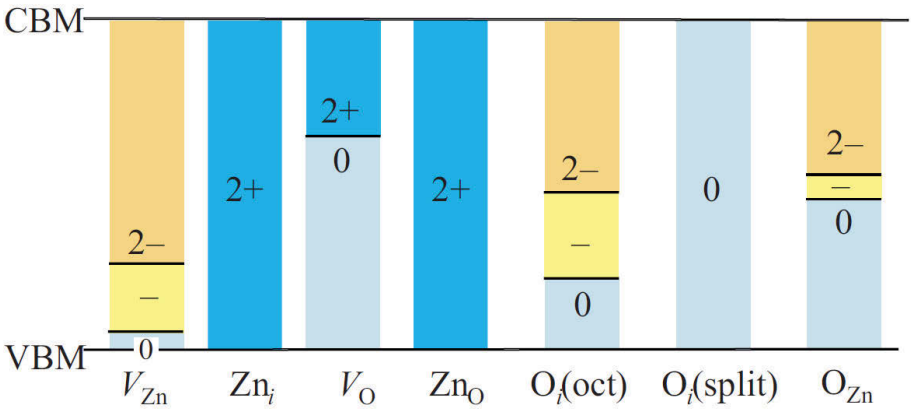

Figure 2.2. Thermodynamic transition levels for defects in ZnO. These values are corrected based on the LDA and LDA+U calculations [41].

Generally, native defects are related to the compensation of the principal donor or acceptor dopants. Donor defects are easily formed in n-type material while acceptor defects are formed in p-type material, responding to the dominant conductivity type. Since ZnO often shows unintentional n-type properties, native defects in ZnO have been considered to play an important role. This fact highlights the major challenge in

research on ZnO as a semiconductor to achieve p-type material. The theoretical open problem is to understand how N, P, As, and Sb form acceptors and which lattice site each dopant occupies.

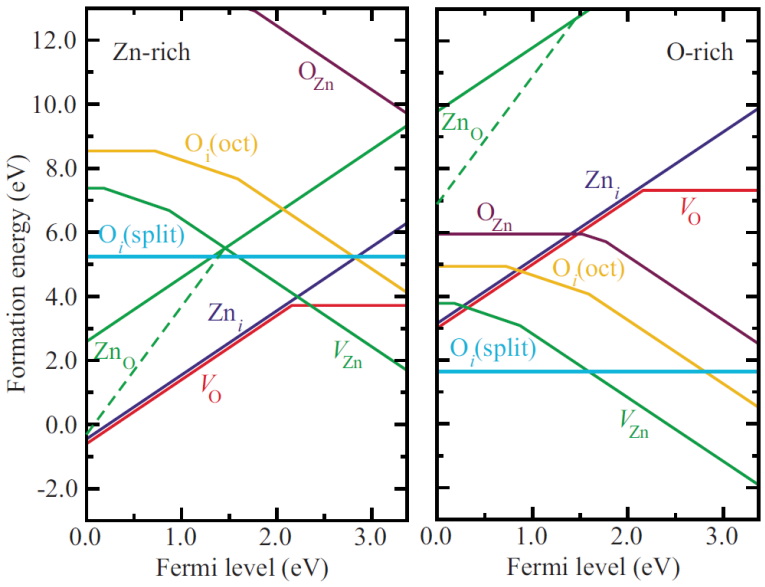

Figure 2.3. Formation energies as a function of Fermi level position for native point defects in ZnO. The slope of the line represents the stable charge state of the defects [41].

2.1.5 Optical properties of ZnO

The optical emission consists of a UV peak and a broad visible band. The UV peak is also called the NBE emission, which manifests as a relatively sharp peak in the UV region (~ 3.3 eV); and the broad visible band is called DL emission which is a broad peak in the visible region (1.5 eV – 3 eV), due to transitions involving defects or impurity state [7]. The UV peak is attributed to the recombination of free and bound excitons. The exact chemical origin of the visible DL luminescence is still unknown and is currently an area of active research interest. There is, however, general agreement that visible portion of the emission spectrum is caused by DL defect states in the crystal lattice.

2.1.5.1 Near-band edge (NBE) emission

NBE emission usually occurs by a recombination of free excitons, as well as donor and acceptor bound excitons, along with the longitudinal optical phonon replica modes of these transitions in high quality bulk ZnO. In high resolution luminescence spectra, free exciton emission in ZnO occurs at approximately 3.374 at 4 K [43].

The different recombination channels are shown in Table 2.1, where E_g is the bandgap of the material, E_x is the exciton binding energy, E_D is the energy of the donor levels measured from the bottom of the conduction band (CB), E_A is the energy of the acceptor levels measured from the top of the valence band (VB), and the term $\frac{q^2}{4\pi\varepsilon_0\varepsilon_r R_{DAP}}$ describes a Coulombic interaction between the electron and hole in donor-acceptor pair (DAP) recombination [7].

Recombination channel	Energy transition	Notation
Band-to-band recombination	$E = E_g$	
Free-exciton	$E = E_g - E_x$	FX
Neutral donor bound exciton	$E = E_g - E_x - E_D$	D^0X
Neutral acceptor bound exciton	$E = E_g - E_x - E_A$	A^0X
Donor to free hole	$E = E_g - E_D$	D^0, h
Free electron to acceptor	$E = E_g - E_A$	e, A^0
Donor-acceptor pair	$E = E_g - E_D - E_A + \frac{q^2}{4\pi\varepsilon_0\varepsilon_r R_{DAP}}$	DAP

Table 2.1. Radiative recombination channels by excitation of electron-hole pair.

The recombination of the bound excitons will lead to an emission with energy characteristic of the defect (impurity) ionization energy. Lower energy emission peaks with decreasing intensity occur due to longitudinal optical phonon replicas separated by 72 meV [44]. At energy from 3.31 eV – 3.34 eV, high resolution spectra may also reveal two electron satellite transitions due to recombination of excitons at neutral donors leaving the donor in an excited state [43].

2.1.5.2 Defect-related deep-level (DL) emissions in ZnO

Defects in ZnO can strongly affect the electrical and optical properties of ZnO, including minority carrier lifetime, luminescence, and doping characteristics, and thus they are directly involved in the nanophotonic device properties. The DL band in ZnO mainly contains green, yellow, and red contributions. The emission can occur as the result of either native defects or unintentional impurities, with point defects such as V_O or V_{Zn}, along with Cu interstitial, being investigated thoroughly.

Red band have mostly been observed in ZnO single photon emission. A red luminescence (RL) peak is observed in ZnO at 1.7 eV – 1.9 eV with a full width at half maximum (FWHM) of 0.5 eV [7], however, this peak is reported less frequently than the green luminescence (GL) or yellow luminescence (YL). The emission at 1.9 eV was attributed to transitions associated with O_i [45], and the orange-red emission at 1.7 eV was suggested to be due to transitions related to V_{Zn} complexes [46]. Experimental results associate this luminescence with O-rich conditions [47] and RL has been assigned to transitions involving V_{Zn}, and Zn_i [48]. Additionally, crystal field splitting of levels in transition metal impurities can lead to internal transitions emitting a red emission, consisting of sharp peaks. Alvi et al. studied a red emission at 1.75 eV and suggested that it may be attributed to the transition from V_O level to top of the VB in ZnO [49]. The calculated energy level of the V_O in ZnO is 1.62 eV below the CB based on the full-potential linear muffin-tin orbital method [50].

ZnO exhibits yellow band centered at around 2.0 eV – 2.2 eV with a FWHM of 0.5 eV [7]. This emission has been attributed to transitions involving O_i acceptors [51]. Another explanation is the presence of Li which is present in ZnO grown by hydrothermal methods where Li compounds have been used in the growth process [52]. ZnO nanorods grown by chemical methods also exhibited YL which was attributed to a $Zn(OH)_2$ group attached to those surface [53]. At low temperatures the YL has been assigned to donor-acceptor recombinations between shallow donors and deep Li_{Zn} that introduce deep acceptor levels (~ 0.8 eV above VB minimum) [54, 55] into the bandgap.

The green band of the visible portion of the ZnO emission is most frequently observed in luminescence spectra in ZnO, which is centered at around 2.4 eV with a FWHM of 0.4 eV [7]. This green emission of ZnO has been assigned to a wide range of defects including Zn_i [51], V_{Zn} [41] V_O [56], Zn_O [57] as well as extrinsic impurities such as Cu impurities [58]. Cu is a major trace impurity in Zn metal used as a precursor material in ZnO growth accounting for the large number of reports on the structured GL band. Conversely, following the works of Vanheusden et al., the GL was attributed to transitions from singly ionized oxygen vacancies (V_O^+) [59]. The chemical origin of the GL is still open and controversial, but there is strong experimental evidence that it is located at the surface.

The intensity of these visible emission lines can be manipulated by thermal annealing, doping or plasma processes that can modify the defect states. For instance, Li-in-diffusion doped ZnO produces yellow emission at 2.2 eV [53] and Cu-doping ZnO contributed wide green emission with a sharp zero photon line (ZPL) and a broad phonon sideband below 80 K [60]. However, controllably engineering particular defect centers in ZnO is still challenging. Although the clear origins of the colorful emissions have not yet been elucidated, the suppression of them is possible. Several possible levels of the visible emission in ZnO are summarized in Figure 2.4.

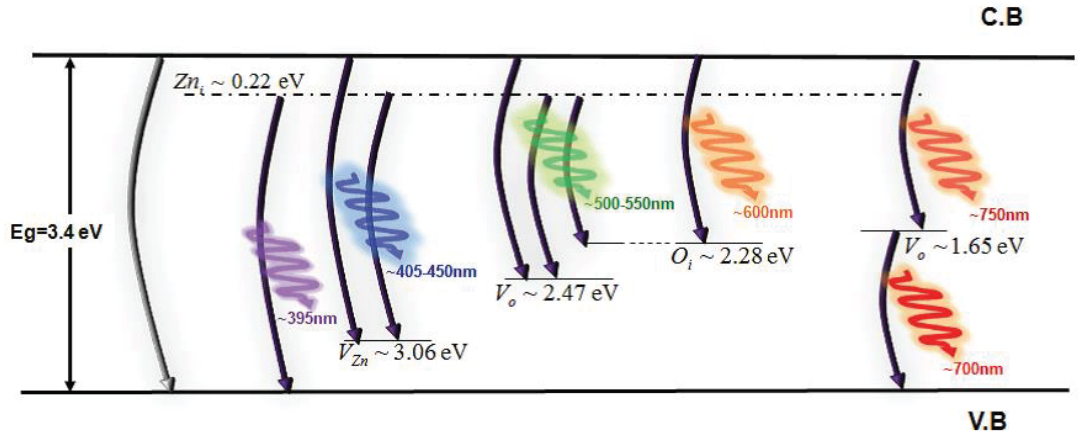

Figure 2.4. Schematic band diagram of the DL emissions in ZnO based on the reported data [49].

2.2 Single photon emission from ZnO for quantum photonics

As discussed above, ZnO has a characteristic emission spectra comprising of the UV emission and the broad defect-related band occurring at visible. So far, SPSs have only been identified in the red spectral range. This section describes the generation of ZnO SPSs that have been demonstrated by antibunching characteristics and their statistics.

Numerous color centers related to the defects or impurities have been studied in ZnO, so this material can offer many potential candidatures for SPSs covering emission in the visible or near infrared spectral range. At present SPSs, ZnO have been observed at ranging from 1.56 eV to 1.9 eV. Commonly SPSs from ZnO are observed under the green laser optical excitation. Morfa et al. first reported the generation of single photon emission through antibunching, bunching and spectral measurements from ZnO defects [11]. SPSs were induced by thermal annealing of ZnO nanoaprticles or thin films to 500 °C in air to induce the formation of color centers that produces a bright red fluorescence [61]. Single photon emission characteristics were characterized using confocal microscopy at room temperature under ambient conditions. Figure 2.5(a) shows a typical confocal microscopy setup for the ZnO samples obtained by 532 laser excitation. The emitted light passes through a 50/50 beam splitter and is detected by one of two avalanche photo diodes (APDs). A time correlated single photon counting (TCSPC) module measured the delay between consecutive photon detections at each APD. Second order correlation function ($g^2(\tau)$) measurements were taken on the ZnO with an optical fiber-coupled Hanbury-Brown and Twiss (HBT) setup to identify SPSs, while the PL spectral were collected. Figure 2.5(b) shows a typical confocal map of the ZnO nanopowder using a 532 nm excitation laser. Several bright spots (D1 and D2) and visible and correspond to localized bright fluorescent defects.

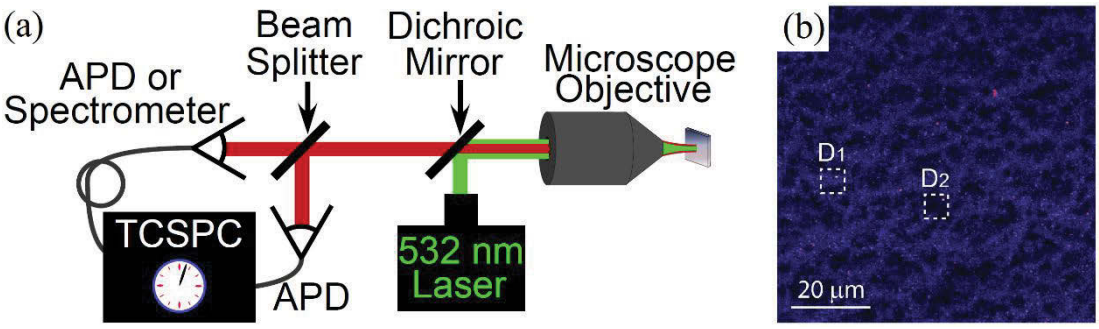

Figure 2.5. (a) Schematic of a confocal microscope used to detect single emitters. Sub-bandgap green laser excites localized single emitters and the emitted light is detected by an APD or a spectrometer. A TCSPC module enables measurement of $g^2(\tau)$ for confirmation that a single emitter is being identified [12]. (b) Typical scanning confocal fluorescence map of ZnO illuminated with 532 nm continuous wave (CW) light. Locations marked 'D1' and 'D2' identify the SPSs [11].

Representative antibunching data for the two ZnO different samples are shown in Figure 2.6(a) and 2.6(b). The $g^2(\tau)$ can be expressed as a following the equation:

$$g^2(\tau) = \frac{\langle I(t)I(t+\tau)\rangle}{\langle I(t)\rangle^2} \tag{2.4}$$

which describe the probability of defecting a photon at a delay time, τ, given that a photon was detected at time, t, recorded from the same emitter using the HBT configuration. The degree of $g^2(\tau)$ directly provides information of statistics of emitted photons and determines if the emitted photons are true SPSs. For an ideal SPSs, $g^2(\tau) = 0$. As can be seen from Figure 2.6(a) and 2.6(b), the pronounced antibunching dip in in the photon statistics at zero delay time indicates that the emission originates from a single photon emitter. The deviation from 0 at $g^2(0)$ is attributed to the overall background luminescence.

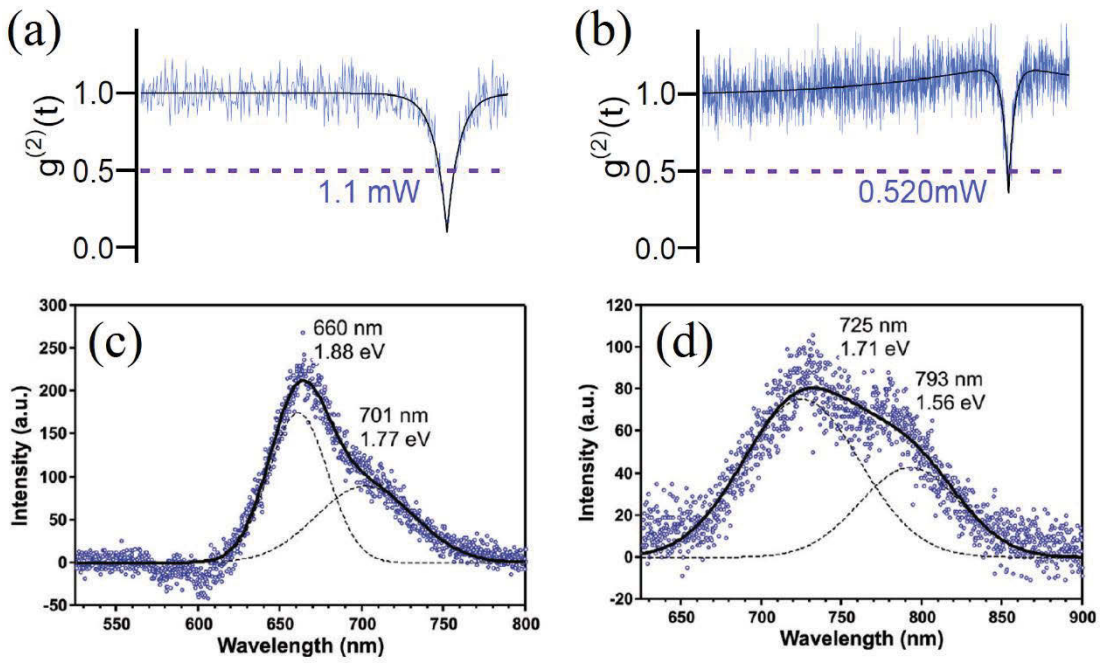

Figure 2.6. Characterization of single photon emitters in ZnO. (a, b) Representative $g^2(\tau)$ curves from 2 different defects obtained from different laser powers. In each curve, the antibunching dip at ($g^2(0) < 0.5$) is observed, verifying that single defects are being studied. Note in (b) that as laser power increases the antibunching dip sharpens and bunching behavior ($g^2(\tau) > 1$) is evident, indicating three-level system exist [12]. (c, d) Background subtracted single defect fluorescence showing two broad emission lines. The dash lines are fit by Gaussian function to each emission line, while the thick black line is the sum of the two Gaussian peaks [11].

The PL spectra from two different single emitters are shown in Figure 2.6(c) and 2.6(d). The dashed lines in Figure 2.6(c) and 2.6(d) are Gaussian functions to fit for each emission line. For the left sample, the emissions are observed at 1.71 eV and 1.56 eV. The blue-shifting of the emission from 1.56 eV (lower peak from the right) to 1.88 eV (higher peak to the left) can be explained by a changed CB level resulting from charge accumulation at the surface. It has been speculated that the mechanism involves the emission from the CB to V_{Zn} trap. Other groups found the single photon emission ranging from around 1.55 eV to 2.21 eV. Jungwirth et al. measured 19 different defects in ZnO [12] and about 30 defect center locations have been investigated by Neitzke et al. [62]. They obtained antibunching curves with similar spectral range. The emission

spectra of each study differ so it is difficult to assign the origin of the single emitters. Ten of the 16 spectra investigated by Jungwirth et al. are well characterized by two Gaussian distributed peaks separated by roughly 150 meV [12]. They found the location of the energy peak to be in the range of 1.82 eV – 1.97 eV for one of two peaks and 1.91 eV – 2.08 eV for the other peak. Single photon emission has also been observed from sputtered ZnO thin film, which is promising for quantum applications because sputtered films can be quickly and easily engineered and thus can be readily integrated for quantum photonics [12]. Sputtered ZnO thin films showed single emitters at ~ 1.9 eV which can be attributed to similar defect centers from ZnO nanoparticles.

Investigation of isolated defects through a HBT interferometer also provides new quantitative information. The lifetime of the SPSs can be deduced from fitting the $g^2(\tau)$ to the following equation:

$$g^2(\tau) = 1 - e^{(-\tau_1/\tau)} \tag{2.5}$$

at low excitation powers, where τ_1 is the decay rate of the emitter. The calculated lifetime of the single emitters of ZnO ranges from 1.7 ns to 13 ns, which are comparable with other single defects in solids [63]. In particular, the photon statistics of the single emitters can be described with a frame of a two- or three-level system [64]. For the three-level system, at high excitation powers, bunching behavior is observed indicating the presence of a metastable (shelving) state. While the $g^2(\tau)$ curve in Figure 2.5(a) shows antibunching behavior only, the $g^2(\tau)$ in Figure 2.5(b) exhibits a pronounced bunching behavior, indicating emission occurs via three-state mechanism. In this case, $g^2(\tau)$ is fit to three-level system which has two exponential components following the equation:

$$g^2(\tau) = 1 - (1 + a)\, e^{(-\tau_{21}/\tau)} + a\, e^{(-\tau_{23/31}/\tau)} \tag{2.6}$$

where τ_{21} and $\tau_{23/31}$ are decay rates for radiative and the metastable states, respectively. A source for which $g^2(0) > 1$ is described as bunched since there is an enhanced probability of two photons being emitted within a short time delay. The calculated decay rates correspond to radiative lifetimes ranging from 1 ns to 5 ns and non-

radiative lifetimes ranging from 40 ns to 429 ns, respectively. Jungwirth et al. showed that 7 of the 14 nanoparticle-based defects studied displayed signs of bunching which one of 5 sputtered film defects exhibited bunching behavior [12]. Some of the emitters did not exhibit bunching behavior despite high excitation power. The two-level nature of selected emitters could be a significant system for metrological applications, because the $g^2(\tau)$ does not exhibit bunching even at saturation.

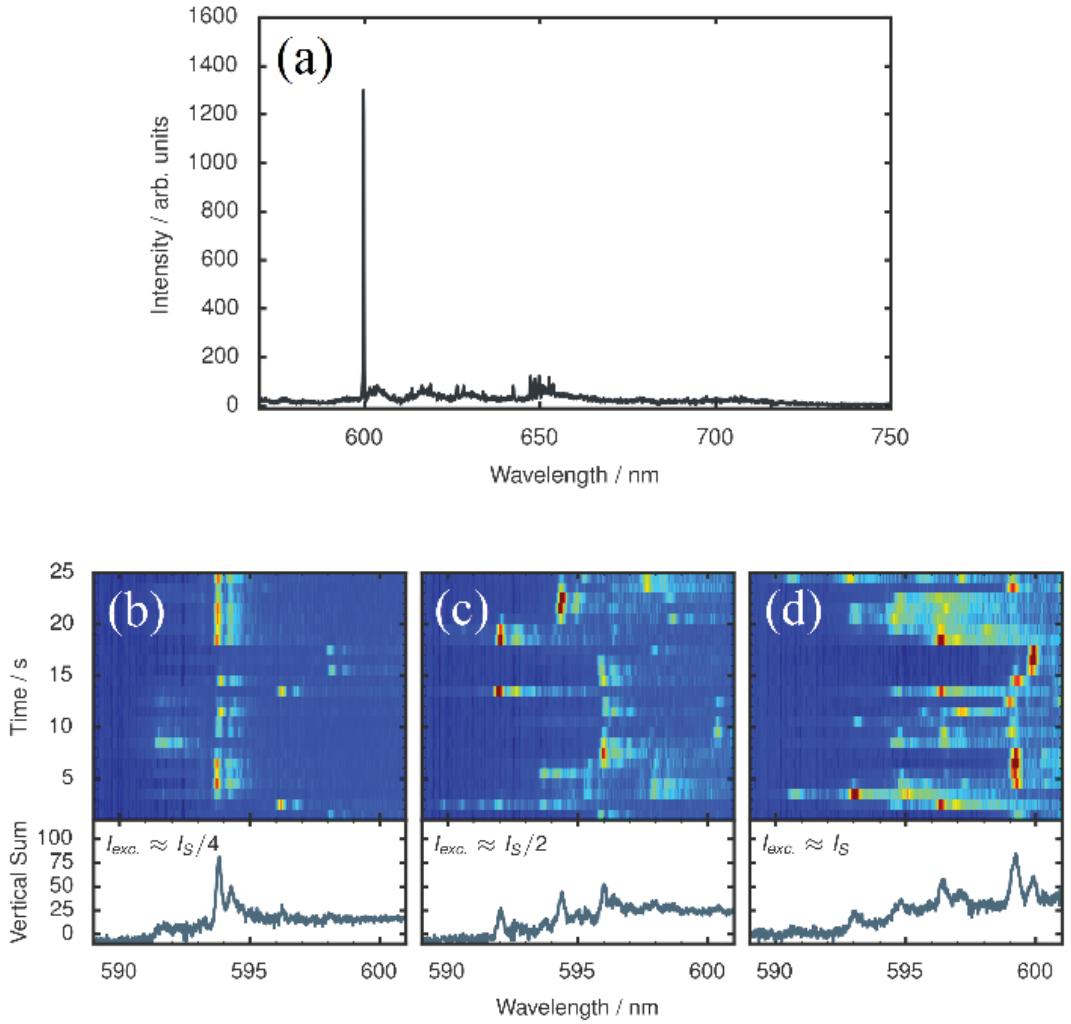

Figure 2.7. (a) PL spectrum that emits SPSs from the optical ZPL transition at 5 K. (b-d) Power dependent spectral jumps of the ZPL of three different ZnO defect centers at excitation intensities [62].

For a clear understanding of the ZnO defects, low temperature PL measurements were performed by Neitzke et al. [62]. Sixteen defects from the same ZnO sample were

investigated at 5 K. Figure 2.7(a) shows a typical PL spectrum of the defect, consisting of a sharp ZPL and a phonon sideband. The ZPLs correspond to the direct electron transition within the ZnO bandgap. Since the measured width was the limitation of the spectrometer, it has been suggested that more accurate values of the width can be obtained by PL excitation spectroscopy [65]. The fast dynamics of the intensity fluctuations are reduced at cryogenic temperatures around 5 K. Therefore, the phonon sidebands are reduced and the emission between 8 % and 14 % of the emission comes from ZPL, which is attributed to Debye-Waller factor of a defect. The measured $g^2(\tau)$ from a single defect exhibits antibunching with a similar $g^2(\tau)$ with the room temperature measurement shown in Figure 2.6(a) and 2.6(b), but no bunching behavior was observed at 5 K. To investigate jump behavior of the ZPL accurately [66], power-dependent spectral jump of ZPL was measured. The temporal behavior of the ZPL is captured by continuously measuring spectra at an exposure time of 1 second. It has been shown that the central position of the ZPL jumped within a spectral window of a few nm to locations evenly spaced by 0.5 nm. Figure 2.7(b-d) show that the frequency of jumps and the jump distance increases with increasing power. The smallest energy jump distance is 1 meV, which is sufficiently below the phonon-assist energies in ZnO that ranges from 10 meV to 100 meV [7]. They suggested that the spectral jumps were attributed to ionization of shallow charge traps by excitation source, not to jumps between different structural defects in ZnO lattice because the observed results have similar behavior of spectral diffusion and jumps in nitrogen vacancy centers in diamond nanocrystals [65, 67]. As phonon-assisted decay channel is reduced at low temperature, the lifetime is increased by three times compared to the calculated lifetime at room temperature, and thus the saturation intensity is reduced.

2.3 ZnO optical resonators

In the previous section, several promising SPSs in ZnO were highlighted. The next step is coupling those emitters to optical cavities. An optical cavity is considered to be one of the most important factors for light emission in optical materials and devices

because it confines and stores the light at resonance frequencies determined by its configuration. The flexible control provided by the ZnO growth techniques facilitates bottom up engineering of ZnO optical cavities with various geometrical shapes and sizes such as tetrapods, tapered nanowires, and mushrooms [68-70]. In this section, optical resonators of ZnO are reviewed as they offer high quality (Q) factors and are easily fabricated. In addition, FPMs or polariton cavities have also been widely studied in the field of cavity quantum dynamics with the demonstration of the strong coupling regime [71]. Since this is a rapidly growing field and some potential applications have been already achieved, this section reviews the state of the art research activities about the WGMs and other cavity effects of ZnO.

2.3.1 Whispering gallery modes (WGMs) from ZnO nanostructures

WGMs have been demonstrated in recent years, allowing light to be confined within small dimensions with high finesse. In the case of resonators, the light is trapped inside the cavity by multiple total internal reflections at the interface near the structure and the surrounding medium, resulting in light circulation around in the cavity at the inner walls of ZnO structures [72]. Due to a lower loss and better confinement, ZnO WGMs are expected to exhibit a high Q factor and relatively simple fabrication [73, 74]. So far, WGMs have been observed in various ZnO nanostructures such as triangular [75], hexagonal [76], or dodecagonal [77] cross section. The different types of WGMs differ by the length of their closed optical pathway, the angle of incidence impinging light wave fronts on the cross section boundary and the number of reflections at boundary that give rise to phase shifts of the light waves for each total internal reflection. As spherical shaped ZnO optical cavity has been reported [78], however, most of ZnO nanostructures in which WGMs have been observed so far have a hexagonal cross sections arising from the hexagonal wurtzite crystal structure. WGMs emission have been investigated in hexagonal ZnO micro- and nano-disks [73, 79, 80], nanonails [81-83], and wires [84, 85]. Figure 2.8(a-e) shows typical secondary electron microscope (SEM) images of ZnO optical cavities.

Some key research findings about the WGMs from ZnO nanostructures are now discussed. To date, there have been several investigations about the enhancement of

visible emission from ZnO by WGMs [81, 86]. The graph in Figure 2.8(f) shows luminescence spectra of the visible emission band enhanced due to a preferred constructive interference of light. It also presents resonance spectra of polarization-resolved μ-PL spectra of ZnO microcavities. While the topmost, green curve, is the unpolarized PL spectrum, the lower two curves are transverse magnetic (TM) and transverse electric (TE) polarized PL spectra. It can be clearly seen that the emission is modulated with resonance lines of different width and spacing. Due to the refractive index difference between TE (electric field perpendicular to the wire axis) and TM (electric field parallel to the wire the axis) mode, the positions of resonance peaks are different.

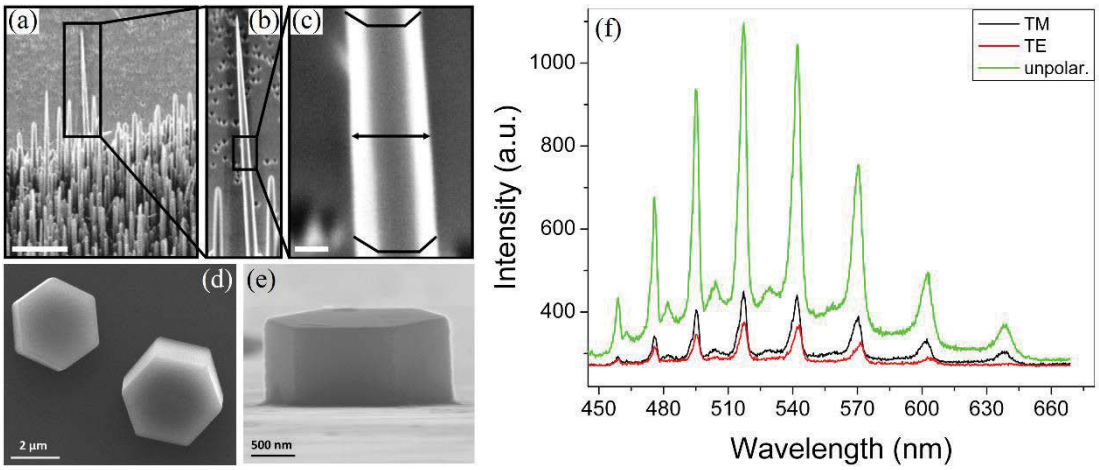

Figure 2.8. (a) SEM image of an array of ZnO nanoneedles containing the reported one marked by a black rectangle. The scale bar has a length of 10 μm (b) Magnified SEM image of the investigated nanoneedle. The needle's diameter is continuously tapered approaching zero at the top. (c) High resolution SEM image indicating the hexagonal cross section of the needle. The scale bar has a length of 300 nm [76]. (d, e) SEM image of ZnO microdisks [80]. (f) Polarization-resolved μ-PL spectra of an individual ZnO microwire. The topmost green curve is the unpolarized PL spectrum. The spectra detected for TM and TE polarizations are shown in the lower two curves [85].

Figure 2.9(a) shows a spatially-resolved CL spectrum from an individual ZnO nanonail head with a side length of 794 nm. The position marked by a cross in the inset is

examined by the CL. Most of the CL peaks were identified as TM- and TE-WGMs through the systematic investigation based on the mode equations and Sellmeier's dispersion relations (Figure 2.9(b) and 2.9(c)) [83]. Some of local polarization-dependent experiments show that WGMs are preferentially TM polarized, but other works investigated that the WGMs observed from ZnO microcavities were mostly TE polarized [87].

Figure 2.9(d) shows the dependence of the WGMs on the diameter of the ZnO wires. It can be seen that the positions of the TM polarized resonant peaks grew well with the theoretical values for different wire diameters. The symbols are the experimentally observed peak positions with the interference orders while the curves are the calculation of the constructive interference conditions for WGMs. A larger diameter leads to smaller interference mode spacing and higher interference orders observed in the same spectral range, and it is also shown that with decreasing diameter, these maxima peaks continuously shift to higher energies [85]. For WGMs, the Q factors of visible emission from ZnO structures are range of 20 to 90.

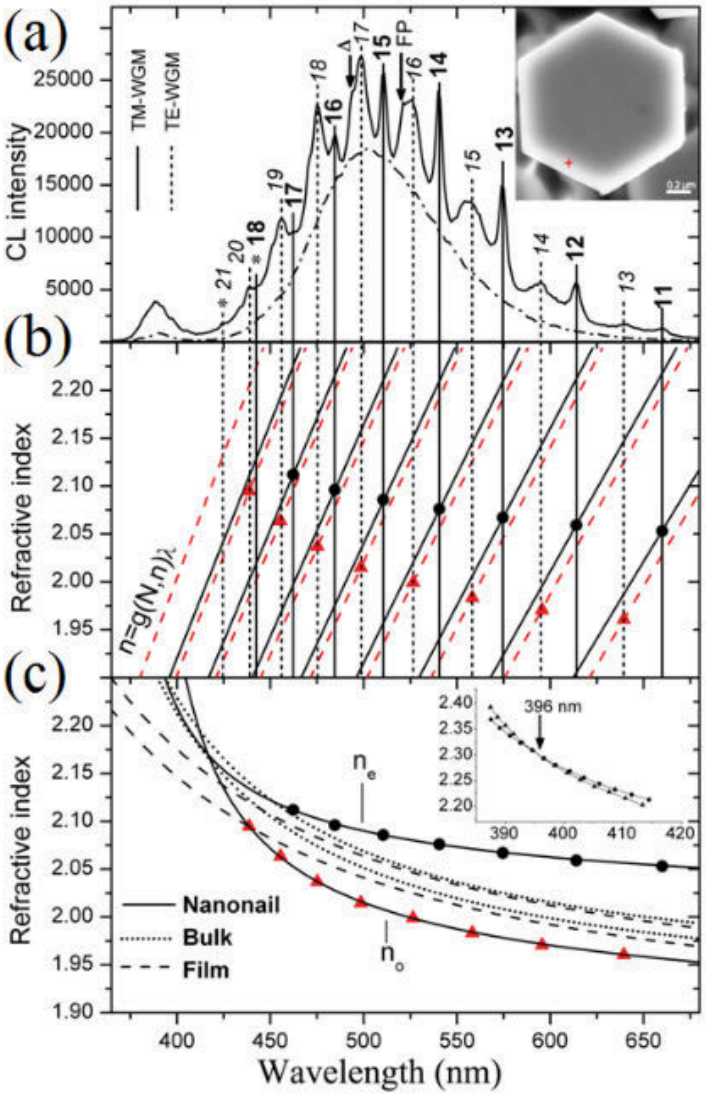
(a)
CL intensity
TM-WGM
TE-WGM
(b)
Refractive index
n=g(N,n)λ
(c)
Refractive index
Nanonail
Bulk
Film
n_e
n_o
396 nm
Wavelength (nm)

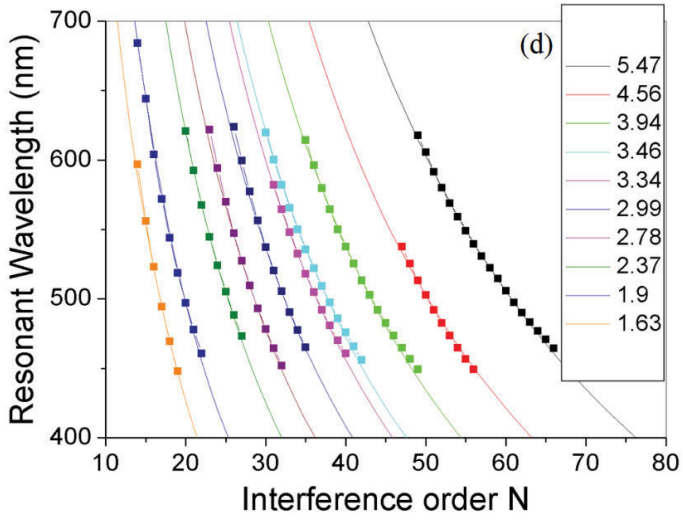
(d)
Resonant Wavelength (nm)
Interference order N
5.47
4.56
3.94
3.46
3.34
2.99
2.78
2.37
1.9
1.63

Figure 2.9. (a) CL spectrum from an individual ZnO nanonail with a series of peaks corresponding to dielectric-cavity resonance modes convoluted. The integers are the mode numbers for respective resonant mode peaks. The inset is a top-view SEM image of a ZnO nanonail with a side length of 794 nm, and the electron beam position is marked with a cross. (b) The series of solid and dash lines are the inverse functions of TM-WGMs and TE-WGMs equations with the corresponding mode numbers in (a), respectively. (c) The dispersion curves for TE (n_0) and TM (n_e) were derived by fitting the peak position and refractive indices to Sellmeier's equations. The inset shows the inversion point of bulk crystals [83]. (d) The dependences of the resonant wavelength of TM polarization on the interference order N for different wire diameters [86].

It is also possible to observe the resonance effect of ZnO emission in UV region [88, 89]. Figure 2.10(a) and 2.10(b) show confocal PL images of a ZnO microdisk measured at 383.6 nm and room temperature and at 370.1 nm at low temperature, respectively. Another monochromatic CL image of a ZnO nanodisk at 378 nm is shown in Figure 2.10(c). As can be seen from the images, the intensity distributions of the disks are not uniform, and are only concentrated at the hexagonal boundary of the disks. The enhanced UV emission is attributed to the total internal reflection of light within the disks when light impinges on the hexagon interfaces. The intensity profile across the corresponding nanodisk is shown in Figure 2.10(d), and the stronger intensity near the boundary can be clearly seen, which ascribed to WGMs emission. The darkened area is one-quarter of the total area under the intensity profile and the percentage of WGMs enhancement in the total luminescence at 378 nm is approximately 25 %, which is in good agreement with the result obtained from the spatial distribution of luminescence intensity [90]. Spectral analysis in Figure 2.10(e) shows the UV CL emission from a vertically grown isolated hexagonal microdisk and Figure 2.10(f) shows theoretical analysis from the UV emission in the Figure 2.10(e). It can be seen that the emission peak positions are in good agreement with the theoretical modes, which confirms the presence of WGMs. From the best fit of the experiment data, a calculated value for the diameter is close to the size of the ZnO microdisk. Accurate values for the WGMs peak positions can be identified at the intersections of a series of solid lines for different mode number N (from 202 to 212).

Interestingly, Moriangthem et al. fabricated a ZnO microsphere that exhibited WGMs evolution in both entire visible range as well as near UV region with narrow resonance peaks [78]. Using size dependence observation and theoretical comparison with experiments, comprehensive investigations were performed to confirm that observed emission was indeed from WGMs. The *Q* factors of WGMs in UV region were higher than that of visible emissions, ranging from around 100 to more than 4000.

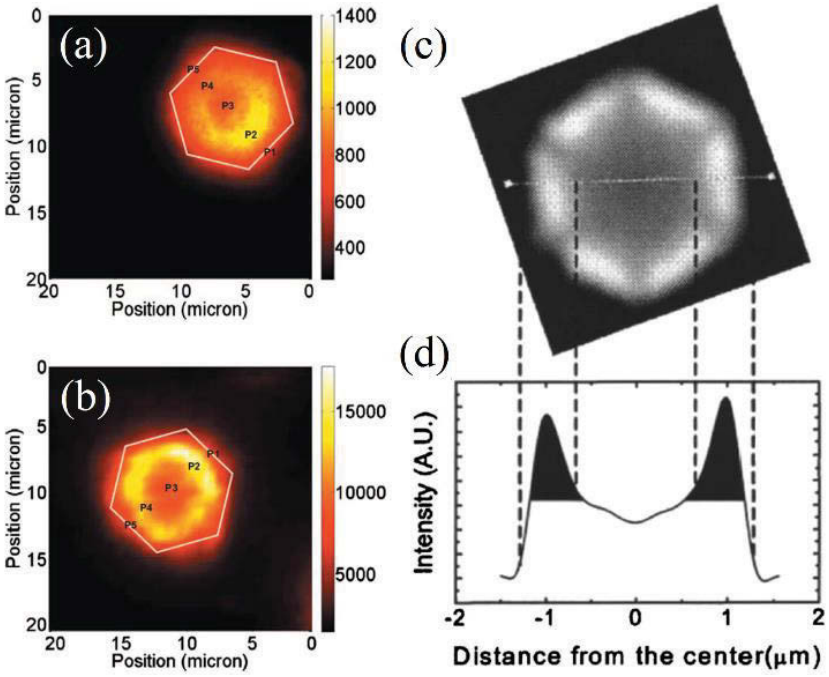

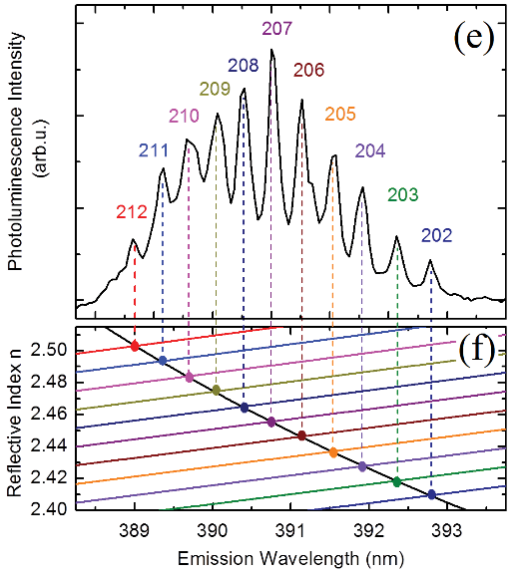

Figure 2.10. PL images of a ZnO microdisk (a) at room temperature and (b) at 10 K. The images are constructed from intensities at 383.6 nm and 370.1 nm, respectively [88]. (c) Monochromatic CL image of a ZnO nanodisk at 378 nm. The side length of the ZnO hexagonal nanodisk is approximately 1.5 μm. (d) Intensity profile across the nanodisk. The darkened area indicates the luminescence contribution from the WGMs emission [90]. (e) PL spectrum of a ZnO microdisk. (f) Inverse functions of WGMs with the corresponding mode numbers given in (e). The wavelengths are determined by the intersection points with the Sellmeier's first order dispersion function [73].

2.3.2 Additional ZnO optical cavities

In addition to WGMs, other types of ZnO resonators were studied. In terms of geometrical optics, FPMs and quasi-WGMs are formed when the light ray strikes top and bottom planes of the cavity and the boundary at 30° relative to the normal to the surface boundary, respectively. The FPMs have been observed in elongated ZnO nanostructures such as wires or tubes. Here, FPMs occur perpendicular to the cross section plane by reflections between the wire end facets in nanowires with a constant diameter [91, 92]. It have also been demonstrated in tapered nanowires [93, 94]. The standing waves are formed whenever the cavity contains an integral number of half-wavelength. Thus, the optical path length for constructive interference in this case is equal to twice the cavity length. Similar to WGMs, FPMs also can exhibit high Q factors and thus show lasing action in ZnO nanostructures [95].

FPMs in ZnO microstructures with hexagonal cross sections have been shown to be novel optical resonators [96]. Optical study of the ZnO microrods is carried out under a confocal μ-PL spectrometer and a broad PL signal in the range of 360 nm – 700 nm is observed in Figure 2.11(a). The modulations can correspond to the several resonance optical modes because of its geometrical shape. From the point of view of geometrical optics, four kinds of resonant cavity modes can be formed in the microcavity; WGMs, horizontal-FPMs, quasi-WGMs, and vertical-FPMs as shown in the right inset of Figure 2.11(a). For FPMs, two different light directions can be studied. While light travels back and forth between the two narrow opposite sides of the microrod (horizontal-FPMs), light can also travel between the top and bottom planes of the

microrods (vertical-FPMs). For WGMs, quasi-WGMs, and horizontal-FPMs, it was deduced that the calculated path lengths were all much larger than the observed values in the experiment, which indicates that the observed emission does not arise from these that resonant modes. For the vertical-FPMs, the height of the microrod is consistent with that of obtained in the theoretical analysis based on the measured resonant modes. Furthermore, the PL spectra from ZnO with different heights were measured to investigate the relationship between the resonance modes and the vertical sizes of the microcavities. As shown in Figure 2.11(b-d), the PL signals in UV and visible spectra range are clearly modulated by varying the height of the cavity. It is interesting that a series of FPMs can be clearly identified in such a vertical microcavity with a short effective length. The number of FPMs increases clearly with increasing height of the cavity based on the FPMs condition. In addition, the width of the mode peak significantly decreases as the microrod height increases, indicating that a larger cavity height can improve the mode quality.

Another ZnO nanowire can also exhibit a series of FPMs [97] shown in Figure 2.11(e). The spectra detected at both wire ends are identical and consist of a series of peaks which can be enhanced by FPMs. The spectrum can be fitted to a sum of Lorentzians, where each Lorentzian represents an individual luminescence peak. Below 3.22 eV in the region with pronounced peaks, light is mainly emitted at the wire ends as shown in Figure 2.11(f) and 2.11(g). Since the emission spectra at both of the nanowire ends feature a series of identical peaks, it is highly likely that they reflect standing-wave modes in the ZnO nanowire. Therefore, the luminescence spectra detected at the nanowire ends is attributed to the FPMs with their wave-vector parallel to the wire's long axis. Further analysis showed that the modes are polariton eigenmodes situated on the lower polariton branch.

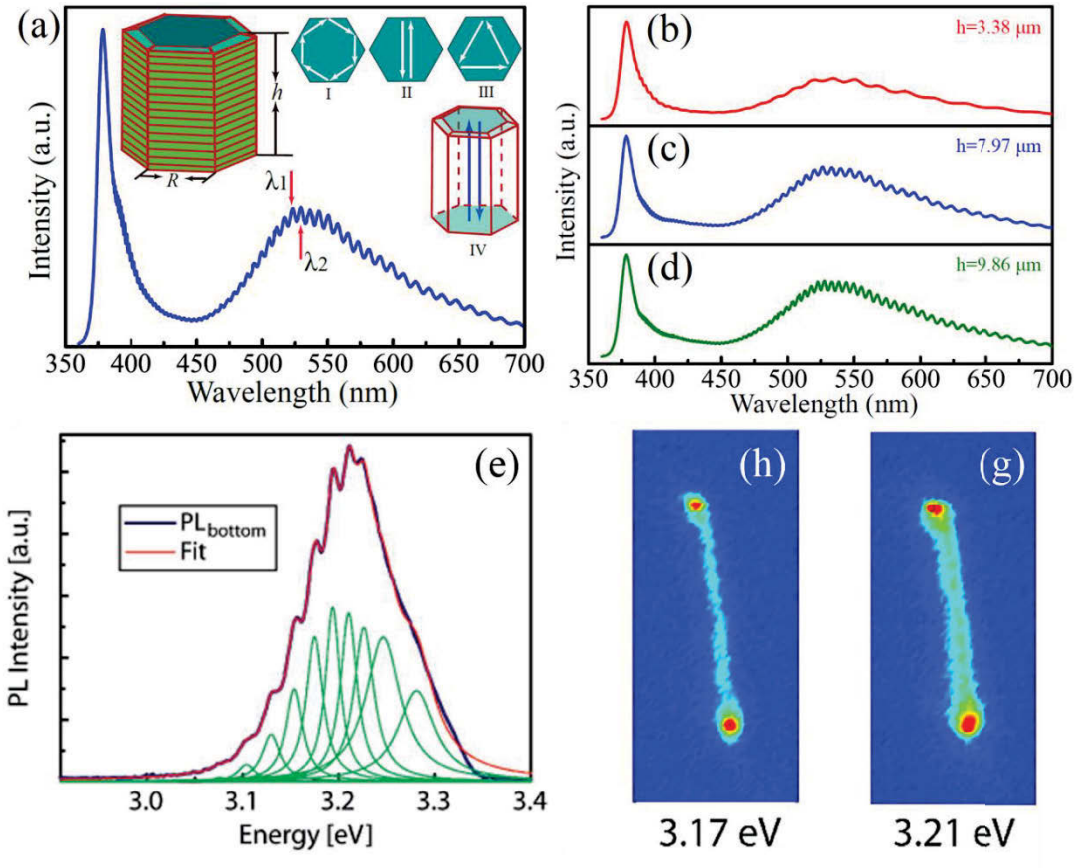

Figure 2.11. (a) PL spectrum from the individual ZnO microrod. Insets show the diagrams of the 4 light paths. (b-d) PL spectra collected at the center of the top facet of 3 ZnO microrods with different heights [96]. (e) Analysis of the emission spectrum from a ZnO single nanowire at the bottom end as a sum of Fabry-Pérot peaks each with a Lorentzian line shape. (f, g) Map of the emission intensity along the nanowire at two different photon energies [97].

ZnO possesses outstanding optoelectronic properties such as exciton resonances due to spin-orbit coupling in the crystal field with a large oscillator strength and a large exciton binding energy ~ 60 meV [98]. Thus, ZnO can be one of the most potential candidates for realization of exciton-polariton emission [99]. Inside a suitable optical cavity or photonic crystal structure, excitons can strongly couple with the cavity mode and form cavity polaritons. As a result, it is likely that the light-matter interaction between optical modes is strong and therefore excitonic-polariton effect can be beneficial for proper understanding of the UV luminescence spectra of ZnO

nanostructures [100]. These polariton cavity modes exhibit a hyperbolic dispersion relation in the plane of optical resonator [101]. The dispersion curve of exciton-polaritons in optical cavities can be obtained by measuring the reflectivity or PL. For strong exciton-photon coupling in ZnO, thin films and nanostructures has been investigated from angle-dependent absorption, reflection, and luminescence spectroscopy at room temperature and cryogenic temperature [102-104]. In addition, some findings of polariton lasing have been studied in various microcavities including the WGMs microcavity [104-107]. For example, the strong coupling regime was observed from a ZnO tetrapod in WGMs cavity, as shown in Figure 2.12(a).

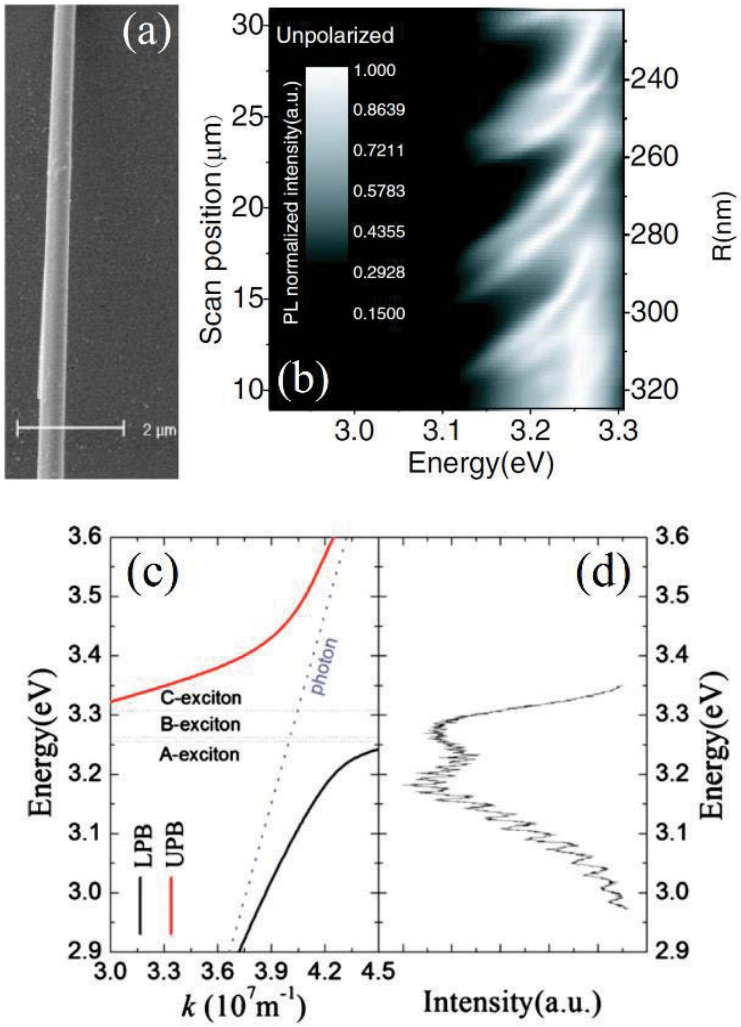

Figure 2.12. (a) Magnified SEM image of a ZnO tetrapod. (b) Spatially-resolved PL mapping along the tapered arm with the excitation laser polarization $E \parallel c$-axis and

detection unpolarized [105]. (c) Exciton-polaritons dispersion curve from a ZnO microrod. The blue dashed line is the pure cavity mode dispersion. The horizontal dashed lines denote the exciton A, B, and C. (d) TE polarized μ-PL spectrum from the microrod [107].

Interestingly, a tapered arm of the ZnO tetrapod has a varying radius, which leads to different energy and the number of orders of WGMs cavity by choosing different position along the tapered arm. Therefore, μ-PL scan was used to investigate the polariton emission along the tetrapod (Figure 2.12(b)). PL mapping clearly shows the modulation of UV luminescence, indicating excitonic-polaritons resulting from a strong coupling between WGMs and excitons in the cavity, relatively low energy side for WGMs and higher energy side for exciton-polariton branch. Recently, strong coupling regime from WGMs in a ZnO microrod cavity has been reported [105, 107]. To understand the spectral nature in UV emission region, polariton effects that are induced by the interaction between optical modes and excitons should be considered. It is expected that the different polarized modes relate with different polarized free excitons (A, B, and C exciton). In the coupling oscillator model, the polariton dispersion and the refractive index can be described in the simple dielectric approximation form as:

$$n^2 = \varepsilon_\infty \left(1 + \sum_{i=A,B,C} \Omega_i \frac{\omega_{i,L}^2 - \omega_{i,\gamma}^2}{\omega_{i,\gamma}^2 - \omega^2 - i\omega\Gamma_i} \right) = \frac{c^2 k^2}{\omega^2} \tag{2.7}$$

where the ε_∞ is the dielectric constant, $\omega_{i,L}$ and $\omega_{i,\gamma}$ are the longitudinal and transverse resonance frequencies respectively at $k = 0$, Γ_i is the damping constants, c is speed of light, and Ω_i is a parameter determined by the longitudinal and transverse resonance frequencies [102]. According to the exciton-polariton dispersion, the exciton-polariton dispersion curve is separated into upper polariton branch (UPB) and lower polariton branch (LPB) as shown in Figure 2.12(c) and 2.12(d). The energy positions of the two enhanced peaks correspond to the bottom of the UPB and the transition region of the LPB, respectively. Besides WGMs polaritons, PL investigations of quasi-WGMs polaritons in a ZnO microrod have also been studied [108]. The quasi-WGMs were

shown at the UV region where the cavity modes strongly couple with excitons and form polaritons. The calculated dispersion relations showed the A-exciton resonance for the cavity polaritons showing good agreement with the experimental data points. Scanning μ-PL measurement was performed along the *c*-axis of the microrod to confirm the fine structures and explore their physical properties.

2.4 Nanophotonic devices from ZnO

Now several applications of the photonic devices are discussed – focusing on amplified spontaneous emission (ASE), lasing and electrically driven devices.

2.4.1 Lasing action in ZnO

Numerous reports on stimulated emission in ZnO have been published. However, important to note that majority of these papers in the literature only report on ASE, rather than lasing [109, 110]. A dominant line in luminescence spectrum does not automatically mean lasing, rather it is critical to confirm a change from linear to ASE as well as from ASE to lasing on a log-log plot of the light in and light out plots [95]. WGMs ASE in the excitonic UV band was shown by Czekalla et al. [84, 111]. Hierarchical structures such as nanotubes and nanowires [112] or ZnO nanoplate-nanowire architectures [113] have been studied as new directions for integrated device applications. In recent years, ASE has been investigated in ZnO powders and patterned films with incoherent and coherent feedback in the gain media [114, 115]. UV lasing in ZnO has been observed in powder, thin-film, and nanowire samples based on the positive feedback in random and Fabry-Pérot cavities [116-118].

Due to the difficulties in achieving high *Q* from ZnO samples, the distinct WGMs lasing was observed from individual ZnO microwires at low temperature. Following this work, more detailed investigations have been carried out, and the performance of WGMs lasing has been improved remarkably, which can be observed directly at room temperature from different ZnO micro- nano-structures with hexagonal cross section. By changing the excitation density, the transformation from spontaneous emission to

stimulated emission can be directly observed. Very recently, a membrane-type of ZnO microcavity is fabricated and characterized [119]. Figure 2.13(a) depicts a schematic diagram of the ZnO membrane-type microcavity and corresponding pumping schemes. Figure 2.13(b) is a SEM image of suspended ZnO membrane. Through changing the pumping regimes, manipulation of P-band exciton lasing and WGMs lasing could be easily achieved. The calculated vertical optical field distribution, shown in Figure 2.13(c), is obtained using the transfer matrix method. To observe the triggering condition of P-band exciton lasing and WGMs lasing, four types of pumping scheme is studied as shown in Figure 2.13(d). Thus, the WGMs could be manipulated by modifying the intensity and position of the pumping laser. The insets of Figure 2.13(e) and 2.13(f) show the optical microscopy images of a large pumping spot at the center (regime III) and at the edge (regime IV) of the ZnO microcavity, respectively. For pumping regime III, the pumping spot showed a larger WGMs overlapping to a higher order WGMs compared with pumping regime I because of the larger pumping area, which was useful for triggering the WGMs lasing. The spectra in Figure 2.13(g) show a non-linearly enhanced intensity and a linewidth narrowing behavior when the laser power exceeds the threshold. The single mode lasing behavior of regime III was attributed to the edge accumulated WGMs characteristics. As the pumping spot was removed towards the edge of the microcavity (regime IV), additional WGMs were excited. In Figure 2.13(h), two WGMs were excited and lased above the threshold as a result of the edge-pumping scheme. An intensity saturation of this dominant peak was related to the gain competition with another lasing peak.

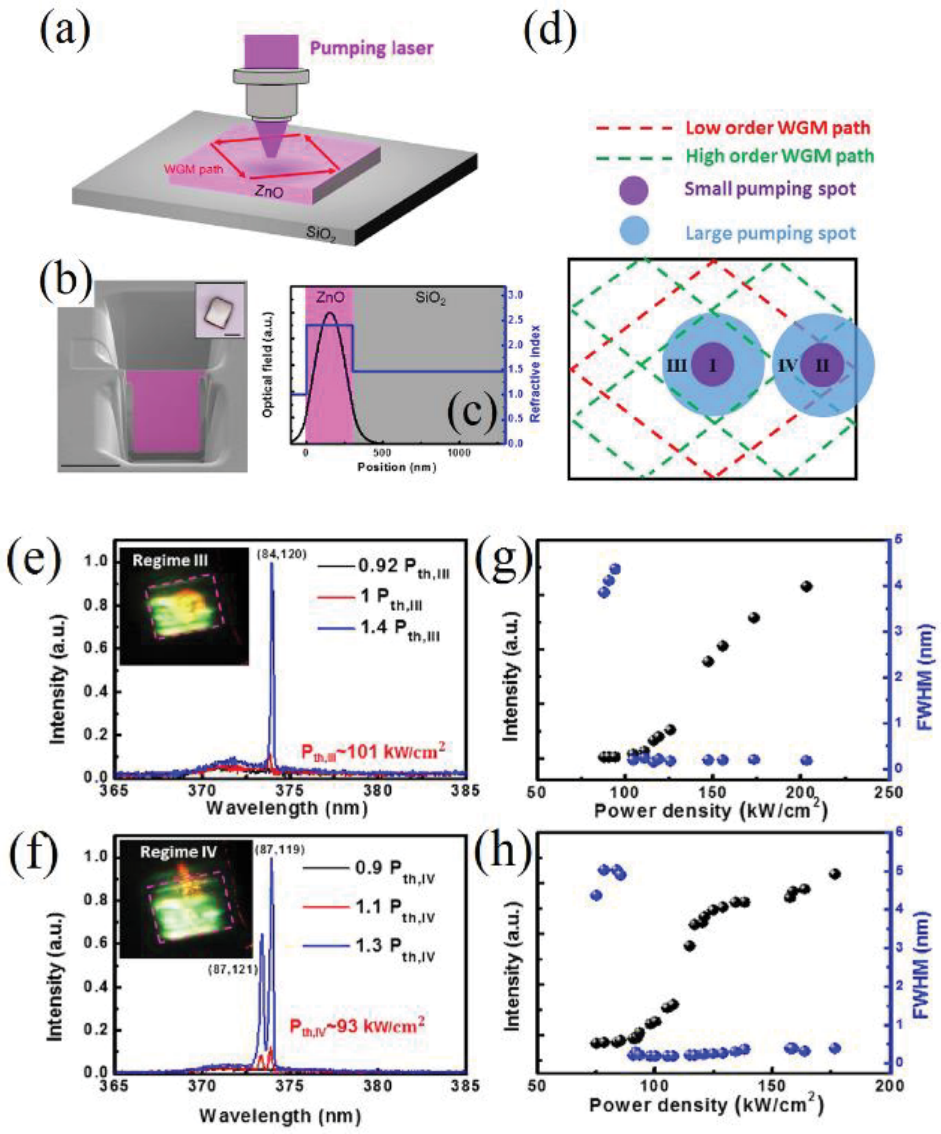

Figure 2.13. (a) Schematic plot of ZnO membrane microcavity and the configuration of optical measurement. (b) SEM image of suspended ZnO membrane with false color for clarity. Inset shows the optical microscope image of ZnO membrane on the silicon dioxide (SiO_2) substrate. The scale bar in both the main figure and the inset figure is 10 μm. (c) Refractive index and optical field distribution along the vertical direction of ZnO microcavity. (d) Schematic plot of 4 pumping schemes and the optical paths for WGMs. (e-h) Measured spectra and peak intensity and linewidth versus pumping intensity at regime III and IV pumping condition. Insets in (e) and (f) display the optical microscope images of pumping spot on ZnO microcavity of regime III and regime IV, respectively [119].

Recently, stimulated emission from FPMs has been investigated from ZnO nanostructure cavities that are composed of waveguides and end-facet mirrors [120-122]. Figure 2.14(a-c) shows the sample morphology and transmission electron microscopy (TEM) images of ZnO nanoribbons. Figure 2.14(d) shows a far-field emission image of another nanoribbon and Figure 2.14(e) shows the PL intensity as a function of excitation power. At a low excitation power density, broad UV emission was observed at around 387 nm. With the assumption that this nanoribbon was supported as FPMs optical cavity, the calculated value was almost in well-agreement with observed mode spacing of 0.85 nm obtained from the difference between peak to peak. Thus, it confirmed the formation of longitudinal FPMs cavity by the reflection at the end two facets of the nanoribbon. As increasing the excitation power density, the intensity of these peaks became strong and additional lasing mode appeared between the energy peaks (Figure 2.14(f)). Figure 2.14(h-k) shows another optically excited ZnO nanowire below and above lasing threshold. It is clearly seen that the nanowire is directed by spontaneous emission below threshold across the whole nanowire surface with the uniform and broad light, but exhibits only two light sources of stimulated emission at the nanowire end of facets above threshold, indicating the light interference is due to FPMs. The emission even displays diffraction patterns indicating high spatial coherence. From the PL spectra in Figure 2.14(l-o), the broad emission altered to a sharp peak with mode spacing on increasing the excitation intensity.

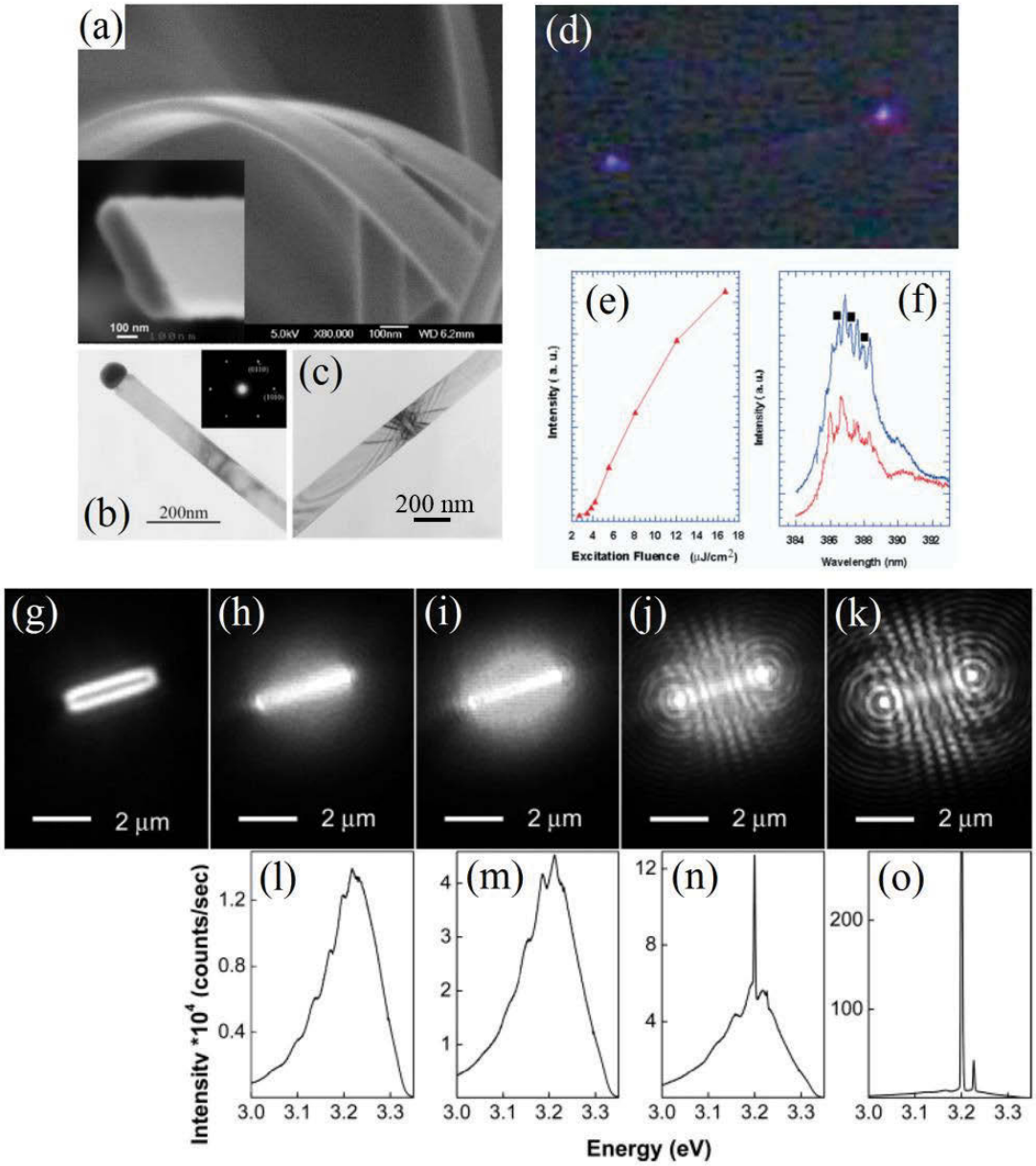

Figure 2.14. (a-c) SEM and TEM images of ZnO nanoribbons. (d) PL far-field image of a ZnO nanoribbon. (e) Integrated emission intensity against excitation power of the corresponding nanoribbon. (f) Emission spectra from the nanoribbon at different excitation powers above lasing threshold [120]. (g) Dark-field optical image of a ZnO nanowire laser. (h-k) Panchromatic PL images of the nanowire with increasing excitation intensity. (l-o) PL spectra taken at the excitation intensities corresponding to images (h-k) [121].

Additionally, other nanostructures such as hexagonal nanorods [123] and tetrapods [124, 125] were demonstrated to show laser activity. However, most of the lasing is observed in the UV region. Although visible lasing from ZnO nanostructures has not been widely reported, one study shows that white light and visible luminescence are observed from ZnO nanocolumns grown on Au-coated tin-oxide glass [126]. The observed lasing emissions related to FPMs cavities were confirmed by the directionality of the emission, lasing threshold and mode spacings. Figure 2.15(a) shows the SEM image of ZnO nanocolumns and Figure 2.15(b) is the corresponding PL spectrum obtained at different pumping intensities. The curve, which is above the threshold pumping intensity, exhibits a number of peaks that occurs only at the modal frequencies of the cavity. The cavity mode features are due to laser action within the solid ZnO nanocolumns based on the mode spacing calculation.

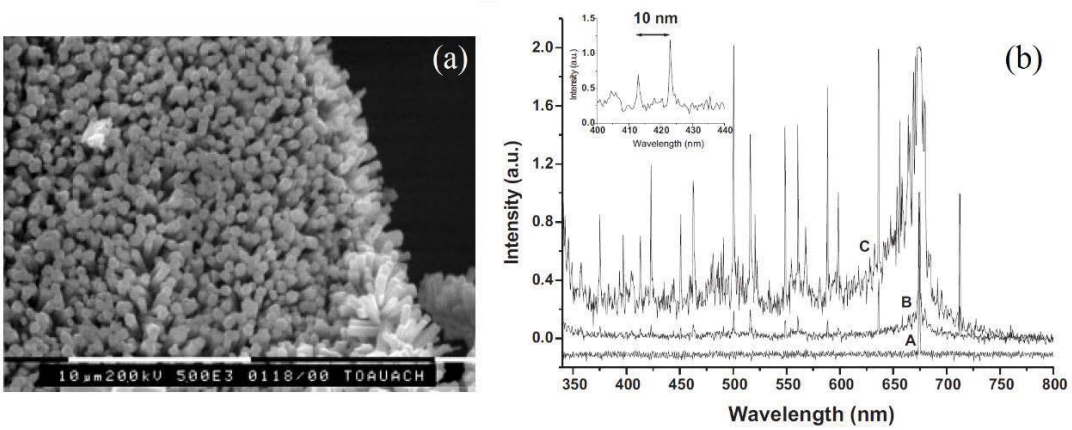

Figure 2.15. (a) Crystallographic representation of ZnO nanocolumns. (b) PL spectrum for the nanocolumns for a pumping intensity of **A**: below threshold, **B**: 5.5× above threshold, and **C**: 11× above threshold. Inset shows expanded view of spectrum **C** showing a mode spacing of 10 nm [126].

Multiple scattering of light can be achieved in a disordered medium within gain, and thus light amplification can be enhanced by modifying the path length and dwell time of light in an active medium [127]. It is called random lasing that the light is amplified along the closed and optical loop feedback paths by the repeated scattering at the boundaries. These pathways can also advance in disordered dielectric media when scattered light interferences produce positive coherent feedback for lasing oscillation

[128]. Optical gain should be larger than losses to achieve random lasing. It has been studied that the scattering mean-free-path should be reduced below the wavelength of the light [129]. As a result, the probability that light returns back to the positions where it has been scattered before is increased [116]. In addition, emission properties with changing laser spot sizes should show a different number of lasing peaks in the emission spectra because the change of the spot size affects the number of closed loop paths. Since closed loop path shows different output directions, modification of emission angles also influences the emission spectra. Random lasing has been demonstrated in several ZnO nanostructures, such as powder [116, 130], nanowires [25], nanoparticles [131], or polycrystalline ZnO thin films [129].

Figure 2.16(a-c) present an example of random lasing showing the evolution of the emission spectra as the pumping intensity was increased. When the pumping intensity was increased, additional peaks emerged and the emission peak became narrower due to the preferential amplified emission at frequencies close to the maximum of the gain spectrum. After the pumping intensity was further increased larger than the threshold, distinct narrow peaks appeared on top of the broad spontaneous emission peak. The linewidth of these peaks was less than 0.3 nm, which is much smaller than the width of the spontaneous emission peak. Laser emission from the ZnO nanostructures could be observed in various directions. As shown in Figure 2.16(d) and 2.16(e), the laser emission spectra changes with the detection angle. Since different laser cavities formed by multiple scattering show different output directions, lasing modes observed at various angles can be different. Additionally, Cao et al. studied micro-random lasers with disordered and closely packed ZnO nanoclusters [132]. Figure 2.16(f) shows a nanocluster of size ~ 2 μm. The ZnO nanoparticles have an average size of 50 nm. When the pumping intensity exceeded a threshold, a sharp peak appeared from the emission spectrum in Figure 2.16(g). Simultaneously, some bright spots appeared with light distribution in the nanocluster in Figure 2.16(h) and 2.16(i) which show the images of the light distribution on two planes with different depth inside the nanocluster. These images demonstrate three-dimensional localization of laser emission in the random medium. This three-dimensional light confinement could be realized through the process of multiple light scattering and wave interference. When

the pumping intensity was increased further, well above the threshold, a second sharp peak appeared in the emission spectrum (not shown), and the total emission intensity increased with the pumping intensity.

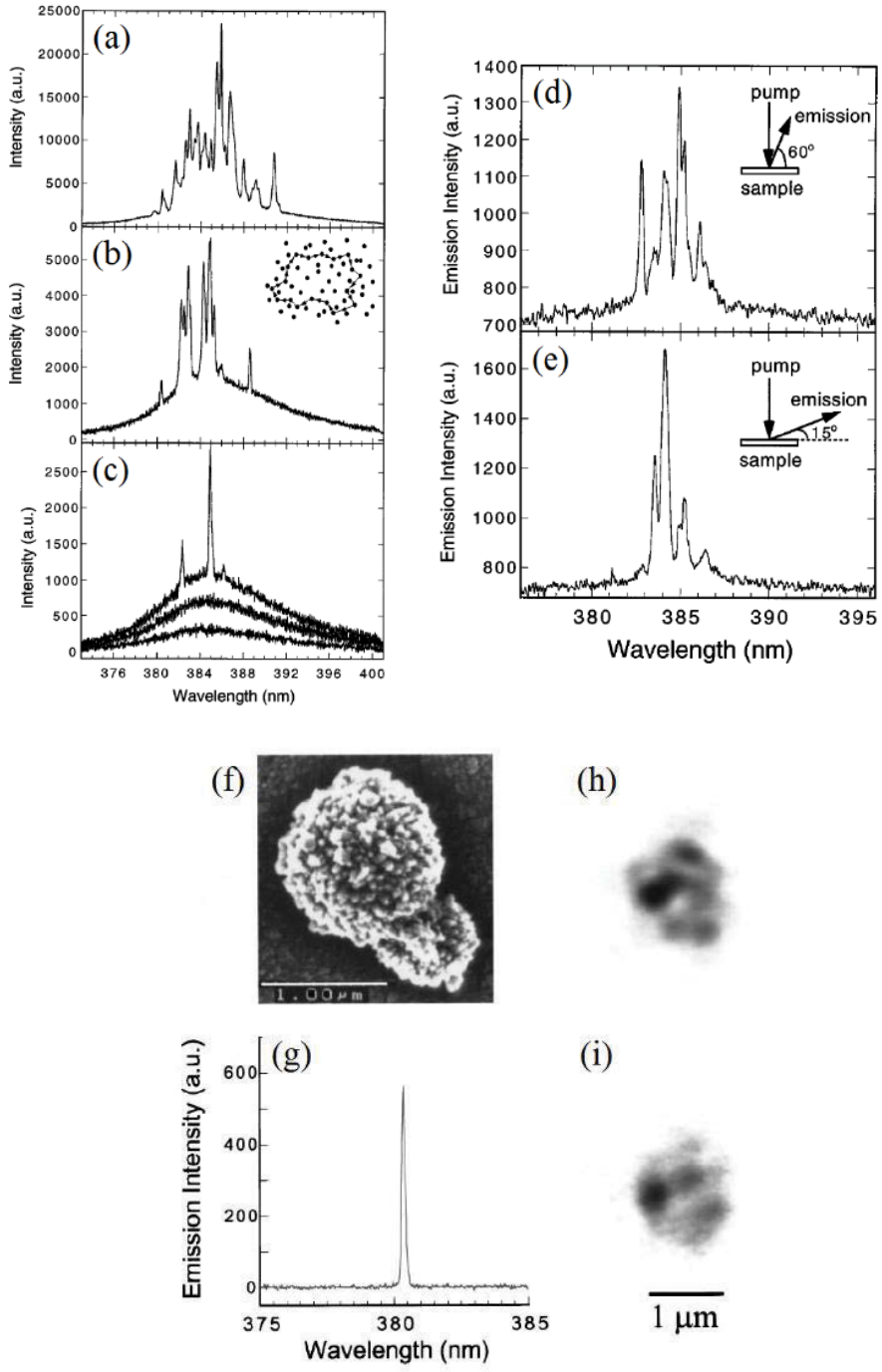

Figure 2.16. (a-c) Spectra of emission from ZnO powder when the excitation intensity is (from bottom to top) increased. Inset in (b) is a schematic diagram indicating the

formation of a closed loop path for light through recurrent scattering in the powder. (d, e) Emission spectra of laser emission into two directions: (d) 60° from the sample surface, (e) 15° from the sample surface [116]. (f) SEM image of a second ZnO cluster. (g) Spectrum of emission from this cluster above the lasing threshold. The incident pump pulse energy is 0.27 nJ. (h, i) Spatial distribution of emission intensity in the cluster at the same pumping power [132].

2.4.2 Hybrid / heterostructures

Regarding the electrically driven light devices and lasers, the fabrication of high-quality p-type ZnO remains great challenge. Due to the p-type doing problem, many researchers reported on the heterostructures with n-type ZnO grown on p-type materials of GaN, Si, and conducting oxides [31, 133, 134]. Among the possible heterostructures, the structure ZnO/GaN has attracted extensive interest [135-137] because device structures such as n-ZnO/p-GaN can be readily realized because the lattice mismatch between ZnO and GaN is modest (~ 1.9 %) [43]. Another alternative p-type material is acceptor doped Si [138]. Some of heterostructure devices are shown in Figure 2.17.

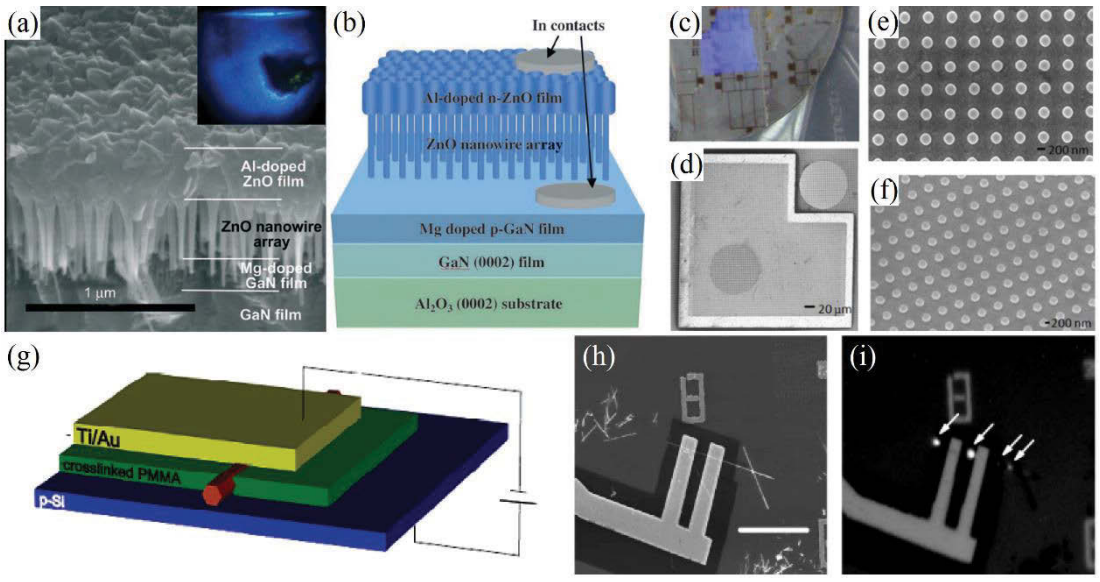

Figure 2.17. (a, b) SEM image and schematic diagram of Mg-doped GaN film/ZnO nanowire array/Al-doped ZnO film structures for nanometer-sized ZnO/GaN heterojunction applications. Inset of (a) is a photograph of blue-light emission from

the heterojunction diodes observed through a microscope at the forward current [135]. (c) Optical image of ZnO nanorod arrays imprinted on GaN. (d) Top view micrograph image of the ZnO nanorod arrays, along with their enlarged (e) top view and (f) tilt view SEM images [137]. (g-i) Schematic description, SEM and optical images of a single ZnO nanowire/Si heterostructure [139].

One of the most promising applications of the ZnO-based heterostructure is for UV light emitting devices [140]. Figure 2.18(a) shows electroluminescence (EL) spectra of the ZnO-nanowires/p-GaN heterostructures with forward bias, exhibiting emission peak centered in the UV at 397 nm. The EL emission significantly increased from the emission threshold (~ 4.4 V) and is slightly red-shifted compared to the PL emission of ZnO and GaN. The top inset in Figure 2.18(a) shows there is no short circuit in the constructed device, consequently the UV emission is most likely attributed to radiative recombinations in ZnO from the heterojunction. Above 6 V, the violet-blue emission is easily observed with the naked eye as shown in the bottom inset of Figure 2.18(a), imaged with a charged coupled device (CCD) camera. The round-shape spot is originated from the whole disk-shape ZnO nanowires-layer.

Another study showed different EL behavior from other n-ZnO/p-GaN heterojunctions where the EL generated only from either the n-ZnO or p-GaN side [136]. EL spectra from the n-ZnO/p-GaN:Mg exhibited the superposition of light emissions from both the n-ZnO and p-GaN layers. The competition between the EL from the n-ZnO and from the p-GaN can be explained by difference in carrier concentration and emission efficiency between n-ZnO and p-GaN, as well as the interfacial layer. To improve the emission of n-ZnO-based heterojunctions, double and triple heterostructures such as a hybrid n-MgZnO/CdZnO/p-GaN structure with a quantum-well structure [141] and MgZnO/ZnO/AlGaN/GaN were fabricated producing strong emission at 390 nm [142].

Visible EL can also be observed from ZnO/GaN heterostructures [143]. The ZnO nanorod arrays were grown on p-GaN layer using metal-organic vapor phase epitaxy without the catalyst. ZnO nanorods are fabricated vertically well on the GaN layer due to a low lattice mismatch. EL spectra from the heterojunction were measured at different reverse bias voltages as shown in Figure 2.18(b). As increasing the reverse

bias from 3 V, the yellow emission appeared and increased, and blue and UV emission were also observed. The EL emission peaks of the visible (yellow and blue) emission can be attributed to a defect-related emission and a radiative recombination related to Mg acceptor in Mg-doped GaN. On the other hand, Klason et al. used p-Si to obtain visible luminescence. They reported the EL spectra obtained from ZnO nanodots/p-Si heterojunctions [144]. White light EL consisting of a blue light at 450 nm and a broadband around 550 nm from n-ZnO/p-GaN heterojunction was also reported [145]. Alvi et al. also investigated the n-ZnO nanostructures (nanowalls, nanorods, nanoflowers, and nanotubes)/p-GaN white light emission systematically [146]. EL spectrum of ZnO heterostructures showed two main peaks positioned at violet, and violet-blue emission with some visible emission as well.

The electrically pumped WGMs ASE from hexagonal ZnO has been recently reported [147]. Figure 2.18(c-h) shows the schematic procedure for fabricating a ZnO microrod/GaN microlaser diode and its SEM images. A 20 nm Zn thin film was sputtered between the p-GaN substrate and the ZnO microrods and the thin film is put into a ZnO buffer layer after annealing process to contact between the ZnO microrod and the GaN substrate. Figure 2.18(i) shows current – voltage (I-V) rectifying curve of the device and the inset is the energy band diagram of the n-ZnO/p-GaN heterojunction. Figure 2.18(j-l) shows the room temperature EL spectra of the device at different applied current and insets of 2.18(j) are an EL image at the current of 15 mA and the EL intensity profile against the current. As the applied current is increased, 4 distinct sharp peaks occurred from the EL band, indicating the presence of ASE. When the current is increased to 15 mA, more obvious resonant peaks emerge on the spectrum and the emission intensities significantly increase. Based on the calculations using the plane wave model, it has been confirmed that the resonant sharp emission peaks originate from WGMs emission through the electrically driven device of the ZnO microrod on GaN. Even though Q factor from EL is lower than that of PL, these results strongly suggest that ZnO microdisk could be promising candidate for electrically pumped microlaser diodes.

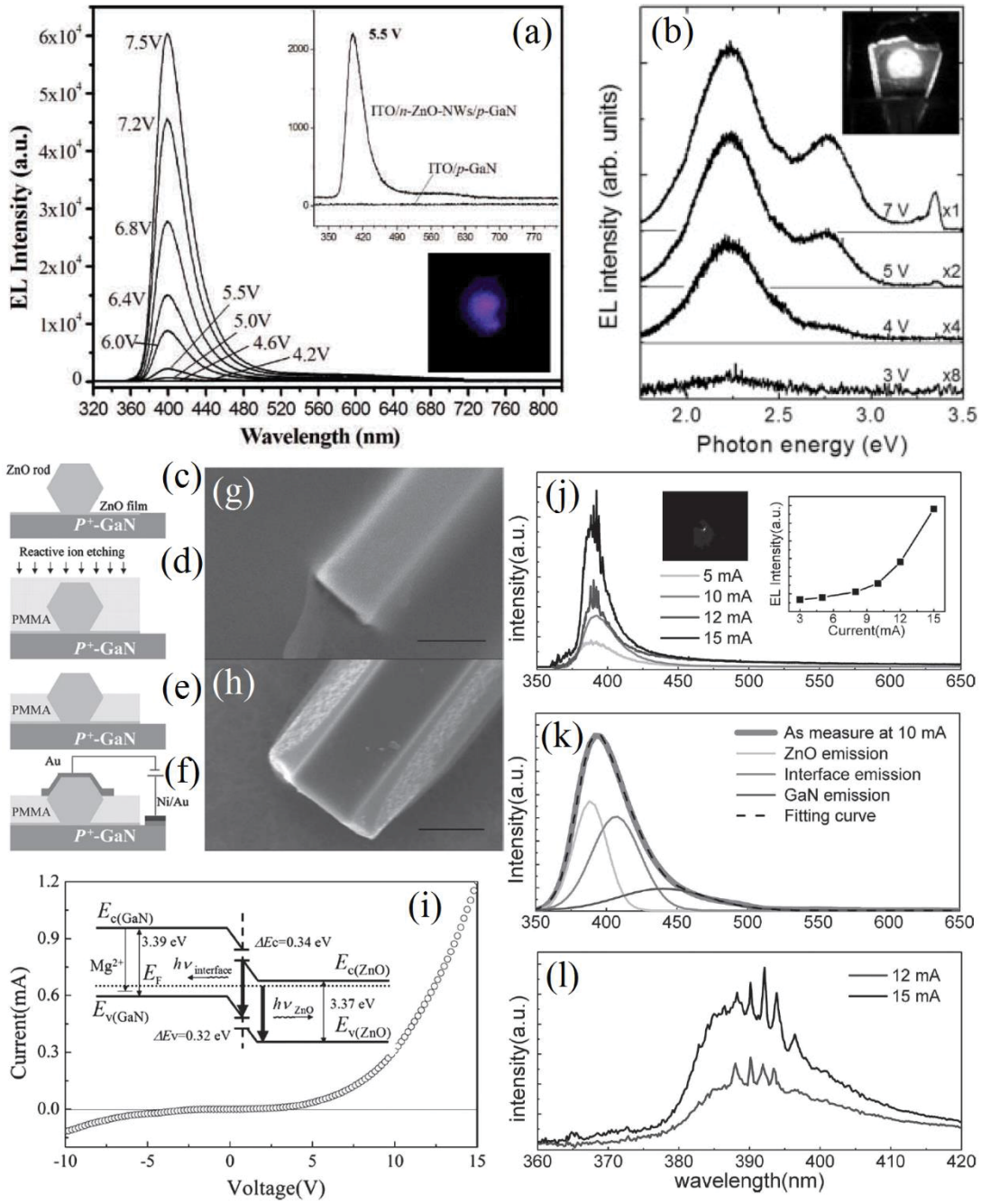

Figure 2.18. (a) Room temperature EL spectra of an indium tin oxide (ITO)/ZnO-nanowires/p-GaN/In-Ga heterojunction under different forward bias voltages. Inset (top right) shows the comparison of EL spectra from the heterojunction structure and an ITO/GaN/In-Ga structure. Inset (bottom right) is an image of the light emission spot under a DC bias of 6 V at room temperature [140]. (b) EL spectra of a n-ZnO nanorods/p-GaN device with a reverse bias voltage. Inset is a photograph of light

emission from the EL device at a bias voltage of 5 V. (c-f) The fabrication process of a ZnO microrod/GaN heterojunction [143]. (g, h) SEM image of the ZnO microrods covered by a polymethyl methacrylate (PMMA) thin film and microrod after reactive ion etching. (i) I-V curve for the ZnO microrod/GaN heterojunction; the inset shows a schematic of the band diagram. (j) EL spectra from the ZnO microrod/GaN heterojunction under different applied current. The left inset shows a photograph of the EL emission from the sample and the right inset shows the relationship between the EL intensity with the applied current. (k) Gaussian fit of the EL spectrum under the applied current of 10 mA. (l) The enlarged spectra from 360 nm to 420 nm under current equal to 12 mA and 15 mA [147].

Chapter 3

Materials and experimental methods

In this chapter, ZnO samples used during the experiments are described. Key experimental techniques to characterize the samples used in this project are also discussed. Extensive experimental investigations were undertaken to study morphological and optical properties of the sample.

3.1 ZnO samples

Three different types of ZnO were used during the experiments:

(1) ZnO nanoparticles, obtained by Nanostructured and Amorphous Material Inc., USA. ZnO nanoparticles were dispersed in methanol and ultra-sonicated to disperse the nanoparticle clumps. The suspension was then drop cast using a spin coater with a micropipette onto a clean substrate, so the nanoparticles were relatively evenly distributed across the substrate after the methanol was completely dried.

(2) ZnO thin films were produced by sputtering of 2" ZnO target (99.99 %) with a DC current controlled deposition. The film thickness is ~ 50 nm, and its SPSs and electrical properties were characterized. Growth details of the ZnO thin film are described in Chapter 6.

(3) ZnO microdisks were fabricated by carbothermal reduction of ZnO using a horizontal tube furnace, which is discussed later. The ZnO microdisks have a hexagonal structure which facilitates the observation of WGMs optical resonance.

3.1.1 Carbothermal reduction of ZnO to fabricate ZnO microdisks

ZnO growth has been studied extensively in the field of optoelectronic. One of the popular fabrication methods of ZnO micro- and nano-structures is chemical vapor deposition where a source material (typically a 1:1 weight mixture of ZnO powder and graphite) and a substrate are placed inside a growth furnace in such way that the temperature of the source material is higher than that of the substrate. Zn vapor was produced through the carbothermal reduction of ZnO powder by using graphite which was used as a reducing agent. ZnO has a melting point of 1875 °C, but the addition of graphite can lower this to 907 °C. The process of reduction is followed by:

$$ZnO_{(s)} + C_{(s)} \rightarrow Zn_{(g)} + CO_{x(g)} \tag{3.1}$$

The Zn atoms and C were then reoxidized [69] by the oxygen in air to facilitate the formation of ZnO micodisks. Oxygen can also be introduced in the furnace tube as carrier gas. The reaction can proceed according to the equation:

$$Zn_{(g)} + O_{2(g)} \text{ or } CO_{x(g)} \rightarrow ZnO_{(s)} (+ C_{(s)}). \tag{3.2}$$

Generally, this method usually takes a lot of time, so a metal catalyst is used to seed up the process. Additionally, control of the position of the substrate in the growth furnace is difficult and time consuming. Recently, however, some studies have been conducted for the fabrication of ZnO micro- and nanostructures without carrier gases and on a catalyst [148, 149].

Synthesis of the ZnO microdisks was carried out in a conventional Lindberg/Blue horizontal tube furnace. The details of fabrication methods are discussed in chapter 7.

3.2 Annealing process

Annealing processes have been performed in the tube furnace. The general arrangement of the furnace is shown in Figure 3.1. The tube was sealed at both ends, with one end connected to a rotary pump and the other connected to a gas inlet. The furnace allows annealing from low temperature up to 1100 °C for a range of annealing

times with programmable heating and cooling rates. Gas flow rates can be controlled by mass flow controllers and the pressure was also managed through a pressure limiting valve. The sample was placed in a ceramic boat, which was placed in the middle of a sealed quartz tube. Details of annealing conditions are presented in each chapter as different annealing approaches are required to create different defect centers in ZnO.

Figure 3.1. Photograph of the annealing tube furnace.

3.3 Hydrogen doping

To probe the charge state of defects, the nanoparticles were doped with hydrogen. Hydrogen was chosen as the investigative plasma since it is known to exist exclusively as a positively charged donor in ZnO [150]. Consequently, it is expected to interact strongly with negatively charged defects and hydrogen passivates some peaks in the broad DL emission resulting in enhancement of the NBE. H-Doping was achieved by exposure to radio-frequency (RF) plasma in a vacuum chamber controlled by AG 0201HV-OS high voltage RF plasma power source. The basic setup is presented in Figure 3.2.

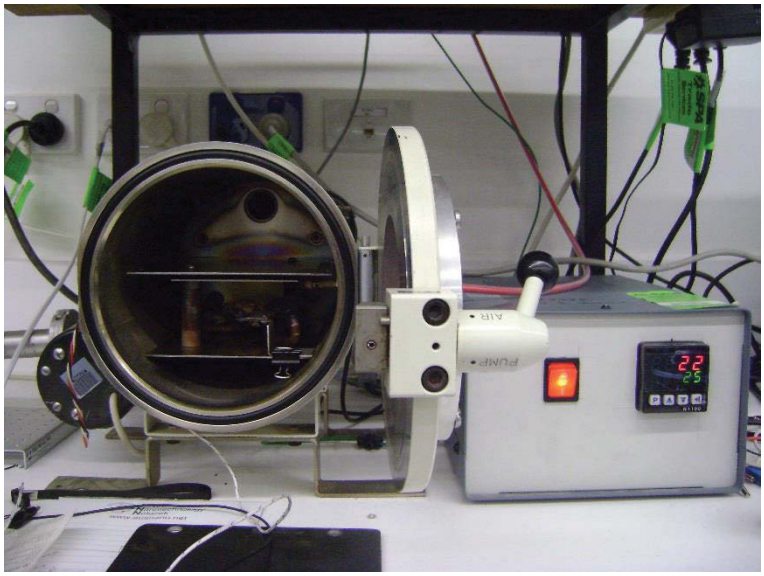

Figure 3.2. Schematic diagram of the plasma deposition chamber.

Annealed ZnO nanoparticles were put in the chamber which was evacuated with the pressure of ~ 10^{-1} torr. A constant pressure is monitored with a Lam research series capacitance diaphragm gauge. The stage was then heated up to 200 °C. As the temperature used throughout the plasma treatment process was kept constant at 200 °C or below, intrinsic defects were not produced due to the high formation energy.

Hydrogen gas (H_2) is flown into an evacuated chamber moderated using an Apex mass flow controller. A 10 standard cubic centimeters per minute (sccm) H_2 flow was also maintained across all samples. The chamber is equipped with a RF plasma source that ionizes the gas introduced into the chamber through the gas pipe connected to the gas cylinder. The plasma is generated using an AG 0202-HV OS high voltage plasma generator from T&C power/conversion, Inc. H_2 gas is ionized creating energetic radicals which penetrate into the sample and diffuse.

3.4 Characterization of ZnO

3.4.1 Scanning electron microscopy (SEM)

A SEM is used for high-resolution imaging of a sample to provide information of its composition, morphology and topography. [151]. The SEM morphology analysis was performed using a Zeiss Supra 55VP SEM high resolution field emission SEM operating in SE mode. The microscope was equipped with an in lens SE detector capable of 1 nm resolution. Images were collected at room temperature using an accelerating voltage of 15~20 kV.

3.4.2 Cathodoluminescence (CL) spectroscopy

3.4.2.1 Background

CL spectroscopy is one of the main analysis tools used in this project. CL is the phenomenon associated with the emission of light from the surface of a material when excited by an electron beam. Irradiation by a high energy electron beam will result in the promotion of electrons from the VB and into the CB, leaving behind holes. Following excitation the CB electrons quickly thermalize via phonon scattering and recombine with the holes in the VB, where the excess energy is conserved via photon or phonon emission. There are several radiative pathways for the electrons and holes to recombine which are illustrated in Chapter 2.

Band-to-band and excitonic emissions occur at the NBE, and the free-to-bound and DAP recombinations involve transitions at levels within the bandgap. So CL can be used to study excitonic behavior as well as to probe electronic states within the bandgap of a material. However, it is important to note that in CL is a competitive process dependent on the concentration of a recombination center, and can be either radiative or non-radiative.

The advantage of CL in electron microscopes over other optical measurement techniques is the high spatial resolution, which can be below 10 nm under optimal operating conditions. Moreover, CL depth information on a specimen can also be

obtained by varying the accelerating voltage (E_b) of the primary beam up to a few microns, and adjusting the beam current (I_b) to provide constant beam power ($E_b \cdot I_b$). Also, CL can be used to perform power density, depth-resolved, and temperature dependent measurements. As a result, with CL, the bandgap as well as various electronic states such as defect states in the bandgap of a semiconductor can be investigated at high spatial resolution in three dimensions.

3.4.2.2 CL measurement

Scanning CL can be conducted using a SEM equipped with a suitable light collection and optical spectrometer. In this work, the sample is placed at the focal point of a parabolic mirror which focuses the emitted CL onto a fiber optic cable, connected to either the OceanOptics QE65000 CCD spectrometer or the Oriel MS257 monochromator equipped with a Hamamatsu CCD. The OceanOptics spectrometer gives a luminescence ranging from ~ 200 nm to ~ 1000 nm which a spectral resolution of 1 nm. The monochromator system disperses the light emission to a variable wavelength range and the dispersed light is projected onto the Hamamatsu CCD sensor, which is attached to the lateral port of the monochromator. A schematic diagram of the system is given in Figure 3.3. The monochromator setup was used to investigate optical resonance behaviors of ZnO microdisks which were not able to be observed using OceanOptics spectrometer. The system used for CL imaging was an FEI Quanta 200 ESEM with a Gatan MONOCL3 system equipped with a liquid nitrogen cold stage for cooling samples down to 80 K. The collection conditions used in CL experiments can have a dramatic effect on spectra [152]. CL conditions used in this project vary significantly depending on the nature of the experiment. For this reason, collection conditions are presented in each chapter. Beam current was measured by using a Faraday cup.

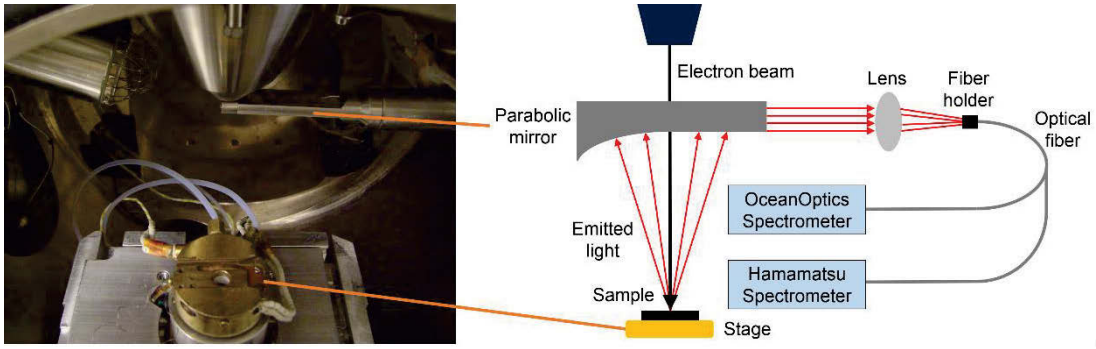

Figure 3.3. Diagram of SEM-based CL system.

3.4.3 Electron paramagnetic resonance (EPR) spectroscopy

Electron paramagnetic resonance (EPR) spectroscopy, also referred to as electron spin resonance (ESR), is a technique used to study materials with unpaired electrons using microwave energy. Thus, EPR is powerful technique to characterize defects in ZnO that contain an unpaired spin which is EPR active.

When a molecule or compound with an unpaired electron is placed in a strong magnetic field of strength B_o produced by a magnet in the laboratory, the spin of the unpaired (paramagnetic) electrons can either orient in a direction parallel m_s = -½ or antiparallel m_s = +½ to the direction of the magnetic field because the electron is a spin ½ particle, as can be seen in Figure 3.4(a). This creates two distinct energy levels for the unpaired electrons and this effect is known as the Zeeman Effect. The higher energy state arises when the magnetic moment of the electron, μ, is aligned against the magnetic field. On the other hand, the lower energy state occurs when the μ is aligned with the magnetic field. The energy of a magnetic moment (E) in a magnetic field can be expressed as the product of μ and B_o. For an electron spin magnetic moment is given by

$$\mu = m_s g \mu_B \tag{3.3}$$

where μ_B is the Bohr magnetron and g is the g-factor. For a molecule with one unpaired electron in a magnetic field, the energy states of the electron are given by

$$E = \pm\frac{1}{2} g\mu_B B_0. \tag{3.4}$$

Therefore, the separation between the upper and the lower state is determined as

$$\Delta E = (E+) - (E-) = g\mu_B B_0 = h\nu, \tag{3.5}$$

where h = Planck's constant, ν = the frequency of radiation. The g-factor is a unit-less measurement of the intrinsic magnetic moment of the electron. The equation indicates that the splitting of the energy levels is linearly proportional to the magnetic field's strength.

In EPR spectroscopy, the magnetic field is changed to collect an absorption spectrum, while the frequency of the radiation is kept constant. Electromagnetic radiation will be absorbed if the resonance condition $\Delta E = h\nu$, is obeyed, leading to Eq. 3.4. The absorption of this energy results in a transition of an electron from the lower energy (spin-down) state to the higher energy (spin-up) state. EPR spectrum is plotted by the absorption of microwave frequency radiation against the magnetic field intensity. A phase-sensitive detector is used in EPR spectrometer, causing the absorption signal being presented as its first derivative in the spectrum. Thus, absorption peak of the EPR spectrum corresponds to the point where its first derivative spectrum passes through zero which is the point used to measure the center of the signal. Figure 3.4(b) shows an example of EPR absorption spectrum and its first derivative. EPR spectroscopy was conducted for the investigation of electronic structure of point defects in ZnO nanoparticles. The condition details (temperature, power, and frequency) for the experiment are described in Chapter 4.

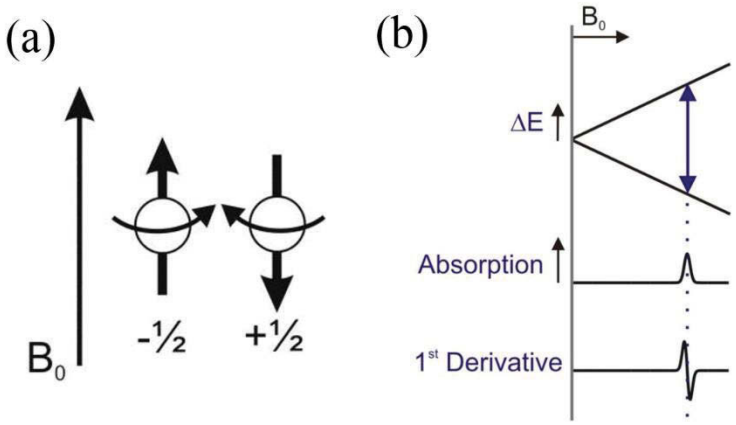

Figure 3.4. (a) Minimum and maximum energy orientations of magnetic moment μ with respect to the magnetic field B_0. (b) EPR absorption spectrum. The middle spectrum is the absorption spectrum in a varying magnetic field and the bottom spectrum is the first derivative of its absorption spectrum [153].

3.4.4 X-ray diffractometry

X-ray diffraction (XRD) is a useful technique that examines detailed information about the crystallographic structure of samples. Constructive interference of diffracted x-ray occurs when Bragg's law is satisfied. The Bragg's law is defined as

$$2d \sin\theta = n\lambda \tag{3.6}$$

where d is interatomic spacing in Angstroms which is usually called d-spacing, θ is the diffraction angle in degrees, n is an integer, and λ is wavelength in angstroms. In XRD experiments the intensity of x-rays arriving at the detector is measured as a function of 2θ which is the total angular displacement of the x-ray. Maxima in the intensity profile correspond to crystal planes meeting the Bragg condition in Eq. 3.6. A schematic diagram of the XRD is shown in Figure 3.5. The x-ray diffractometer consists of an x-ray source (usually an x-ray tube), a sample stage, a detector, and a way to vary the angle θ. The x-ray beam is focused on the sample at some angle θ, while the detector opposite the source reads the intensity of the x-ray that receives at 2θ away from the source path. The incident angle is increased over time while the detector angle always remains 2θ above the source path.

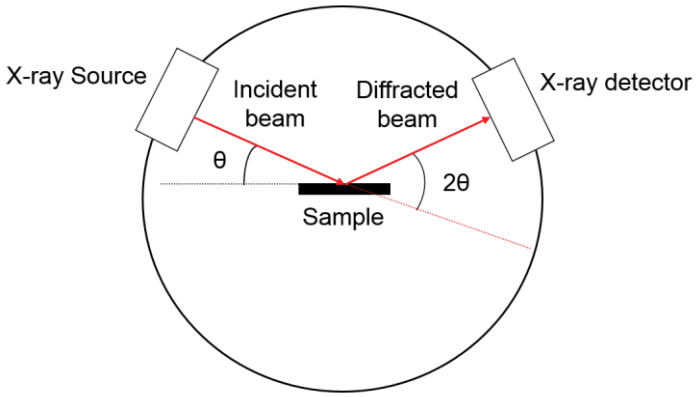

Figure 3.5. Schematic diagram of x-ray diffractometer.

3.4.5 X-ray near absorption edge spectroscopy (XANES)

In order to probe core levels within atoms, high energy x-rays are needed. In this project, XANES measurements were performed at the Soft X-ray Beamline of the Australian Synchrotron.

XANES measures the absorption of x-rays as a function of x-ray photon energy. As it probes the unoccupied electron states in the energy level above the selected atomic core level ionization energy, XANES provides information of conduction hand, oxidation state and transitions from the core level to an unoccupied states of elements in a sample. Two different types of defection modes can be obtained: total electron yield (TEY) and total fluorescence yield (TFY). TFY measures the emitted photons that give information about the bulk sample due to the long mean-free-path of photons. TEY on the other hand collects the neutralization current flowing into the sample. Generally, TEY measurement probes the surface of a material due to the short mean-free-path of electrons and is sensitive to sample charging. In this project, TEY mode was used during the measurements and details of the conditions are described in Chapter 4.

3.4.6 Confocal microscopy

The confocal microscopy provides a major improvement in optical microscopy scientific disciplines developed. The principle of confocal imaging was developed in

1957 by Marvin Minsky. In a conventional wide-field optical fluorescence microscope, a sample is completely illuminated by the excitation light, so entire area of the sample is fluorescing at the same time. The highest intensity of the excitation light is at the focal point of the lens, but nonetheless, the other parts of the sample do get some of the light and they do fluoresce. Thus, the fluorescence emitted by the specimen obscures resolution of features due to a large amount of unfocused light. This is most pronounced in thick three-dimensional specimen, where the most of the fine detail is absent. Conversely in confocal microscopy only light emission close to the focal plane is collected and thus optical resolution and contrast of an image is enhanced with confocal microscopy over conventional far-field techniques. The basic principle of the confocal microscopy is that a confocal microscope is able to exclude out-of-focus fluorescent light in areas from resulting images due to a confocal pinhole in front of the detector. This approach enables to obtain sharply distinct optical sections from which three-dimensional structures can be imaged at high spectral resolution.

In a typical confocal microcopy, laser excitation source passes through a pinhole aperture that is positioned in a confocal plane with a scanning point on a sample, and a second pinhole aperture is placed in front of the photomultiplier detector. The microscope uses a dichroic mirror which reflects light shorter than a certain wavelength, and passes light longer than that wavelength. As the laser is reflected by the dichroic mirror and scanned across the sample focal plane, emitted light from points on the sample in the same focal plane pass back through the dichroic mirror and is focused as a confocal point at the detector pinhole aperture to form an image.

3.4.6.1 Second order autocorrelation function ($g^2(\tau)$)

Second order autocorrelation function, $g^2(\tau)$, is used to observe SPSs from a material. $g^2(\tau)$ describes the intensity correlation of the fields at two different time-space points and classifies in which the light is described as antibunched, coherent, or bunched light. Antibunched light is clear signature of the quantum nature of light. $g^2(\tau)$ is defined as

$$g^2(\tau) = \frac{\langle \varepsilon^*(t)\varepsilon^*(t+\tau)\varepsilon(t+\tau)\varepsilon(t)\rangle}{\langle \varepsilon^*(t)\varepsilon(t)\rangle\langle \varepsilon^*(t+\tau)\varepsilon(t+\tau)\rangle} = \frac{\langle I(t)I(t+\tau)\rangle}{\langle I(t)\rangle\langle I(t+\tau)\rangle} \tag{3.7}$$

where $\varepsilon(t)$ and $I(t)$ are the electric field and intensity of the light beam at time t. The bracket symbols again indicate the time average computed by integrating over a long time period (expectation values). If we consider a source with constant average intensity, $<I(t)>=<I(t+\tau)>$, $g^2(\tau)$ can be written as Eq. 2.4 which is $g^2(\tau) = \langle I(t)I(t+\tau)\rangle / \langle I(t)\rangle^2$.

For antibunched light, only one photon arrives into a detector at given time t, thus the value of $g^2(\tau)$ becomes less than 1, sub-Poisson photon statistics. Based on the quantum mechanical theory of light in second quantization, $g^2(\tau)$ at the zero time-delay correlation can be expressed as

$$g^2(0) = \frac{n(n-1)}{n^2} \tag{3.8}$$

where n is the photon number. For a true single photon emitter, no more than one photon can be detected at any given time, $n = 1$, and subsequently $g^2(0) = 0$.

3.4.6.2 Hanbury Brown and Twiss (HBT) setup

In order to investigate antibunching behavior, a HBT interferometer is used. The HBT experiment gives a direct measurement of $g^2(\tau)$ in the photon interpretation of light. The HBT measures correlation of light emissions received by two detectors from a stream of light particles. Figure 3.6(a) shows a schematic diagram of the HBT system. Firstly, a stream of photons is incident on a 50/50 beam splitter, and is divided into two output paths. The beam splitter outputs are connected to two APDs for the photon detection, instead of photomultiplier tubes. The outputs of the APDs are then connected to the start and the stop inputs of a correlator card. When a photon reaches one of the APDs, the correlator records the time interval between a pulse detection at an APD, ("start") and a subsequent detection at the other APD ("stop"), while simultaneously counting the number of pulses at each input. The results of the coincident events are presented as a histogram as a function of time delays between two consecutive photon detections, Figure 3.6(b) shows a histogram that exhibits the number of events recorded at each time delay between the start and the stop pulse. Note that in practice, a delay is placed in the stop channel.

Since the number of counts registered on a photon counting detector is proportional to the intensity, the definition of $g^2(\tau)$ can be rewritten as:

$$g^2(\tau) = \frac{\langle n_1(t) n_2(t+\tau) \rangle}{\langle n_1(t) \rangle \langle n_2(t+\tau) \rangle} \tag{3.9}$$

where $n_i(t)$ is the number of counts registered on detector i at time t. This shows that $g^2(\tau)$ is proportional to the conditional probability of detecting a second photon at time $t = \tau$, given that one photon is detected at $t = 0$.

If a true single photon emitter is emitted, only one photon is incident on the beam splitter at a time ($t = 0$). Multiple photons do not exist at the same time since one photon cannot be divided. Hence there is a 50 % probability that the emitted photon will be detected one of the APDs and activate the timer to start recording. The triggering of a start pulse in the APD indicates that there is a 0 % probability of obtaining a stop pulse from the other APD from this photon due to only one photon emission. That means the joint probability of equal time photo detection at the two detectors will be zero. Thus the timer will record no events at $\tau = 0$. The process continues until a stop pulse is achieved. The stop pulse will be recorded at larger values of τ, but never at the time of $t = 0$. The result of the coincident statistics will be a dip at $t = 0$. The obtained curve of the statistics events is generally known as "antibunching" curve, shown in Figure 2.6(a) and 2.6(b). The absence of the peak at zero delay time, $g^2(0) = 0$, indicates that the source is a true SPS. Antibunched light is a purely quantum state with no classical equivalent: However, in our experimental setup, there is always background emission present which causes the slight deviation from an ideal SPSs, giving $0 < g^2(0) < 0.5$.

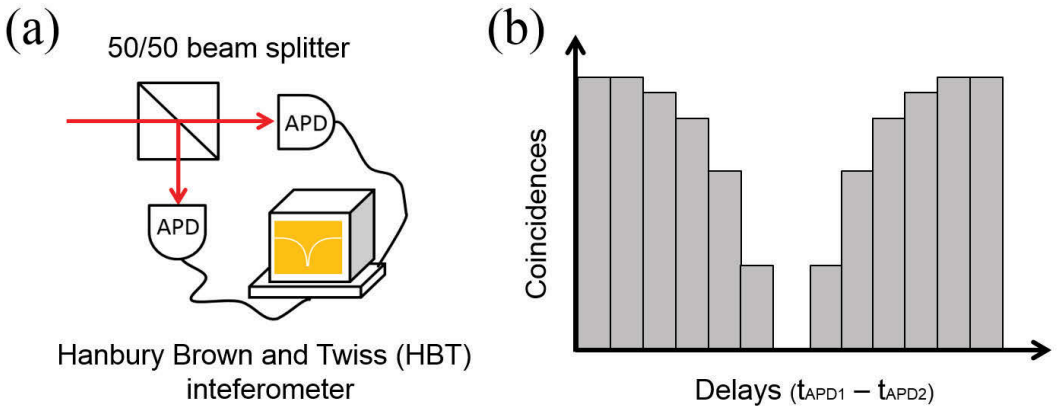

Figure 3.6. Schematic illustration of a HBT experiment with a photon stream incident on the beam splitter. (a) The beam splitter directs the incoming photons to two APDs. The APDs are connected to a correlator card, which records the time elapses between the start and the stop pulses. (b) A histogram of an experiment from a true single photon emitter, showing the number of events recorded within a particular time interval.

3.4.6.3 Single photon source (SPSs) measurement

Measurements of SPSs were performed using a confocal microscope with HBT interferometer and PL spectroscopy at room temperature. The overall structures are illustrated in Figure 3.7. A CW of 532 nm green laser was used in the project and the excitation power was changed using a variable neutral density filter. ZnO sample was mounted on a movable XYZ stage. A high numerical aperture (0.9) objective lens was used and the confocal excitation spot size was ~ 600 nm. The laser is collimated and excites the sample through the objective lens which also collects the emitted light. The emission and residual laser line was filtered by a dichroic beam splitter and a band-pass filter centered at 572 nm. The emitted light passes through the dichroic and is focused onto a pinhole in front of a detector. The light that passes through the pinhole and a 50:50 fiber-coupled beam splitter guided the light to the both APDs, providing an aperture for the confocal imaging. Then their outputs were sent to the start and stop inputs of the time correlator card. The correlator card is attached to a computer which builds up the image, one pixel at a time. Once the scanning mirror scans many thin

sections through a sample, a confocal image of the sample can be obtained. The laser polarization was controlled by a half-wave plate. The PL from the emission was coupled into a 62.5 nm core multimode fiber, which acts as an aperture. The PL was recorded using a fiber-couple spectrometer with a cooled CCD array.

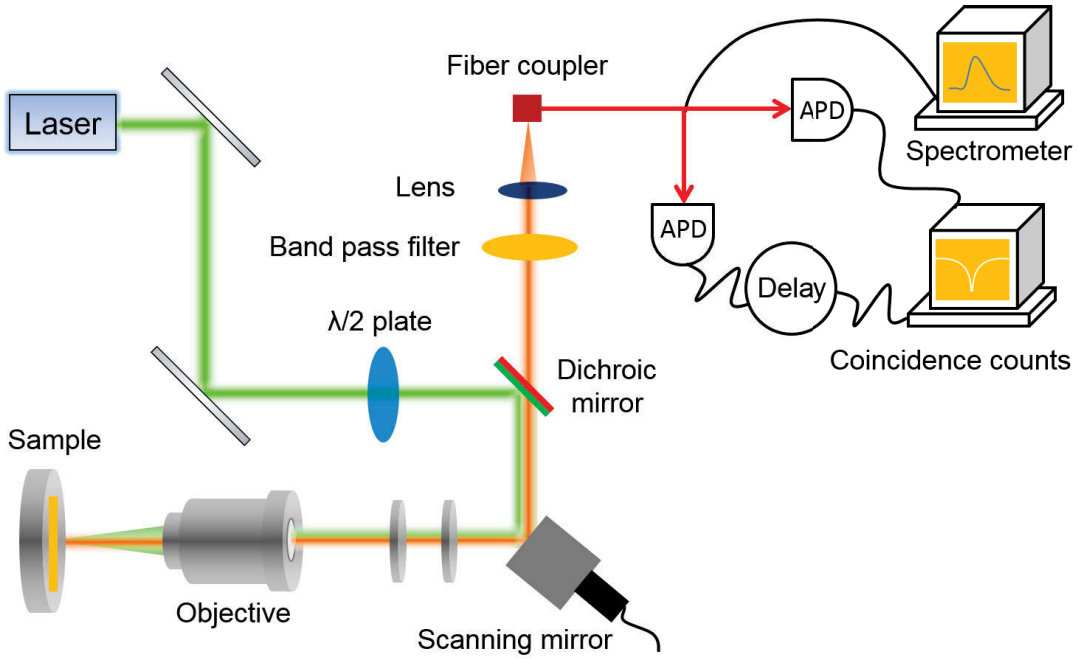

Figure 3.7. Experimental setup of measurements of SPSs using a customized confocal microscope with HBT interferometer operating at room temperature. A CW laser at 532 nm is used and a variable neutral density filter was used to change the excitation power. The fluorescence emission was collected with a microscope objective lens. The emitted light passes through a dichroic mirror, band-pass filter, and is focused onto a pinhole. The laser polarization was varied by a half wave (λ = ½) plate. The light was coupled into a multi-mode fiber and sent to two APDs and a PL spectrometer.

3.4.7 Raman spectroscopy

Raman spectroscopy has proven to be an effective and non-destructive characterization to investigate the lattice dynamics of materials. The experimental Raman system (Renishaw in Via Raman Spectrometer) is a compact single-grating (1800 lines per mm) Raman spectrometer system equipped with microscope optics (Leica DMLB microscope). This system provides a spectral resolution about 1 cm^{-1}. To avoid effects

due to the laser heating: (i) a 632.8 nm line of a Renishaw He-Ne laser was used as excitation wavelength. (ii) a lens with only 5 times magnification was used, and (iii) the excitation power was kept under 6 mW. The ZnO samples were put under microscope objective lens, the laser was focused on the samples, and then the parameters such as time, power, and spectral range were set.

Chapter 4

Photophysics of point defects in ZnO nanoparticles

ZnO nanoparticles have recently been identified as a promising candidate for advanced nanophotonic applications and quantum technologies. In this chapter, the formation of luminescent point defects and their photophysical properties will be described. This work provides important knowledge towards employment of point defects in ZnO in nanophotonic technologies.

4.1 Introduction

ZnO offers attractive optical, mechanical and electronic properties, including a large exciton binding energy, a high dielectric constant, high carrier saturation velocity, piezoelectric behavior and low lasing density threshold [118]. ZnO can also be grown into a variety of different nanostructures such as nanoparticles, nanowires, and nanobelts. Fabrication of ZnO nanostructures is quite simple promoting it for inexpensive nanotechnology devices such as environmentally friendly, high efficiency lighting solutions. These nanostructures, due to large surface to volume ratio, are also ideal for gas sensing applications, and would be potential building blocks of nano-scale electronic components.

One of the most fascinating applications of ZnO is its ability to host bright fluorescent defects that exhibit luminescence across the entire visible range, facilitating extensive applications in lighting technologies [6, 7]. Thus, it is important to understand the origin of the emissions related to DL defects in ZnO for the development of optoelectronic devices with high efficiency. The origin of the observed near-UV lines

was identified as bound exciton complexes and their phonon replicas due to emission of a single optical phonon or multiple phonons [9]. While it is widely acknowledged that substitutional Li_{Zn} (a common impurity in hydrothermal growth) introduces a deep ~ 60 meV acceptor level and is responsible for YL [54, 55], the chemical origin of GL remains highly controversial. Earlier works attributed the GL to several native defects including V_O [56] V_{Zn} [154], interstitials (Zn_i, O_i) [51] and antisite defects (Zn_O, O_{Zn}) [57] as well as chemical impurities such as Cu [155]. With advances in nanotechnology and the decreasing size of electronic components, surface effect may dominate the properties of future of nano-scale structures. In order to consistently produce ZnO with useful and reproducible properties, a comprehensive knowledge of the dominant defects is crucial.

The need to characterize point defects in ZnO is further amplified with the recent applications of ZnO nanoparticles as hosts of single emitters for quantum information processing [11, 12] and their use in random lasing [156] and other advanced sensing technologies [13]. These applications require precise control over the defect engineering of ZnO nanoparticles. Consequently, correlative characterization of point defects will be valuable to explore the luminescence properties and affiliate them with their chemical and paramagnetic spin features.

In this chapter comprehensive studies on the formation and photophysical properties of point defects in ZnO nanoparticles are performed. Because of the larger surface-to-volume ratio, the properties of nanoparticles primarily reflect the properties of the surface. The surface can have unique and novel properties, as well as large concentrations of native defects. 20 nm nanoparticles were chosen since at this size the surface-to-volume ratio would be significant, however, they were large enough to avoid quantum size effects as the Bohr exciton radius of ZnO is 2.34 nm [157]. Annealing of ZnO nanoparticles are performed to investigate the origin of different emissions in ZnO. To date, annealing studies of ZnO nanoparticles have not been investigated systemically over a wide range of temperatures and various gas atmospheres. The control of the optical emission of ZnO nanoparticles and the structural quality by the annealing process in the nanostructures are crucial for future

ZnO nanophotonic devices. Correlative characterization techniques are employed to assign the optical emission peaks and EPR lines to specific defects in ZnO nanoparticles. The results provide new insight into optical luminescence properties of ZnO nanoparticles and promote them as potential candidate for nanophotonic technologies [16].

4.2 Generation of point defects in ZnO nanoparticles

4.2.1 Annealing process on ZnO nanoparticles

To generate the defects within the ZnO nanoparticles (Nanostructured and Amorphous Materials Inc., USA), several annealing treatments were applied. ZnO nanoparticles were first annealed for 1 hour at temperatures between 400 °C up to 900 °C in pure O_2 and Zn vapor with a flow rate of 20 sccm at a pressure of 1 atm. The Zn vapor ambient was generated using a metallic Zn source held just above its melting point (420 °C) upstream from the ZnO nanoparticles. When the samples were annealed in metal Zn vapor atmosphere, the metal zinc was placed at a few centimeters away from the middle of the furnace depending on the annealing temperature. The position of boat containing metal Zn kept remain constant at around 420 °C to produce similar amount of Zn vapor. To keep the temperature of metal Zn constant, the furnace temperature was measured by using thermocouple in 2 cm steps (center to 20 cm from the middle of the furnace) (Figure 4.1). After measuring the temperature range, 2 g of metal Zn in the boat was placed the position at which the temperature was around 420 °C. An Ar gas was used as the carrier gas and flow rate was 20 sccm during the annealing.

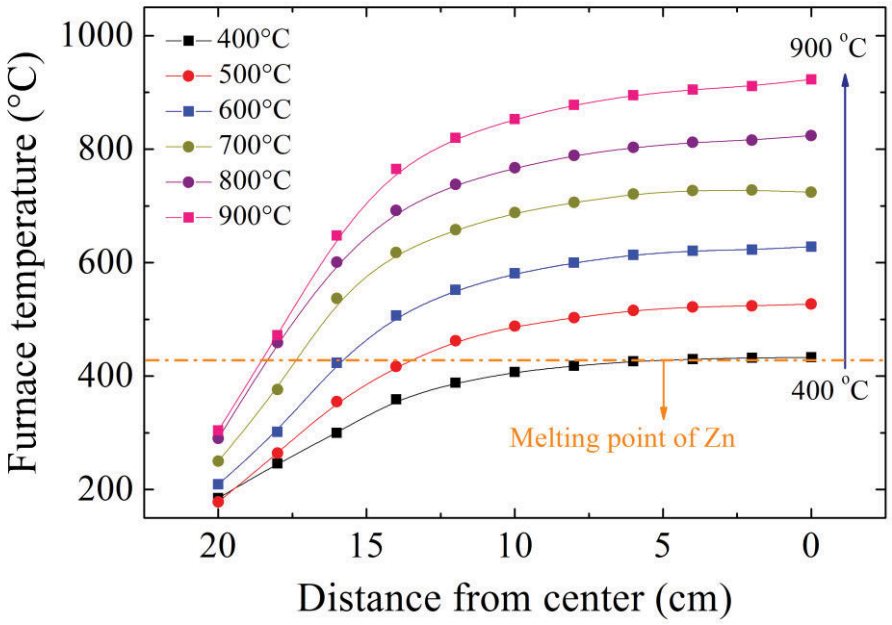

Figure 4.1. Temperature inside the furnace depending on the annealing temperature. A red horizontal line is the melting point of Zn which is 419.6 °C.

Annealing conditions are shown in Table 4.1. Samples were cooled to 80 °C before being removed from the furnace to prevent reaction with the atmosphere at elevated temperatures.

Atmosphere	Temperature	Time	Pressure	Gas flow
Argon	400 °C to 900 °C in each 100 °C step	1 hour	~ 2 torr	Argon 20 sccm
Oxygen				Oxygen 20 sccm
Zinc				Argon 20 sccm

Table 4.1. Annealing conditions in this experiment.

4.2.2 Hydrogen doping on annealed ZnO nanoparticles

In this experiment, RF power 15 W (175 V) was used to create hydrogen radicals, which was lower than the voltage used for DC ion implantation. As the RF power and treatment time was minimized, the possibility of surface damage through the lattice structure of the ZnO samples was avoided. The hydrogen plasma treatment on the samples was done for 3 minutes. After plasma processing the sample was cooled in an

H atmosphere to less than 50 °C before removal from the chamber for analysis. As mentioned above, during the treatment the gas flow rate and sample temperature were kept constant. The reactant gas was leaked into the chamber through a mass flow controller, and temperature and chamber pressure were controlled and monitored by a computer running a custom LabVIEW program.

4.3 Characterization of ZnO nanoparticles

4.3.1 Structural characterization

XRD measurements were performed with a Siemens D5000 diffractometer using CuKα radiation source λ = 1.54056 Å. Scans were taken in the range 25° < 2θ < 80° with a step size 0.01° and dwell time 1.25 s. Structural analysis was performed using the XRD. The EPR measurements were made using a Bruker Elexys E500 cw X-band EPR spectrometer equipped with an Oxford ITC605 temperature controller. All presented EPR spectra were collected at 10 K using a power of 2.0 mW with a modulation amplitude of 5.0 G and a frequency of 9.4 GHz. The local surface electronic structure around Zn and O atoms in ZnO nanoparticles before and after annealing process was studied using an XANES. XANES implemented in the TEY mode was performed around the Zn L_3-edge and O K-edge on the Soft X-ray Spectroscopy beamline, Australian Synchrotron. The photon energy scale was calibrated against the Au $4f_{7/2}$ peak at 84 eV from a clean gold film in electrical contact with samples.

4.3.2 Optical characterization

The samples were characterized by CL spectroscopy at 80 K using a FEI Quanta 200 Environmental SEM equipped with a liquid nitrogen cold stage and an Ocean Optics SD2000 Diode Array Optical Spectrometer. For CL measurements, the accelerating voltage was fixed at 15 kV and the electron beam current was 0.25 nA. All spectra were corrected for the total response of the light collection and measurement system.

In order to investigate the sub-bandgap excitation, PL spectra of the annealed ZnO nanoparticles were collected using a home built confocal microscope with 500 nm resolution. The excitation was performed using a CW laser (λ = 405 nm and 532 nm) through a high numerical aperture (NA = 0.9) objective. The signal was collected using the same objective and directed into a spectrometer (Princeton Instruments, 300 lines/nm grating). For the time-resolved measurements, a picoseconds pulsed laser (λ = 405 nm and 514 nm, repetition 20 MHz) was employed. The signal was recorded using an APD (Excelitas, SPCM-AQRH-14) and analyzed using a TCSPC (PicoHarp 300) with 64 ps resolution. In all cases, a dichroic mirror was used to filter the excitation laser, and a band-pass filter to select only the defect emission. The sub-bandgap measurements were done at room temperature.

4.4 Structural properties of ZnO nanoparticles

4.3.1 Morphology of annealed ZnO nanoparticles

A range of properties of ZnO nanoparticles were investigated after annealing processing. SEM images of the annealed ZnO nanoparticles are shown in Figure 4.2. After being annealed in an Ar or Zn vapor environment at 700 °C – 900 °C the as-received ZnO nanoparticles (diameter ~ 20 nm) coalescence [158, 159] and display faceted morphologies. The nanoparticles increase in average size up to about 120 nm after annealing in inert gas (Ar) or oxygen, and up to 150 nm for annealing in Zn vapor at 900 °C. The tendency for nanoparticles to form clusters is well known and is related to excess surface energy. Since the Bohr radius of ZnO is 2.34 nm, the nanoparticles are large enough to avoid quantum size effects but still possess a sufficiently large surface area to allow defect engineering.

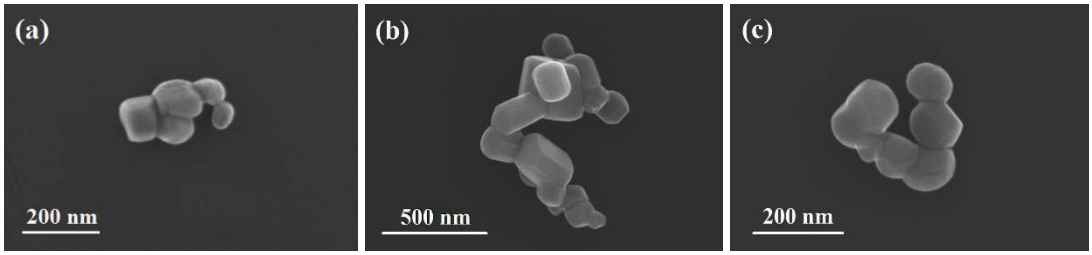

Figure 4.2. SEM images of the ZnO nanoparticles annealed at (a) 700 °C in Zn vapor (b) 900 °C in Zn vapor, and (c) 900 °C in Ar. The annealed nanoparticles exhibit highly faceted morphologies and enlargement from the 20 nm as-received size.

4.3.2 XRD analysis of ZnO nanoparticles

The XRD patterns of as-received ZnO nanoparticles and ZnO nanoparticles annealed at temperatures between 400 °C and 900 °C are shown in Figure 4.3. The nanoparticles show typical powder diffraction for a wurtzite crystal and all peaks are indexed to ensure they originate from ZnO without any impurity phase. With increasing the annealing temperature, the intensities of the diffraction peaks increase and become narrower with smaller FWHM, indicating better crystallinity. A sharp peak at (201) occurred at 900 °C annealing could come from the Si wafer due to the different coverage of the ZnO nanoparticles or the nanoparticles may get sintered and preferentially oriented in (201) direction.

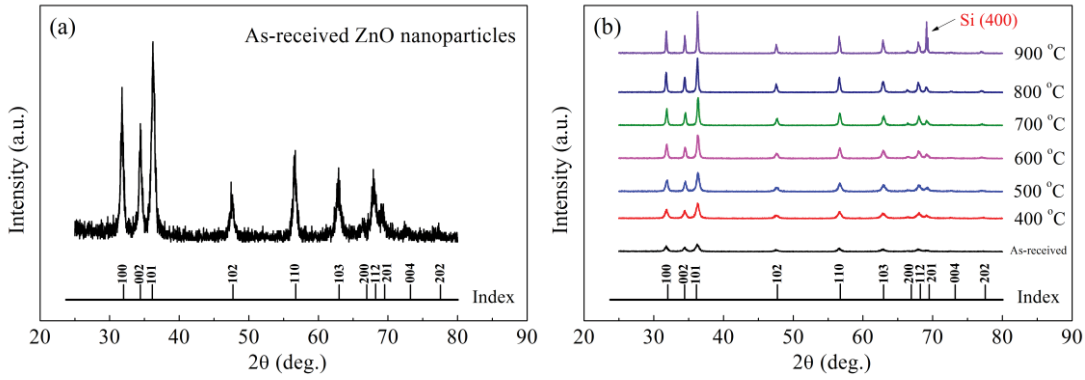

Figure 4.3. XRD patterns of (a) as-received and (b) Zn-annealed ZnO nanoparticles in a range of annealing temperature between 400 °C and 900 °C. The diffraction peaks increase in intensity and become sharper with increasing annealing temperature.

XRD is utilized to evaluate peak broadening due to crystallite size and lattice strain using the Williamson-Hall (W-H) method, which evaluates the peak width, β_{hkl}, as a function of diffracting angle θ. The expression is

$$\beta_{hkl}\cos\theta = \frac{k\lambda}{D} + 4\varepsilon\sin\theta \tag{4.1}$$

where β_{hkl} instrumental corrected integral breadth of the reflection (in radians) located at 2θ, θ is the diffracted angle, k is the Scherrer constant (0.9) [160], λ is the wavelength of the x-ray, D is particle size, and ε is strain [161]. The peak width (β_{hkl}) is defined as

$$\beta_{hkl} = \frac{1}{I_{max}}\int I(2\theta)d2\theta \tag{4.2}$$

which the integrated intensity of a diffraction peak is divided by the peak maximum (I_{max}) [162]. Instrument broadening was subtracted from the data for the W-H method.

A plot is drawn with 4sinθ along the x-axis and $\beta_{hkl}\cos\theta$ along the y-axis for ZnO nanoparticles. Among 11 XRD peaks, first nine peaks ((100), (002), (101), (102), (110), (103), (200), (112) and (201)) are used to do W-H analysis since last 2 peaks ((004) and (202)) are too weak to measure the integrated intensity. From the linear fit to the data, the crystallite sizes of the ZnO nanoparticles are extracted from the y-intercept and the strain ε from the slope of the Eq. 4.1, where the y-intercept is $\frac{k\lambda}{D}$ and the slope is ε. Figure 4.4(a) and 4.4(b) present the W-H analysis of the as-received ZnO nanoparticles and annealed ZnO nanoparticles at 900 ^{o}C. From the linear fit to the data, the crystallite size was extracted from the y-intercept. Figure 4.4(c) and 4.4(d) shows the crystallite size of Zn- and Ar-annealed ZnO nanoparticles as a function of annealing temperature. The evaluated particle size for the as-received ZnO nanoparticles is 20 (± 5) nm. The crystallite size obtained using the W-H method is within the experimental errors of the diameter that was measured directly by SEM in Figure 4.2. The particle size increases with annealing temperature, evident of crystal growth by coalescence of smaller nanoparticles. The numerical data of particle sizes of annealed ZnO nanoparticles are also shown in Table 4.2. The degree of orientation of the ZnO nanoparticles is strongly dependent on the annealing temperature. It

increases as the annealing temperature increases. This result can be explained by the fact that annealing provided energy of ZnO atoms to increase atomic mobility, enhancing the ability of atoms to find the most energetically favored sites. Sintering of ZnO nanoparticles can also happen because the powdered material was held in a mold and then heated to a temperature below the melting point (1,975 °C), resulting in some agglomeration along with individual particles and consequently particle size increases [163].

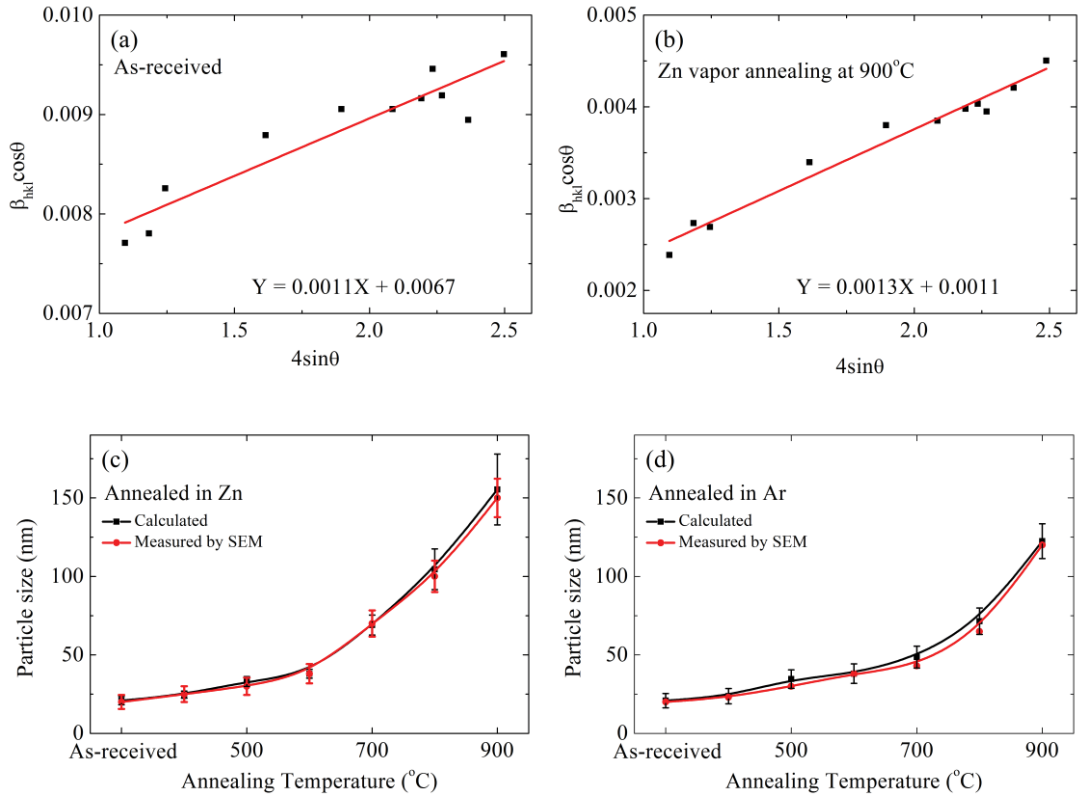

Figure 4.4. The W-H analysis of (a) as-received ZnO nanoparticles and (b) Zn vapor annealed ZnO nanoparticles at 900 °C. The W-H plot is used for the determination of particle crystalline size. Variations of nanoparticle size with annealing temperature in (c) Zn vapor and (d) Ar gas as determined by the W-H method and SEM image analysis.

Annealing Temperature(°C)	As-received	400	500	600	700	800	900
Calculated Particle size(nm)	20±5	24±3	32±8	35±7	40±10	53±11	128±50
Estimated Particle size(nm)	20	20-25	25-35	35-40	40-45	50-70	100-150

Table 4.2. Particle sizes depending on the annealing temperature.

4.5 Electronic properties of ZnO nanoparticles

4.5.1 EPR investigation

To investigate the occurrence of defects in ZnO nanoparticles, EPR spectroscopy was performed. Figure 4.5 shows EPR spectra of the as-received, O_2 annealed, Zn vapor annealed ZnO nanoparticles and a bare Si(100) substrate for comparison. The as-received ZnO nanoparticles exhibit a strong signal at g = 1.96, which has been previously assigned to single ionized zinc vacancies (V_{Zn}^{-}) [164], O_i^{-} [164], Zn_i^{+} [165] and electrons in weakly bound or CB states arising from different donor impurities, such as Ga, In, Al [166, 167] and H [168]. A weak signal is also present at g = 2.00, which has been attributed to V_O^{+} [169]. An EPR signal from a V_O^{+} center was unexpected as the reported EPR signal at g = 2.00 occurs during photo-ionization of neutral oxygen vacancies, V_O^{0}. Computational DFT modeling has shown that the V_O center in bulk ZnO behaves as a negative U center and consequently will either spontaneously capture or emit an electron, converting to V_O^{0} or V_O^{2+} center, respectively [41]. Consequently the presence of the g = 2.00 line in the as-received ZnO nanoparticles indicates that its chemical origin is likely related to singly ionized surface oxygen vacancy centers, $V_{O,s}^{+}$.

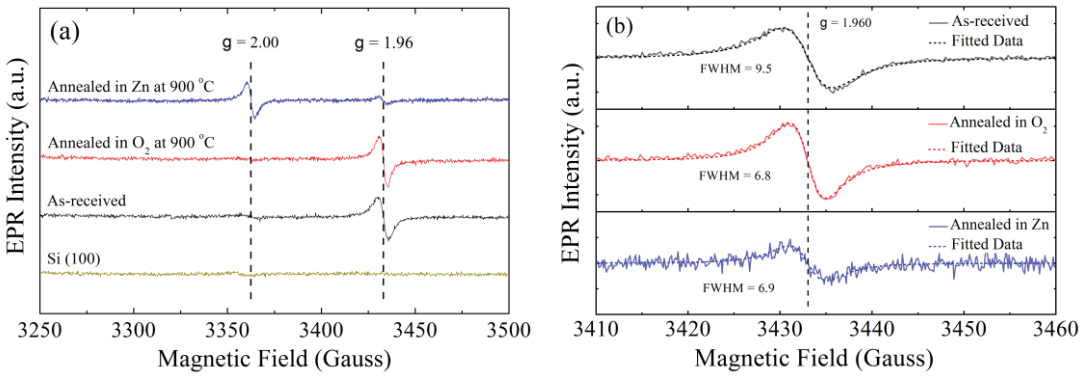

Figure 4.5. (a) EPR spectra of as-received, O_2 annealed, Zn vapor annealed ZnO nanoparticles and a bare Si(100) substrate for comparison. Two main types of paramagnetic signals at g = 2.00 and g = 1.96 are observed, corresponding to $V_{O,s}^{+}$ defects and localized donors, respectively. (b) Magnified EPR spectra of the g = 1.96 line for the as-received and annealed ZnO nanoparticles, showing a decrease in the EPR linewidth after annealing.

Upon annealing in O_2, the weak signal at g = 2.00 vanishes consistent with its assignment to $V_{O,s}^{+}$ defects. Conversely the g = 1.96 slightly increases due to an improvement in crystal quality. This result also suggests its assignment to Zn_i or H donors unlikely. Both of these particular defects are highly mobile in ZnO [170, 171] and should be annihilated by surface reactions with the O_2 gas during annealing. The thermally induced EPR changes could arise from the stronger presence of V_{Zn} which are created by via chemical surface reactions with gaseous oxygen at elevated temperatures. However, more recent studies have concluded that the EPR signatures for V_{Zn} related centers are located around g = 2.02 [172]. Accordingly, the g = 1.96 line is attributed to the presence of localized donor states as suggested by other workers [167].

As shown in Figure 4.5(a) annealing in Zn vapor produced a strong line at g = 2.00 which can be attributed to formation of $V_{O,s}^{+}$ as described above. This result can be explained by (i) the rapid coalescence of the nanoparticles in an oxygen deficient atmosphere at elevated temperatures [158], as shown in Figure 4.2 above, leading to the formation of V_O and (ii) surface chemical reactions with Zn vapor that remove

oxygen from the surface. In contrast the $g = 1.96$ peak intensity was dramatically reduced after annealing in Zn vapor. This result can be explained by the thermal displacement of donors on Zn sites by Zn_i or via the formation of ionized donor - zinc interstitial defect pairs (D^+ - Zn_i^+) [173]. A Lorentzian line shape was used to fit the g = 1.96 EPR peaks shown in Figure 4.5(a) to compare their FWHM. Figure 4.5(b) shows the fitted EPR spectra, which shows the FWHM decreasing from 9.5 to ~ 6.8 Gauss after annealing. The narrow EPR lines after annealing indicate an improvement in the crystal quality which increases the average spin-spin distance [174].

4.5.2 XANES investigation

To gain greater insight into the formation of the point defects before and after thermal annealing, XANES measurements were used to probe the local electronic structure of O and Zn atoms in the nanoparticles (Figure 4.6). The Zn L_3-edge spectra before and after annealing in O_2 or Zn vapor environments are shown in Figure 4.6(a). These spectra exhibit three peaks labeled A_1, B_1, and C_1 at 1022.7 eV, 1024.3 eV, and 1028.9 eV, respectively, which mainly reflect the electron transitions from Zn $2p_{3/2} \rightarrow 4s$, $5s$ and Zn $2p_{3/2} \rightarrow 3d$ derived states in the CB [175]. The Zn L_3-edge spectra are virtually identical in all three samples, indicating that the atomic configurations of Zn atoms are unaffected following the coalescence of nanoparticles. This result confirms that no additional Zn-related defects such as Zn interstitials are introduced during Zn vapor annealing presumably because of the high mobility of Zn_i.

Figure 4.6(b) shows the O K-edge XANES of the ZnO nanoparticles, which were normalized in the energy range of 550 eV - 555 eV. The spectra show five resolvable features labeled A_2, B_2, C_2, D_2 and E_2 at 533.5 eV, 536.5 eV, 539.0 eV, 542.0 eV, and 544.6 eV, respectively. The spectral features predominantly reflect the O $2p$ unoccupied states and their hybridization with Zn orbitals. Features A_2 and B_2 are mainly attributable to the hybridization of O $2p$ and highly dispersive Zn $4s$ in ZnO [176]. Features C_2, D_2 and E_2 are attributed to electron transitions from O $1s$ to unoccupied O $2p$, hybridized with Zn $4p$ and $4d$ states [177, 178]. Upon annealing in Zn vapor, the intensities of C_2, D_2 and E_2 increase significantly. It has been recently

established that stronger antibonding interactions of O 2*p* and Zn 4*p* states are formed due to a lattice distortion caused by V_O which affects its shell of surrounding O atoms [179]. Consequently, the increase in C_2, D_2, and E_2 features are attributed to the presence of a high concentration of surface *Vo*, supporting the EPR g = 2.00 assignment to these centers. This interpretation is consistent with the work of Krishnamurthy et al. [180].

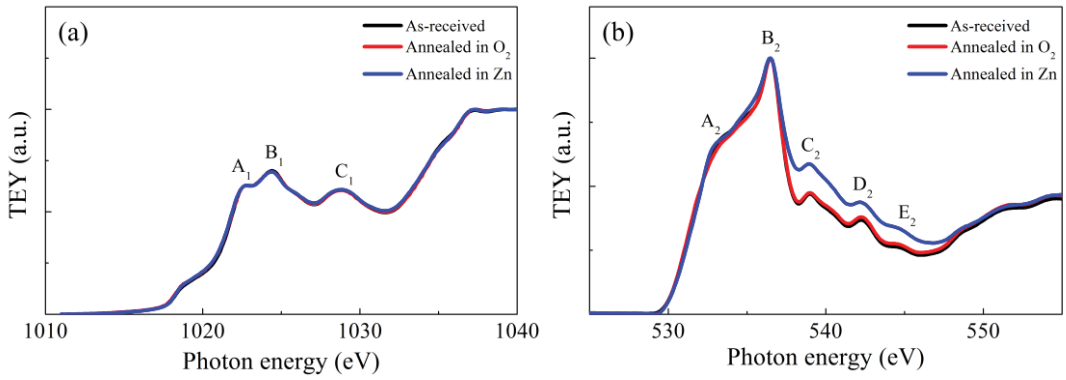

Figure 4.6. Normalized (a) Zn L_3-edge and (b) O *K*-edge XANES spectra of ZnO nanoparticles annealed at 900 °C under O_2 and Zn vapor. The spectra were collected in surface sensitive TEY mode (probing depth is ~ 5 nm). No additional Zn-related defects were produced during annealing, however, *Vo* is formed in Zn vapor anneal.

Nanoparticles annealed in Zn vapor at 700 °C show similar behavior. Figure 4.7 shows the effects of annealing at 700 °C on the atomic configurations of Zn and O atoms in nanoparticles. There are no variations in the Zn L_3-edge spectra following annealing; however, surface *Vo* are formed when the nanoparticles are annealed in Zn vapor environment. Negligible changes to O *K*-edge XANES spectra occur for annealing temperatures below 600 °C, however, significant enhancement of *Vo*-related features (C_2, D_2 and E_2) is observed when the nanoparticles are annealed in the temperature range 700 °C – 900 °C.

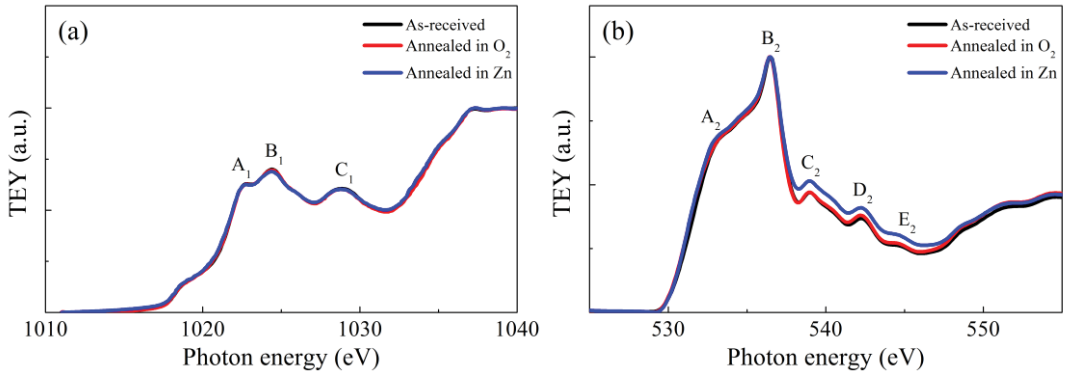

Figure 4.7. Normalized (a) Zn L_3-edge and (b) O *K*-edge XANES spectra of ZnO nanoparticles annealed at 900 °C under O_2 and Zn vapor. The spectra were collected in surface sensitive TEY mode.

4.6 Optical properties of ZnO nanoparticles

4.6.1 Low temperature CL measurement

4.6.1.1 Effect of hydrogen on different green emission

Now the optical properties of the defects in the nanoparticles are reported. Figure 4.8 shows the effects of annealing at 900 °C and hydrogen doping on the CL properties of the ZnO nanoparticles. The DL CL emission of the as-received ZnO nanoparticles at 80 K exhibits a broad visible band centered at 1.82 eV. The LO phonon replicas in NBE are not resolved which could be attributed to peak broadening or crystal quality. Annealing in O_2 atmosphere induces a strong green emission at 2.28 eV (GL1), while Zn vapor annealing produces a green peak centered at 2.48 eV (GL2). The emission intensity of these two GL bands change in an opposite manner in response to a mild H-plasma treatment: decreasing GL1 and increasing GL2, confirming these emissions are of different chemical origin. Quenching GL1 following incorporation of H^+ donors suggests that this emission is related to an acceptor-like defect. The V_{Zn}^{2-} defect is a likely candidate because, as a double acceptor, it will preferentially interact with H^+ donors forming (H - V_{Zn}^{2-} - H) complexes [181]. Assignment of GL1 to V_{Zn}^{2-} is consistent with the absence of a corresponding EPR signal in Figure 4.5(a) as this

defect has no unpaired electrons. Additionally XANES measurements show that the presence of V_{Zn}^{2-} does not strongly affect the atomic configuration of Zn in the ZnO nanoparticles. Zn vapor annealing leads to an increase in the concentration of V_O due to surface chemical reactions, as confirmed by the EPR and XANES results presented above, since the nanoparticles coalesce in a Zn-rich environment [182]. GL2 can therefore logically be assigned to the formation of surface V_O centers. In a control study carried out in inert gas Ar at the same annealing temperatures, the nanoparticles exhibit similar faceted morphologies and coalescence behavior as in Zn vapor anneal, which are described in Figures 4.2 and 4.4, albeit at a slightly slower growth rate. The comparatively larger particle sizes when annealing in Zn vapor environment are due to the efficient diffusion of Zn_i in ZnO at elevated temperatures [170]. Enhancement of GL2 following exposure to H^+ can be explained by hydrogen passivation non-radiative recombination channels. This interpretation is supported by the increase of the intensity of the NBE which doubled after hydrogen doping. Previous work by other authors showed that GL decreases with increasing particle size, due to holes trapped at the ZnO surface [183, 184]. However, no such size dependence was observed in this work, presumably because the particle size range in our study is approximately two orders of magnitude greater than the nanoparticle size in the earlier work (~ 1 nm). Moreover, the fact that the GL2 CL spectral shape remains unaltered with the increase in the size of annealed ZnO nanoparticles confirms that V_O surface defects are not influenced by particle size.

4.6.1.2 Gaussian fitting of visible emission

It is known that the broad optical emission from ZnO is a superposition of multiple DL bands involving native and extrinsic defects. Non-linear least squares curve fitting was applied to extract intensities of individual emissions from the broad overlapped defect band. To overcome uncertainty in curve fitting, reference Li-doped ZnO was used to establish the peak parameters of the common yellow emission in ZnO at 80K, which yields the peak position and FWHM of 1.96 eV and 0.56 eV, respectively [185, 186]. These parameters were constrained during a curve fitting to provide rigorous fitting solutions to the DL band. Figure 4.9 shows two examples of curve fit to the DL CL

spectra of ZnO nanoparticles after thermal annealing in O_2 and Zn vapor environment. Using this constrained fitting approach, the intensities of RL, YL and GL in the nanoparticles are established, which are presented in Figure 4.10 as a function of annealing temperature.

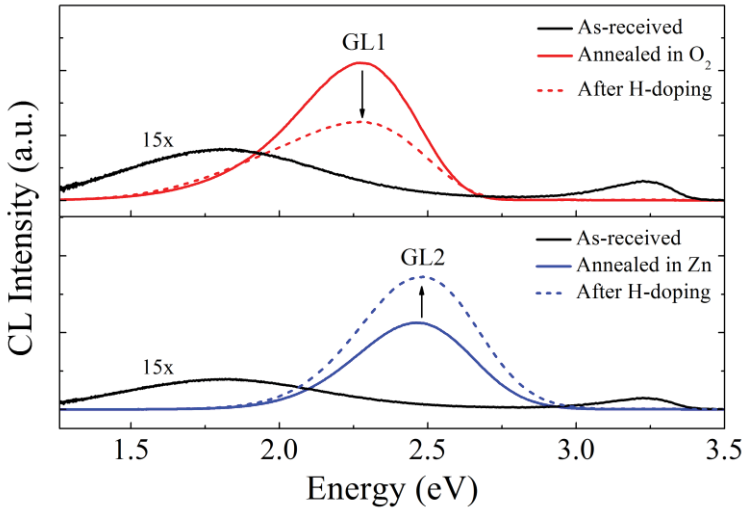

Figure 4.8. CL spectra of O_2 and Zn annealed nanoparticles, recorded at 80 K. The O annealed GL1 at 2.28 eV is quenched by hydrogen plasma treatment, whereas the Zn vapor annealed GL2 at 2.48 eV is increased after the same treatment.

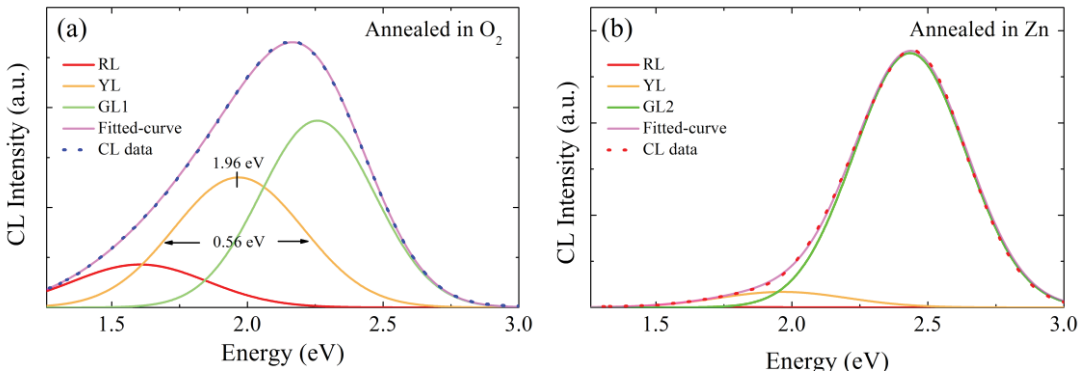

Figure 4.9. CL spectra of the ZnO nanoparticles acquired at 80 K (E_B = 15 keV, I_B = 0.25 nA) with its fitted components. Typical fit of the defect-related band for the nanoparticles annealed at 800 °C in (a) O_2 and (b) Zn vapor atmosphere.

4.6.1.3 Intensity variation of visible emission depending on annealing conditions

As shown in Figures 4.10(a) and 4.10(b), GL1 and GL2 are dominant in O_2 and Zn vapor anneals, respectively. Furthermore, these GL1 and GL2 defects can be engineered by employing two-stage annealing in two different gaseous environments, as illustrated in Figure 4.10(c) and 4.10(d). When annealing at 900 ^oC, the V_{Zn}-related GL1 in O_2-annealed nanoparticles is completely quenched by Zn vapor and the spectrum becomes predominantly GL2, while the V_O-related GL2 of Zn-annealed nanoparticles is gradually reduced and shifted towards GL1. The rapid annihilation of V_{Zn} defects upon annealing in Zn vapor can be attributed to the high mobility of Zn_i at temperatures above 400 ^oC [41]. These results indicate that V_{Zn} and V_O can be eliminated by reductive and oxidative anneal, respectively.

Figure 4.10(a) shows a significant difference in the thermal behavior of Li-related YL, which increases drastically in O_2 anneal while the RL is only slightly affected. The rise in the YL in O_2 anneal is due to an increase in the number of Li_{Zn} acceptors that can be explained by V_{Zn} defects being occupied by mobile Li_i with increasing temperature via the following defect reaction, $Li_i + V_{Zn} \rightarrow Li_{Zn}$. Conversely annealing in Zn vapor produces a strong enhancement of GL2 but only a modest rise in YL and no change in the RL (Figure 4.10(b)). This behavior is different to O_2 anneal due to the growth of the nanoparticles in Zn vapor (oxygen deficient) atmosphere. These results further confirm that GL1 and GL2 have a different chemical origin: GL2 results from recombination channels involving V_O defects while GL1 is related to V_{Zn} centers. The formation of point defects upon annealing at high temperatures (> 500 ^oC) can be described as the following:

$Zn(g) \rightarrow Zn_{Zn} + V_{O,S}$ (reductive anneal in Zn vapor)

$\frac{1}{2}O_2(g) \rightarrow O_O + V_{Zn}$ (oxidative anneal in O_2)

In terms of the stability of the point defects in the ZnO nanoparticles, it is noteworthy that after one year of storage the samples in air the CL spectra of the annealed ZnO nanoparticles are unchanged, indicating that the point defects are stable in air. This result is consistent with the CL data presented in Figure 4.10(a) and 4.10(b), which

show the CL spectra remain unaltered over the annealing temperatures from room temperature to 400 °C.

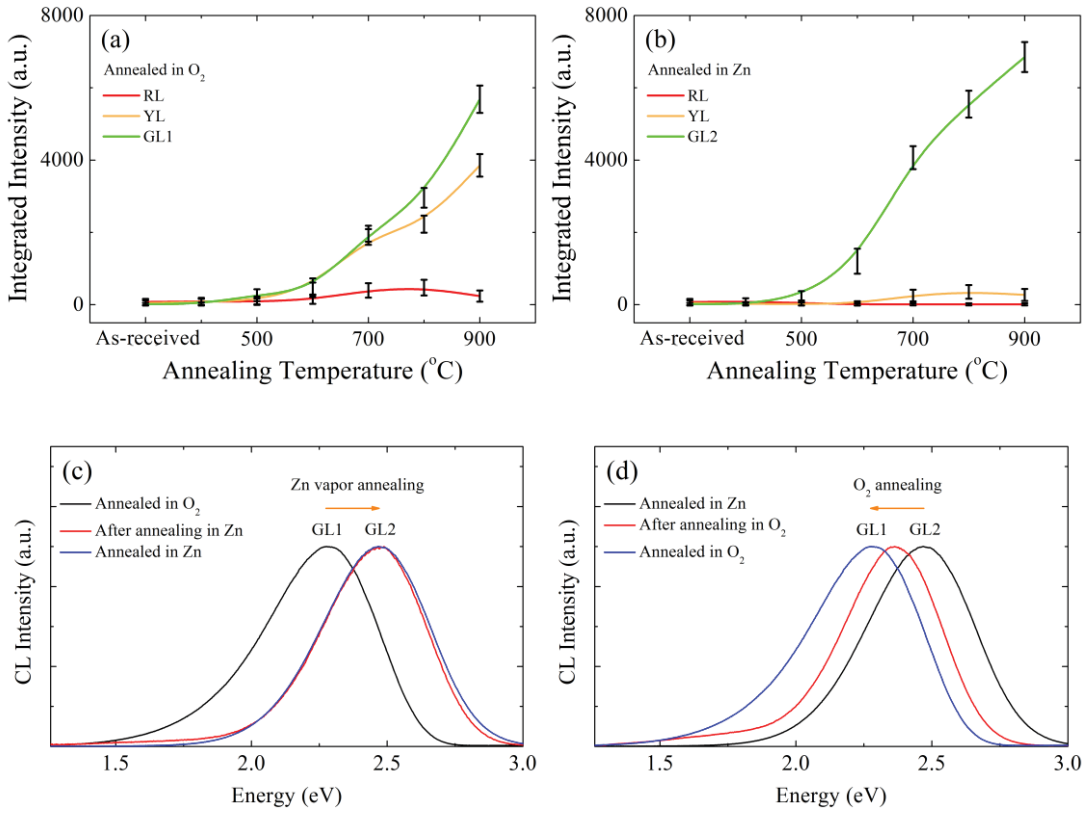

Figure 4.10. Thermal evolution of RL, YT, GL1 and GL2 emissions as a function of annealing temperature in (b) O_2 and (c) Zn vapor atmosphere. GL1 and GL2 arises from thermally generated V_{Zn} and V_O related centers, respectively. (c, d) Normalized CL spectra of the ZnO nanoparticles after a two-stage annealing process in two different environments (O_2 and Zn vapor) at 900 °C, which can be compared with the CL spectra from one-stage annealing. The spectral shift indicates an interchange between GL1 and GL2 after the second annealing stage and that V_O and V_{Zn} defects can be annihilated by oxidative and reductive annealing, respectively.

4.6.1.4 Power density measurement

To gain a better understanding of the DL emission, power density-resolved CL measurements were performed on the annealed ZnO nanoparticles at 80 K. In power density measurements, a penetration depth (the beam energy) is maintained constantly,

while the beam current is varied. By increasing the beam current, a greater number of electron-hole pairs are generated based on the equation:

$$[n]_{eh} \propto I_b \cdot E_b \tag{4.3}$$

where $[n]_{eh}$ is the number of electron-hole pairs generated, I_b is the beam current and E_b is the beam energy.

A series of power density-resolved CL measurements were investigated on both the as-received and annealed ZnO nanoparticles at 80K. In this experiment, the beam energy was kept constant at 15 keV while the beam current was varied from 10 pA to 40 nA. In the power density measurement, ZnO nanoparticles are exposed to high density electron beams. The electron bombardment to ZnO can cause defect formation in the specimen through atomic displacement arising from elastic collisions. Using a minimum displacement energy of Zn and O ions [187], however, the threshold energy of the electron beam necessary for displacement of Zn and O ions is calculated to be ~ 400 keV for Zn ions and ~ 245 keV for O ions, which is much higher than those used in this experiment (E_b = 15 keV). Thus, the electron beam did not damage the samples during the experiment.

NBE and DL behaviors are illustrated in a log-log plot using a simple power-law model. These slopes are able to give information about indications of each emission type and the recombination kinetics. Thus, the logarithmic scale of CL intensity (I_{CL}), versus the logarithmic scale of beam current is plotted and the data are fitted using the following relationship [188, 189]:

$$I_{CL} \propto I^m{}_b \quad \text{or} \quad \log I_{CL} \propto m \cdot \log I_b, \tag{4.4}$$

where m is a linear slope of the logarithmic scale of the fitting curve. Typically the value of the slope (m) is expected to be less than 1 for defect-related emission (slow recombination ~ $\geq 10^{-9}$ s) [190, 191], while band-to-band or excitonic emission (fast recombination ~ 10^{-12} s) have the value of m larger than 1 [192]. However, if the rate of the generation of electron-hole pairs is faster than the recombination rate, saturation effects may occur, showing a non-linear graph at higher beam currents.

Figure 4.11 shows the power-dependence of the emission with the increase of electron beam current. All graphs are plotted as log-log scale to show the power dependency of the emission. Varying beam current in this range only changed the relative NBE and DL and did not introduce any noticeable changes in peak shape or position. Both the NBE and the DL emissions show increasing trend with the electron beam current, but the increasing gradients of the two lines vary.

Both of the data points are the linear fits to the data with the slope m on a log-log scale. The NBE emissions in all specimen exhibit a linear dependence on I_b using a power-law exponent within experimental error for CL measurements, with $m = 1.01 \pm 0.02$, $m = 1.13 \pm 0.01$ and $m = 1.14 \pm 0.02$. The power-law fits reveal that the intensity of the DL for as-received ZnO nanoparticle shows a sub-linear dependence on I_b, with $k = 0.86 \pm 0.02$. While the O-rich DL exhibits an almost linear relationship with $k = 0.92 \pm 0.02$, the Zn-rich DL also exhibits a linear relationship with $k = 0.93 \pm 0.02$. With increasing I_b, the intensity of the Zn-rich DL increases faster than the DL intensity of the as-received sample. For the both of the samples, DL emission shows sub-linear power dependencies with the values of the slopes less than 1, indicating radiative transitions involving DL lattice coupled defects. DL centers are present in a fixed concentration and have typical recombination times of the order of nanoseconds to microseconds as compared to excitonic recombinations which are of the order of picoseconds. NBE exhibits a linear dependence on beam current, indicating that the saturation of the NBE electronic stated in ZnO does not occur. The absence of a peak shift indicates that the DL emission is not a DAP recombination.

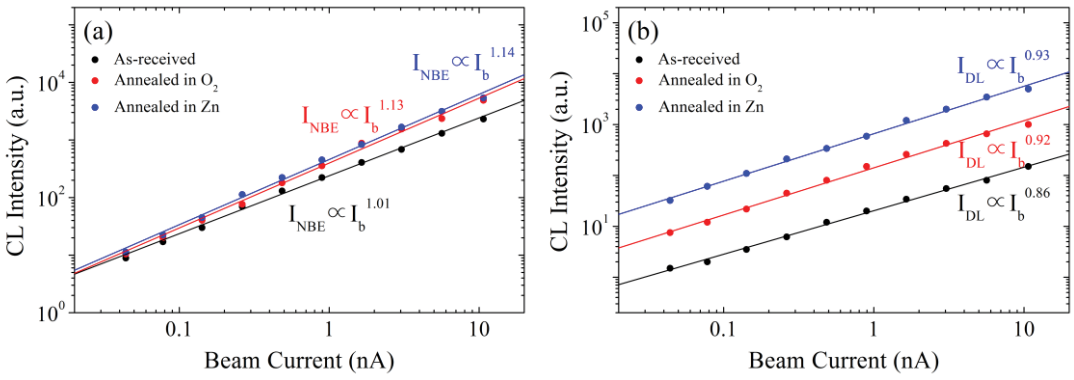

Figure 4.11. Power density CL measurements of the as-received and annealed ZnO nanoparticles at 80 K with various beam currents at an accelerating voltage of 15 kV. The data points show power-law exponent fit.

4.6.2 Sub-bandgap PL measurement at room temperature

Finally, the photophysics of the defect-related luminescence emissions are discussed. Here, PL measurements were performed using sub-bandgap 405 nm and 532 nm laser excitation to directly access the DL defects in the ZnO nanoparticles. Normalized sub-bandgap PL spectra and above bandgap CL spectra at 300 K for the as-received, Zn and O_2 annealed samples are shown in Figure 4.12. When excited using the 405 nm laser PL peaks are observed at 2.33 eV (Zn vapor anneal), 2.23 eV (O_2 anneal) and 1.75 eV (as-received). The last two peaks can be attributed to photo-ionization and radiative relaxation transitions involving ionized Li_{Zn}^{-} and V_{Zn}^{2-} acceptors, respectively [61, 193]. The large Stokes shift with the 1.75 eV has been explained by strong Jahn-Teller (JT) distortion of the V_{Zn}^{-} center [61]. The first peak at 2.33 eV has not been reported in the literature, consequently it is assigned to a radiative transition between photo-excitation of carriers in donor states below the CB with deeply trapped holes at surface V_O. Sub-bandgap excitation with the 532 nm laser at 300 K on the other hand produces a PL peak around 1.90 eV in all three samples, which has been ascribed to O_i [193].

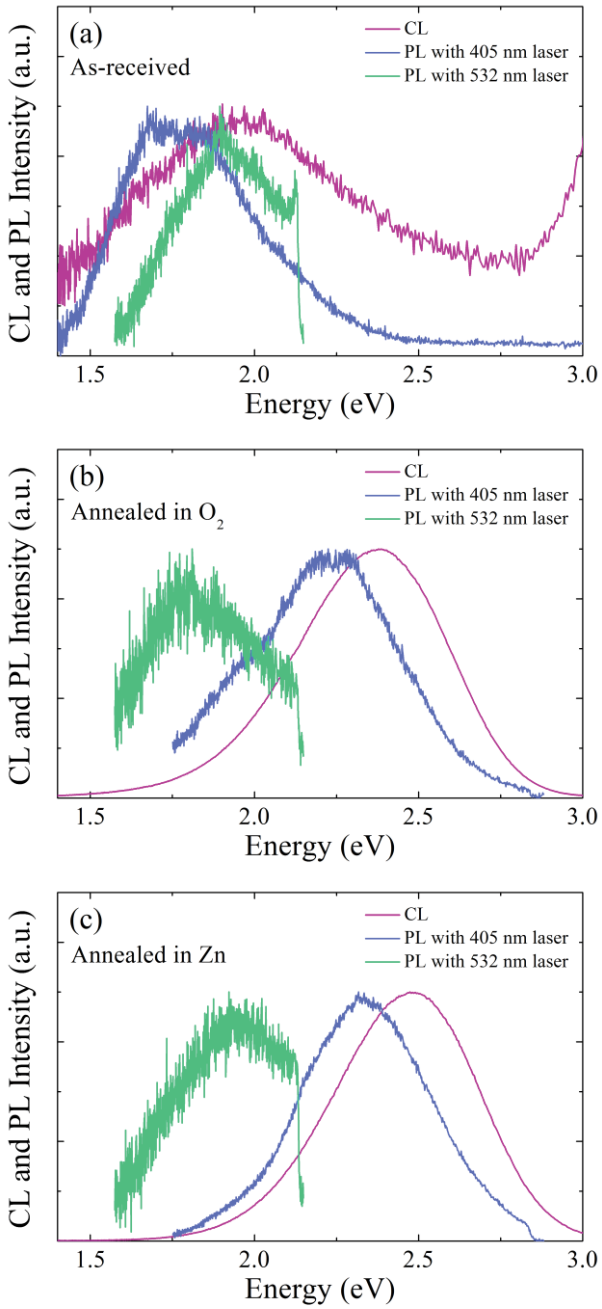

Figure 4.12. Comparison of steady-state 532 nm and 405 nm laser excitation PL and CL spectra at 300 K for (a) as-received as well as (b) and (c) for ZnO nanoparticles annealed at 900 °C in O_2 and Zn vapor, respectively. The sharp feature is due to the presence of an edge filter.

Figure 4.13(a) shows the excited state lifetimes of the fluorescent defects excited by sub-bandgap 405 nm excitation. The as-received nanoparticles and Zn annealed nanoparticles exhibit a similar short lifetime of $\tau_{as} = 10 \pm 0.3$ ns and $\tau_{Zn} = 13 \pm 0.4$ ns for the 1.75 eV and 2.32 eV emission, respectively. The sub-bandgap emission at 2.22 eV formed under O_2 annealing displayed a much longer decay time of $\tau_O > 1$ µs, confirming that the 2.23 eV peak has a different chemical origin to the PL peaks at 2.33 eV and 1.75 eV. The very slow decay time and position of this emission is consistent with reported optical properties for the Li_{Zn} center [194] observed in the CL data Figure 4.10(a). PL decay curves of the ~ 1.90 eV center excited by 514 nm laser light are shown in Figure 4.13(b) exhibiting short lifetimes of $\tau_{as} = 3.55 \pm 0.17$ ns, $\tau_O = 3.60 \pm 0.12$ ns and $\tau_{Zn} = 3.50 \pm 0.16$ ns for the as-received, O_2 and Zn vapor annealed samples, respectively. These sub-bandgap excitation data indicate that the relaxation of the excited states occurs through very fast non radiative channels, which enable the system to be efficiently re-excited. This can occur through fast internal phononic relaxation. A complete understanding of the sub-bandgap excitation and emission PL transitions would require detailed resonant studies of single V_{Zn} and V_O.

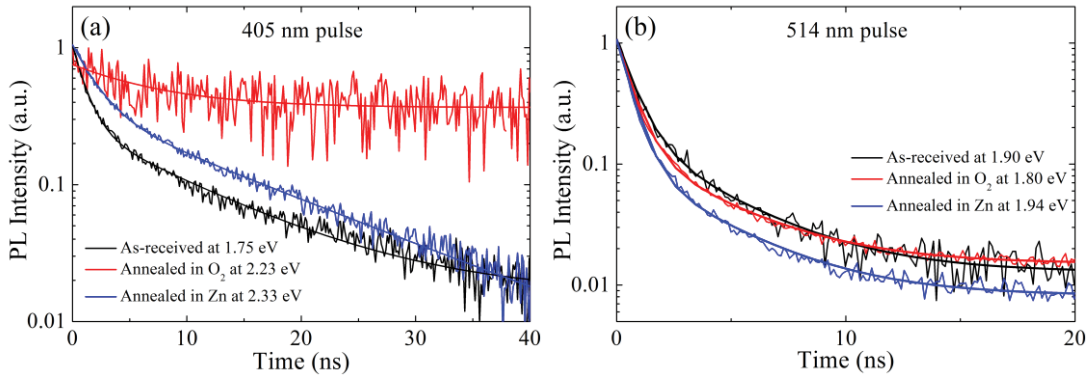

Figure 4.13. PL decay curves at 300 K acquired with (a) 405 nm and (b) 514 laser pulse for corresponding nanoparticles shown in Figure 4.12.

Sample	Emission energy (eV) and lifetime at 300 K			EPR	H-plasma effect on CL
	Above bandgap CL	**Sub-bandgap PL 405 nm**	**Sub-bandgap PL 532 nm**	**g-factor**	
Zn vapor anneal GL2	2.48 Surface V_O^+	2.33 shallow donors - surface V_O^+, τ = 13 ns	1.94 O_i, τ = 3.6 ns	2.00	Quenched
Oxygen anneal GL1	2.38 V_{Zn} center	2.2 Li_{Zn}, τ = > 1 µs	1.80 O_i, τ = 3.6 ns	None	Enhanced
As-received	1.96 O_i	1.75 shallow donors - V_{Zn} related center, τ = 10 ns	1.90 O_i, τ = 3.5 ns	None	Quenched

Table 4.3. Summary of luminescent point defects in ZnO nanoparticles and their photophysical properties.

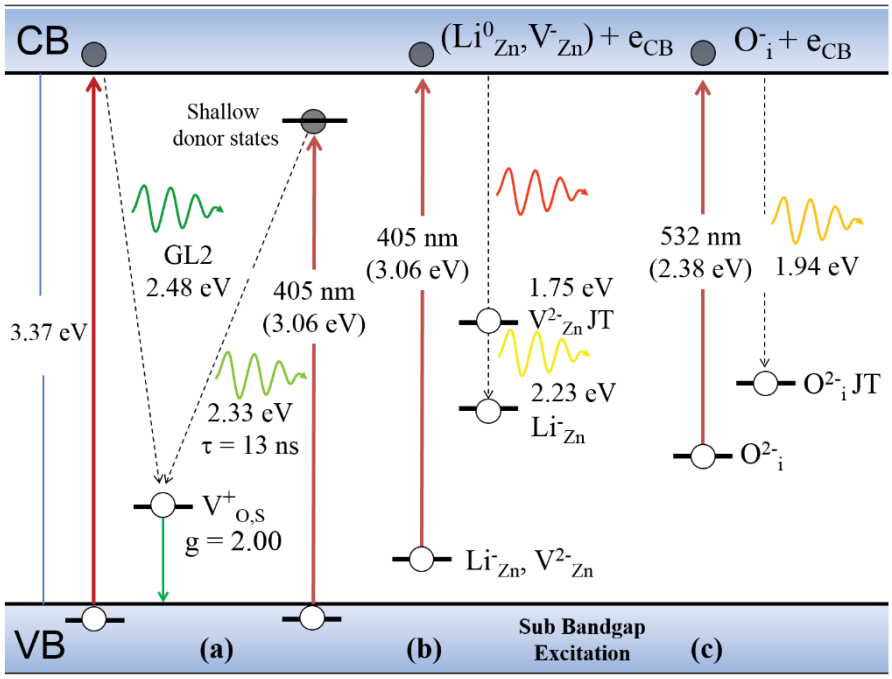

Figure 4.14. Band diagram showing the possible excitation and emission pathways from the discussed defect states. Dashed lines indicate radiative pathways while solid red lines indicate excitation. (a) GL2 emission at 2.48 eV produced with above (CL) and 2.33 eV emission generated with sub-bandgap 405 nm excitation laser, where VB electrons are promoted to the CB and shallow donor states respectively. (b) Promotion of electrons from ionized Li_{Zn}^{-} and V_{Zn}^{2-} acceptors to the CB (photo-ionization) using

sub-bandgap 405 nm light forming Li_{Zn}^{0} and V_{Zn}^{-} and a CB electron (e_{CB}) and the ensuing radiative recombination reinstating the Li_{Zn}^{-} and V_{Zn}^{2-} with PL at 2.23 eV and 1.75 eV, respectively. The later has a large Stokes shift due to a Jahn-Teller (JT) distortion and (c) photo-ionization and radiative relaxation of ionized O_i (O_i^{2-}) using sub-bandgap 532 nm light to produce PL at 1.94 eV.

4.7 Conclusions

In summary, detailed correlative CL, PL, EPR and XANES studies of radiative defects in ZnO nanoparticles have been undertaken. An optical emission peak at 2.28 eV has been attributed to a V_{Zn} related center while an emission at 2.48 eV and corresponding EPR signal at g = 2.00 have been assigned to surface V_O^{+} centers. Their properties at 300 K are summarized in Table 4.3. In addition, the excitation and radiative decay of all of sub-bandgap and above bandgap electronic transitions for each of the defects described above are illustrated in Figure 4.14. The fact that the same defects (i.e. V_{Zn} and V_O) can be accessed using either sub-bandgap excitation or above bandgap excitation, exemplifies that these defects provide very efficient radiative recombination pathways. This is important for future integration of these defects with electrically stimulated devices and photonic resonators [195]. These radiative point defects can be excited using both above bandgap and sub-bandgap excitation which is beneficial for devices and different centers exhibit lifetimes ranging from nanoseconds to microseconds. These exciting luminescence properties of ZnO nanostructures are important to the future development of ZnO materials for nanophotonics, optoelectronics and quantum applications.

Chapter 5

Single photon emission from ZnO nanoparticles

Room temperature single photon emitters are very important resources for photonics and emerging quantum technologies. In this chapter, single photon emission from defect centers in 20nm ZnO nanoparticles is studied.

5.1 Introduction

Sources of non-classical light, are important for a range of applications in quantum communications, sensing and information processing [14, 15]. A particular emphasis is placed on the development of solid-state SPSs that operate at room temperature, as those are the most promising sources for scalable and integrated devices. Color centers in diamond [65], and in particular the nitrogen vacancy [196], and the silicon vacancy defects [197, 198], have been the subject of intense study in recent years due to their unprecedented photostability and spin properties. Recently, several additional materials have emerged as candidates for single photon generation, including site controlled GaN quantum dots [199], defects in SiC [200] and ZnO [11]. While the single photon emission in SiC is attributed to the intrinsic defect known as an "antisite – vacancy pair", the origin of the quantum emission in ZnO remains under debate.

ZnO offers an interesting and valuable system to study quantum effects at the nanoscale [201]. ZnO nanoparticles are commercially available while nanowires and other nanostructures can be easily synthesized by hydrothermal [202] or chemical vapor deposition growth techniques [69, 203]. In addition, ZnO is very suitable for photonic applications, as it has a wide, direct bandgap (3.4 eV) and a large number of

intrinsic defects and impurities that emit from the ultra-violet to the near infrared [7, 44]. Finally, photonic elements including microdisk cavities [87, 202] can be easily fabricated from ZnO. Therefore, there is an urgency to understand and fully characterize the photophysical properties of single emitters to transform ZnO as a valuable platform for quantum photonic applications.

In this chapter, single photon emission from point defects in 20 nm ZnO nanoparticles is studied. The emitters exhibit bright broadband fluorescence in the red spectral range centered at 640 nm. Polarization measurements are performed and the effect of surface termination on the emission properties of these single emitters are investigated.

5.2 Observation and statistical analysis of SPSs from ZnO

5.2.1 Generation of SPSs

ZnO nanoparticles (average size 20 nm, Nanostructured and Amorphous Materials Inc.) were spin coated onto a Si substrate (0.5 cm x 0.5 cm). Then, the substrates were annealed at 500°C in air using a horizontal tube furnace to remove graphitic residue in the powder and to induce the formation of color centers that produced a bright red fluorescence. Single photon emission characteristics were investigated at room temperature under ambient conditions using scanning confocal microscopy. Briefly, a CW pump laser with a wavelength of 532 nm was used as an excitation source, and was focused on the sample through a high (0.9) numerical aperture objective lens (Nikon, x100). The signal was collected using the same objective, directed through a dichroic mirror and a long pass filter (Semrock) and coupled into a multimode fiber (62.5 μm core) that acts as a confocal aperture. The confocal excitation spot in our setup is estimated to be ~ 600 nm. Single photon emission was measured using a standard HBT setup, while the PL spectra were collected using a Princeton Instruments spectrometer with 300 mm focal length.

Figure 5.1(a) shows a representative secondary electron SEM image of the ZnO nanoparticles after annealing in air, where the nanoparticles are clearly visible. Figure

5.1(b) shows a typical confocal map of the ZnO nanoparticles using a 532 nm excitation laser. Several bright spots (marked as circles in Figure 5.1(b)) are visible, and correspond to localized bright fluorescent defects.

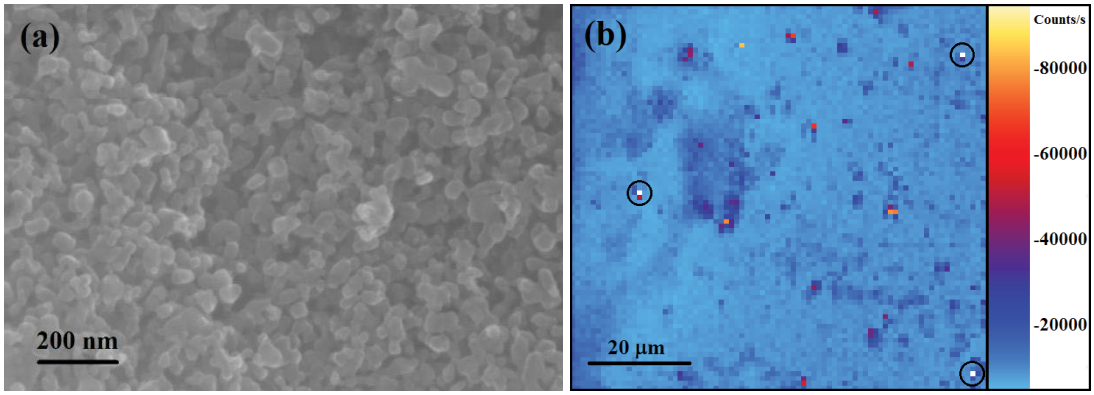

Figure 5.1. (a) SEM image of a dense film of ZnO nanoparticles annealed at 500 °C in air. (b) An 80 × 80 µm^2 scanning confocal image of ZnO nanoparticles excited with a 532 nm laser. Bright isolated emitters are indicated with the circles.

5.2.2 $g^2(\tau)$ analysis

The $g^2(\tau)$ parametrizes the probability of detecting a photon at a delay time, given the probability of detecting a photon at initial time. According to the $g^2(\tau)$, a different classification can be determined. Based on the value of $g^2(0)$, emitted light sources are classified as

coherent light: $g^2(0) = 1$.

bunched light: $g^2(0) > 1$, and

antibunched light: $g^2(0) < 1$.

The coherent light has Poissonian photon statistics, with random time intervals between the photons such as laser source. Coherent light has $g^2(\tau) = 1$ for all values of τ because the probability of obtaining a stop pulse is the same for all values of τ. Bunched light, usually thermal light, is considered as light with $g^2(0) > 1$. It consists of a stream of photons with the photons all clumped together in bunches. This means that if a photon is detected at time $t = 0$, there is a higher probability of detecting

another photon at short times than at long times. Hence $g^2(\tau)$ is expected to be larger for small values of τ than for longer ones. Photon streams of different light sources and those $g^2(\tau)$ plots are described in Figure 5.2.

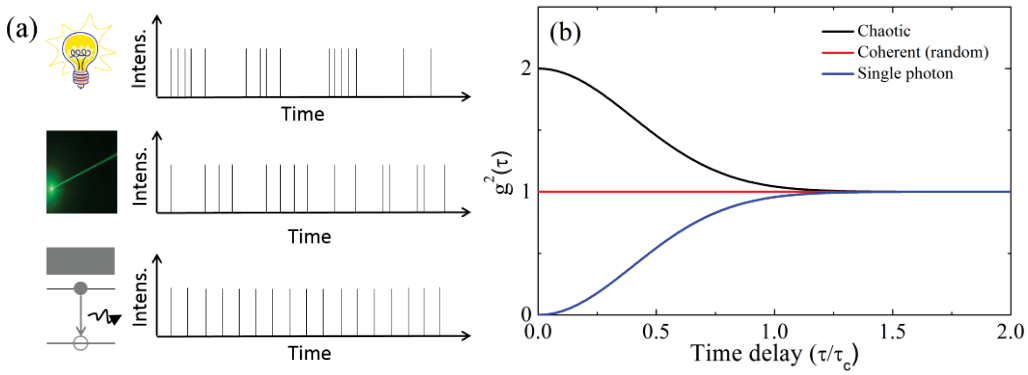

Figure 5.2. Comparison of the photon streams for antibunched light, coherent light, and bunched light. For the case of coherent light, the Poissonian photon statistics correspond to random time intervals between the photons. $g^2(\tau)$ for chaotic, perfectly coherent light, and SPSs plotted on the same time scale.

5.2.3 Two-level system of $g^2(\tau)$

Figure 5.3(a) shows a room temperature PL spectrum recorded from one of the bright spots in the confocal map shown in Figure 5.1(b) (black curve). The curve shows a RL peak at around 640 nm which can be tentatively attributed to V_{Zn} [61]. The background fluorescence exhibited a broad weak RL (red curve). Figure 5.3(b) shows the second order correlation function relevant to Eq. 2.4, $g^2(\tau) = \langle I(t)I(t+\tau)\rangle/\langle I(t)\rangle^2$, that describes the probability of detecting a photon at a delay time, τ, given that a photon was detected at time t, recorded from the same emitter using the HBT configuration. The pronounced antibunching dip in the photon statistics at zero delay time ($g^2(0) \sim 0.1$) indicates that the emission originates from a single photon emitter. The deviation from 0 is attributed to the overall background luminescence. The photon statistics of the single emitters can be described with a frame of a two- or three-level system [11, 64]. The lifetime of the emitters can be deduced from fitting the second order correlation function to the following the Eq. 2.5 at low excitation powers. The lifetime

of the investigated emitter is therefore 6.4 ns – comparable with other single defects in solids [11, 63].

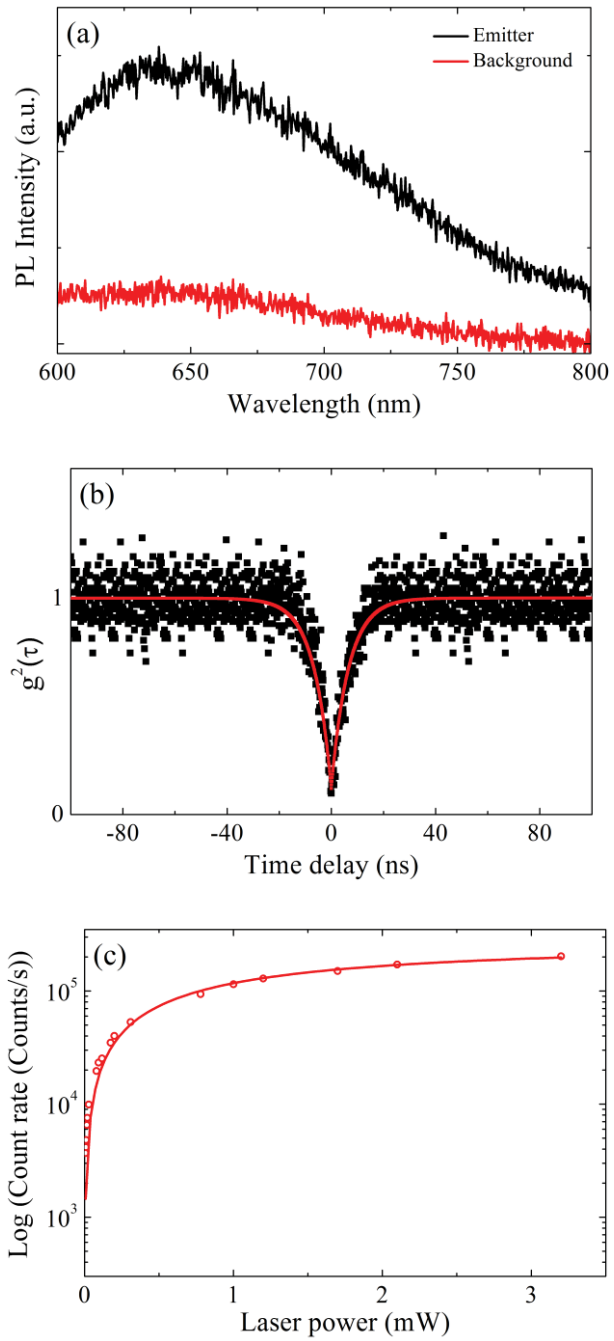

Figure 5.3. (a) PL spectrum recorded from a bright defect within the ZnO nanoparticles (black curve). The red curve represents the background emission. (b) The presence of a single quantum emitter in the ZnO nanoparticles is revealed by the second order

autocorrelation function, $g^2(\tau)$, corresponding to the PL spectrum in Figure 5.3(a). The dip at zero delay time indicates that it is a single emitter. The sold line is a fit using a two-level mode. (c) Single photon emission count rate versus excitation power. The red circles are the raw data and the solid line is the fit using Eq. 5.1. The saturation count rate for this emitter is 1.84×10^5 counts/s.

The saturation curve of a single emitter determined by summing the count rates output by the two APDs of the HBT setup is shown in Figure 5.3(c). The number of emitted photons or the fluorescence count rate of a two-level system can be deduced to quantify the single photon efficiency. This is done by the overall count rate to extract the signal of emitters as a function of laser power, and then fitted to the saturation model for the power-dependent intensity following the equation:

$$\emptyset = \frac{\emptyset_\infty P_{opt}}{P_{sat} + P_{opt}} \tag{5.1}$$

where $\emptyset$ represents the single-photon count rate at a given excitation power (P_{opt}) and $\emptyset_\infty$ is the saturation count rate at optical saturation power (P_{sat}). From this fit, the saturation count rate was determined to be 1.84×10^5 counts/s with an optical saturation power of 1.46 mW. Some emitters were brighter with count rates approaching ~10^6 counts/s. The photon statistics of the ZnO defect and its brightness are comparable with other solid state room temperature SPSs in terms of brightness, which can be advantageous for efficient quantum devices of the emitted light to external cavities, waveguides or heterostructure devices.

5.2.4 Three-level system of $g^2(\tau)$

Some of single emitters show bunching behavior at higher excitation powers, indicating the three-level system with the presence of a metastable (shelving) state. These emitters exhibited very narrow PL lines that corresponded to a very strong bunching, as shown in Figure 5.4(a). This emitter also exhibited blinking. Single emitters with narrow spectral lines are often associated with an extremely fast decay time (~ few ns) and a strong bunching, as also evident by the ZnO defects observed in our work. The $g^2(\tau)$ of the ZnO nanoparticles exhibiting three-level system is shown

in Figure 5.4(b). The calculated radiative and metastable state lifetimes are therefore 2 ns and 25 ns, respectively. In this experiment, only 10 % of the investigated emitters showed strong bunching behavior. Emission from those defects is also associated with a very narrow emission line (~ 5 nm at FWHM). Most of the emitters, however, exhibited moderate or no evidence of a shelving state.

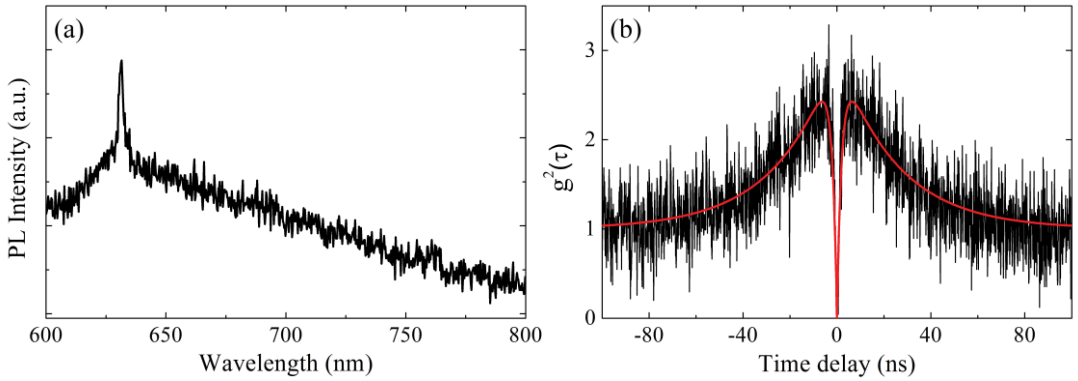

Figure 5.4. (a) Single photon emitter from ZnO that exhibits a narrow PL signal and (b) a strong bunching behavior.

5.2.5 Polarization behavior of SPSs in ZnO

The excitation polarization behavior of the single photon emission was measured by rotating a half-wave plate in the excitation path, and the result is shown in Figure 5.5 (red curve). The emission polarization was characterized by fixing the polarization excitation to a maximum and rotating the polarizer at the collection channel. An almost full extinction of the emission was observed (Figure 5.5 blue curve), indicating that emission occurs from a linearly polarized dipole. The mismatch between the polarization and the emission dipoles originates from the redistribution of the electrons upon photon absorption.

The polarization visibility is defined as

$$V = \frac{I_{max} - I_{min}}{I_{max} + I_{min}} \tag{5.2}$$

where I_{max} and I_{min} are maximum and minimum intensities, respectively. The visibility of the emitter is calculated to be ~ 85 %. High visibility is very important for employing sources for quantum communications as the information is encoded in the polarization state of the emitter. Therefore, highly polarized emitters can provide excellent signal to noise ratios.

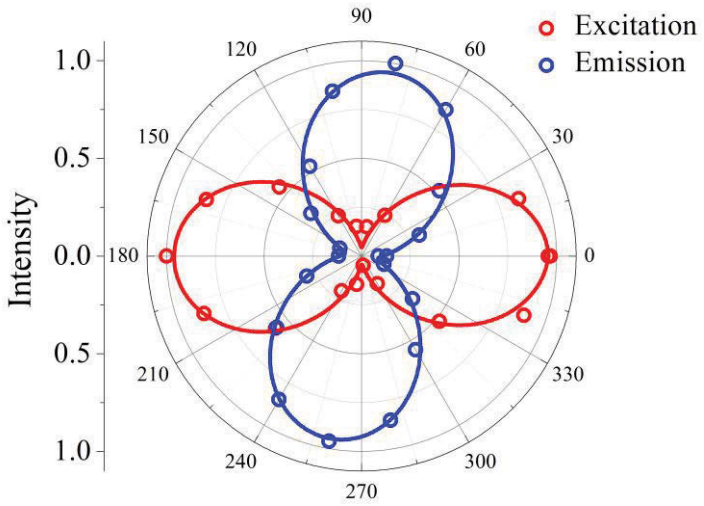

Figure 5.5. Polarization measurement of a ZnO single emitter for both polarized excitation (red curve) and emission (blue curve) as a function of the polarizer angle. The circles are the raw data and the solid line is a fit following Malus' law.

5.3 Surface termination of single emitters on ZnO

All of the investigated emitters in our experiments showed blinking and eventual bleaching after several minutes. To investigate the bleaching behavior, we performed two treatments to modify the ZnO surface. Emission from ZnO point defects is influenced by surface modification such as hydrogen plasma treatment and coating with a polymer barrier layer. In the first experiment, the ZnO nanoparticles were exposed to a hydrogen plasma (2 minutes, 15 W, 473K). The hydrogen plasma treatment is known to lead to quenching of the RL due to the passivation of acceptor–like defects, possibly the V_{Zn} [204]. The reduction in RL is confirmed by CL measurements on the ZnO nanoparticles. Figure 5.6 shows the CL spectra of ZnO

nanoparticles before and after hydrogen doping processing. This clearly shows that the hydrogen termination quenched the RL. The second process involved the deposition of 200 nm of optically transparent PMMA to coat the nanoparticles. This was inspired by recent reports on the quenching suppression of emission in diamond nanoparticles using polymer coatings [205]. After each step, confocal maps were recorded and single emitters were identified. Figure 5.7(a) and 5.7(b) show antibunching curves recorded from single emitters after hydrogen plasma and after PMMA coating, respectively. It is clear that the emitters still maintain their quantum behavior after the hydrogen passivation treatment and PMMA coating.

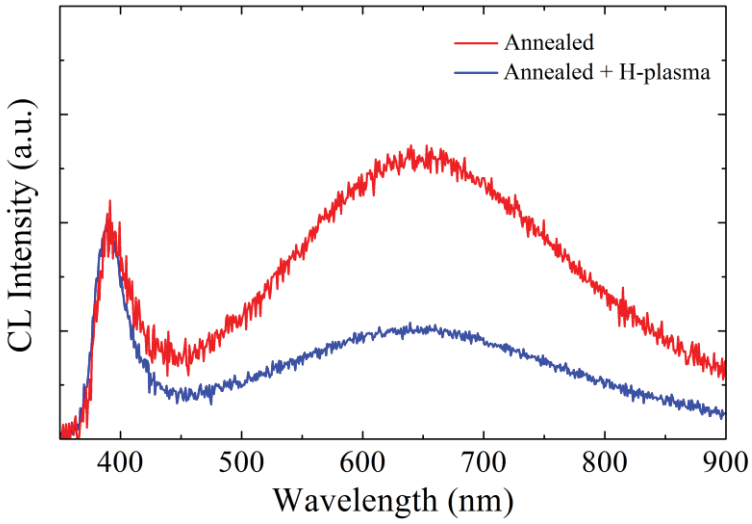

Figure 5.6. CL spectra of ZnO nanoparticles before and after hydrogen plasma treatment. Reduction of RL is observed after the exposure to hydrogen plasma.

5.3.1 Effect of PMMA coating on stability of SPSs in ZnO

Figure 5.7(c) and 5.7(d) show the defect stability recorded from a blinking single emitter from untreated nanoparticles and PMMA coated nanoparticles, respectively. The blinking traces clearly show that the emitters embedded in ZnO nanoparticles that have only been annealed, bleach after several minutes of excitation with a laser beam. Over 20 emitters were measured and all exhibited equivalent behavior. Conversely, the ZnO nanoparticles that are coated with PMMA exhibited blinking, but did not bleach under same excitation conditions. The time constants associated with the on/off

PL intermittency follows an exponential trend, in contrast to that observed for quantum dots, where a power law is followed, but similar to the behavior of other point defects in semiconductors [200, 205, 206]. The mechanism giving rise to this blinking may likewise arise from a photo-induced charge conversion of the defect, to a charge exchange with other impurities in close proximity that act as charge traps or from low probability transitions to a meta-stable dark state. The duration at which the system spends in the "off" state is in the range 70 – 160 ms. Figure 5.8 shows the distribution of the "on" and "off" times of the blinking defect on a semi-logarithmic scale. Both τ_{on} and τ_{off} follow an exponential trend. As expected, the emitters spend considerably longer in their "on" state. For this particular emitter, t_{on} = 1.85 s and t_{off} = 152 ms.

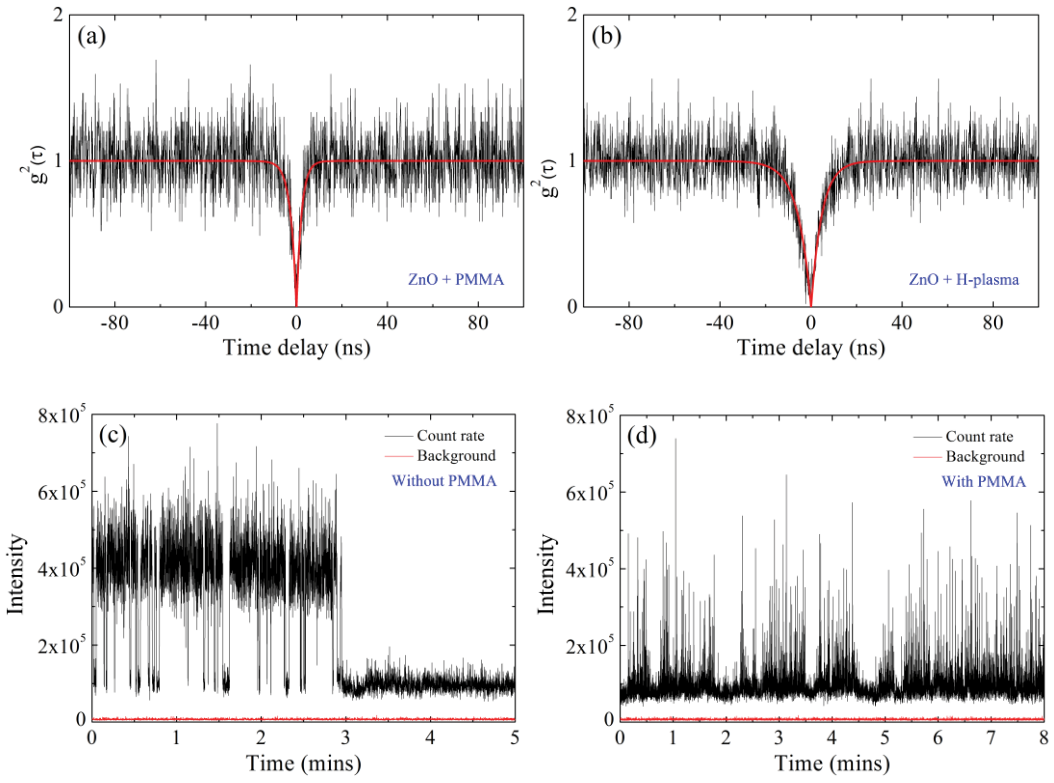

Figure 5.7. $g^2(\tau)$ recorded from single defects within ZnO after (a) coating with PMMA and (b) exposure to hydrogen plasma. (c) Intensity trace recorded from a single emitter within an untreated ZnO nanoparticle showing permanent bleaching after 3 minutes. (d) Intensity trace of a single emitter of a ZnO nanoparticle coated with PMMA exhibits blinking but no bleaching. The red curve in (c, d) is the background fluorescence.

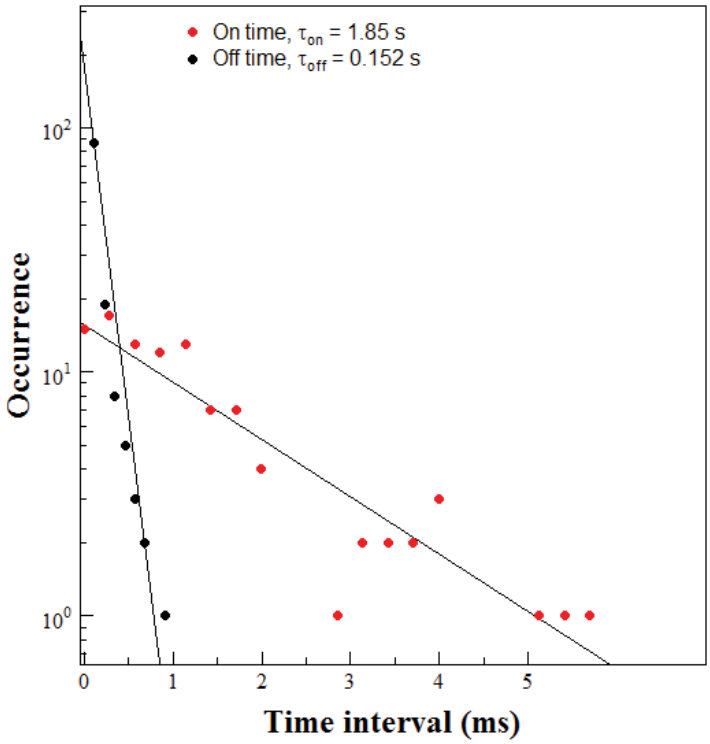

Figure 5.8. The "on" and "off" times of a single ZnO emitter.

5.3.2 Effect of hydrogen on density of SPSs in ZnO

Hydrogen passivation did not yield similar results, and the investigated emitters exhibited similar bleaching as the untreated ZnO nanoparticles. However, after exposure to the hydrogen plasma, the density of emitters increased by a factor of three compared with the untreated samples. The PMMA coating did not influence the absolute number of observed single defects. This indicates the likelihood that the quantum emitters are charged defects, which are influenced by the surface termination and can be switched on and off [207, 208]. Hydrogen termination is likely to induce band bending, thus stabilizing or increasing the probability to populate the single emitter. Hydrogen also rapidly diffuses in ZnO nanoparticles [209], and can create local charge traps and defects that increase the formation of quantum emitters. Furthermore, during the "off" and bleaching states, the emitters are still bright (~ 80,000 counts/s) compared to the background fluorescence from the particles (~ 6000 counts/s – marked as a red base line in Figure 5.7(c) and 5.7(d). However, this emission does not exhibit quantum behavior. This suggests that the quantum emitter is likely to

be a different charge state of the same broad emission that contributes to bright fluorescence or associated to transition metal impurities that do have emission at a similar spectral range [210]. At this point, however, the chemical origin of the quantum emission to a specific defect center has not been assigned yet.

5.4 Conclusions

In summary, single photon emission from point defects in 20 nm ZnO nanoparticles was observed. The quantum emitters can easily be formed through annealing in air – providing an excellent platform for easy access to solid state quantum systems at room temperature. The emitters exhibit red fluorescence centered at 640 nm with a high count rate (~ 200,000 counts/s) and display a fully polarized emission. SPSs in ZnO defects are extremely advantageous in terms of its visibility (~ 85 %). The as-grown and annealed emitters all exhibit blinking which quenched after exposure to the laser beam after several minutes. However, observed ZnO single emitters were stable after the ZnO nanoparticles were coated with PMMA. Emission count rates from ZnO single emitters were collected more than 10 minutes, which is important for future quantum photonic applications. Exposure to a hydrogen plasma treatment increased the yield of the single photon emitters. The long term optical stability of SPSs in ZnO is still under investigation, with some results suggesting blinking, while others found photostable emitters. Different treatment conditions can strongly affect on the formation of color centers in ZnO. For example, plasma treatment or annealing in different atmospheres and temperature can change emission properties, such as Zn-rich or O-rich conditions. In ZnO nanostructures, high temperature annealing (> 700 ^{o}C) creates other defects that showed strong green emission, rather than red emission showing SPSs. Further studies to optimize the formation probability of these quantum emitters are required. Finally, generation of these quantum emitters in bulk material is important to broaden their applicability to various quantum applications.

Chapter 6

Electroluminescence from localized defects in ZnO – toward electrically driven single photon sources at room temperature

SPSs are required for a wide range of applications in quantum information science, quantum cryptography and quantum communications. In the previous chapter, single photon emission from ZnO nanoparticles was observed under the optical excitation. In this chapter, ZnO/Si heterostructures are fabricated and these EL are studied for potential quantum photonic applications.

6.1 Introduction

As discussed in the previous chapter, SPSs have been observed from ZnO nanoparticles. SPSs are widely used in quantum applications such as quantum cryptography and information science. Although SPSs based on quantum dots are robust and have ideal optical properties, such as narrow emission linewidth and short excited state lifetimes, their operation is mostly limited to cryogenic temperatures [211-213]. Alternatively, color centers in wide bandgap materials are excellent candidates for room temperature SPSs. These color centers have energy levels within the bandgap of the host matrix, and form localized confined states that can emit single photons on demand. Diamond, for example, has been studied extensively, due to its ability to host plethora of emitters that are photostable and exhibit single photon emission at room temperature [214].

The need to integrate the SPSs with scalable photonic devices, such as resonators or optical cavities, enhances the urgency of generating electrically driven SPSs [215-218].

It has been shown previously that electrically driven light emission can be realized with heterojunction nanostructures, where carrier injection occurs across the p-n junction or in the i region of a p-i-n junction [219-221]. However, engineering efficient junctions from materials like diamond is challenging, and requires sophisticated growth conditions and cumbersome implantation of the single emitting defects [222].

A more promising approach for fabrication of quantum LEDs is exploiting other semiconductors that are more suitable for current optoelectronic applications. One of these materials is ZnO, which has recently been shown to host single defects that are harnessed as SPSs [11, 12]. In addition, ZnO has attracted significant attention for its extensive photonic applications in UV and visible spectral range due to its relatively large bandgap and high exciton binding energy. The mature technology of ZnO heterojunctions with Si or GaN has enabled fabrication of advanced optoelectronic devices including transistors and LEDs [30, 31, 223, 224]. Therefore, the transformation of these technologies into the quantum device regime, where single emitters can be electrically addressed in ZnO heterojunctions is a promising avenue for scalable quantum photonic applications.

In this chapter efficient electrically driven light emission from localized defects in n-ZnO/p-Si heterojunctions is reported. Two different sources of n-ZnO are investigated. The first source is based on sputtered ZnO films and the second involves deposition of ZnO nanoparticles. n-ZnO/p-Si heterojunction devices have been chosen due to their cost effective and mature fabrication techniques.

6.2 Device fabrication and electrical characteristics

A schematic diagram of the devices is shown Figure 6.1(a). First, ~2 mm diameter circular electrodes were patterned by standard lithographic process. Then, 300 nm SiO_2 layer was deposited on a p-Si substrate (Boron-doped, 0.001-0.005 ohm·cm) via e-beam evaporation, followed by 150 nm Al sputtered as the electrodes on the SiO_2 layer to achieve a Schottky barrier. The thin layer of SiO_2 is used as a spacer between

the two electrodes. The photoresist was lifted-off by ultrasonication in acetone solution for 5 minutes to fabricate the proper structure of $Si/SiO_2/Al$.

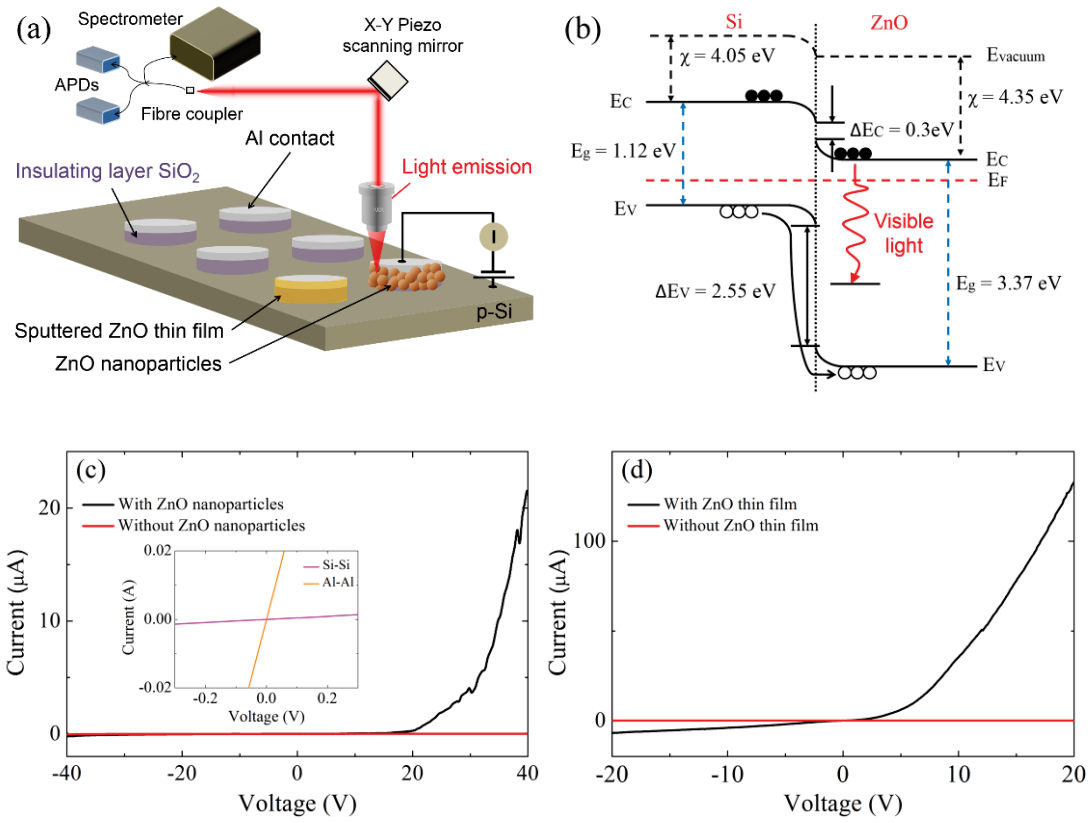

Figure 6.1. (a) Schematic diagram of the n-ZnO/p-Si heterojuction. Electrically driven light emission is generated at the edge of the circle, and then collected through a microscope objective and directed into APDs or a spectrometer. (b) The energy band diagram of the n-ZnO/p-Si heterojunction under zero voltage bias. Defect-related radiative recombination occurs in the devices. The electrons in the CB of ZnO will drop down into the defect-related energy level of ZnO to recombine with the holes therein, giving rise to the visible emission. (c, d) I-V characteristic of the n-ZnO/p-Si heterostructure devices; (c) ZnO nanoparticles/Si configuration with a threshold voltage of ~ 18 V and a measured current of 20 μA at 40 V of forward bias. Inset is the I-V characteristic of Al-Al and Si-Si contacts showing good Ohmic characteristics. (d) ZnO thin film/Si configuration, with a threshold voltage of ~ 7 V and a measured current of 200 μA at 20 V for the ZnO thin film-based device.

To fabricate the heterojunction with the nanoparticles, ZnO nanoparticles (20 nm, Nanostructured and Amorphous Materials Inc., USA) were first annealed at 500 °C for 30 minutes, dispersed them in methanol solution and then drop cast on to the pre-patterned Si/SiO_2/Al substrate to stick on the wall of the mesa to obtain p-Si/n-ZnO heterojunction. To engineer the devices with sputtered ZnO, 50 nm ZnO thin films were grown on the wall of the mesas using a 0.25A DC current controlled deposition from a 2" ZnO (99.99%) sputter target with an argon pressure of 2 mTorr. Prior to the deposition, the sputter chamber was evacuated to a base pressure of ~ 5×10^{-7} torr. The film thickness was monitored using a quartz crystal monitor in the chamber. To obtain reliable Ohmic contacts and to create the color centers within the sputtered ZnO, the sample was annealed at 500 °C for 30 minutes in air environment. On the basis of the positioning of the junction on the side of the mesa structure, the common problem of absorption within each of the electrodes is avoided entirely. The light is generated in the ZnO on the side walls of the mesas and is directly observable from above without having to be transmitted through either electrode. During deposition, the ZnO covers all areas of the devices and the SiO_2 insulating layer is utilized to separate the Al electrode from the Si. The only conductive path between the electrodes is through the ZnO coated on the walls of the mesa structure. When contacting the electrodes the probes penetrate thorough the ZnO to directly contact the Al.

To understand the mechanism of light generation from the formed devices that were fabricated, an energy band alignment diagram n-ZnO/p-Si heterojunction is considered in Figure 6.1(b) based on individual band structures. The dominant mechanism of EL is the recombination of holes injected from the Si with electrons in the ZnO that were supplied additionally by the contact with Al. With the increased forward bias, the energy barriers for electrons and holes are both lowered, thus favoring the injection of electrons and holes. The electron affinities of Si (χ_{Si}) and ZnO (χ_{ZnO}) are 4.05 eV and 4.35 eV, respectively, and the bandgap energies are 1.12 eV and 3.37 eV, for Si and ZnO, respectively. Therefore, the CB offset for electrons is $\Delta E_C = \chi_{ZnO} - \chi_{Si} = 0.3$ eV, whereas that for holes is $\Delta E_V = 2.55$ eV [225]. Although holes injected from the p-Si are limited due to the large barrier, the very high concentration of holes in p-Si causes

a certain amount of holes to be injected into ZnO under the appropriately high forward bias. The electrons from the CB of the ZnO may first occupy these empty defect-produced traps and subsequently, directly recombine with DL defects in the bandgap to produce the visible emissions. The details of the mechanism are discussed in later with EL and PL spectra from the devices.

To study the diode characteristics, I-V measurements were carried out for the two different devices, which are shown in Figure 6.1(c) and 6.1(d). Tungsten probes with 1 μm tips attached to micropositioners were used to connect to the sample electrodes. The inset of Figure 6.1(c) shows a linear behavior of I-V characteristic between two Si-Si and Al–Al electrodes, indicating that a good Ohmic contact was achieved. The red curves represent the measurement without the ZnO materials to confirm that there is no metal leakage of Al on the Si through the insulating layer of SiO_2. The black curves in Figure 6.1(c) and 6.1(d) are the I-V measurements after the deposition of ZnO nanoparticles (film) on the samples. Both junctions exhibit excellent, well-defined rectifying behavior. The ZnO nanoparticle device shows a threshold voltage at ~18 V and a forward current more than 20 μA at 40V, whereas the ZnO thin film device exhibits higher current, ~200 μA at 20 V with lower threshold voltage of ~7 V. The different onset voltages between two devices and noise of the curves in Figure 6.1(c) may arise from the presence of surface states, from the presence of an oxide layer at the interface because the SiO_2 layer acts as a barrier in series [226], or from unavoidable voids in the nanoparticle sample.

6.3 Electroluminescence (EL) from the n-ZnO/p-Si heterostructures

To investigate the luminescent properties of the formed devices, EL and PL measurements were collected using a confocal microscope with 500 nm lateral resolution. The signal was collected through an objective with a numerical aperture of 0.7 and directed into a spectrometer (Princeton Instruments, 300 lines/nm grating). For the PL excitation, a CW laser of 532 nm was employed. A dichroic mirror was used to

filter the excitation laser. All signals were recorded using an avalanche photodiode (Excelitas, SPCM-AQRH-14) and analyzed using a single photon counting (PicoHarp 300). The measurements were carried out at room temperature under ambient conditions. Upon applying the voltage between the Al contacts and the Si wafer, the emission was generated at the edge of the circular mesas. Throughout the measurements, the contact probes were positioned close to the scanning area to achieve higher EL generation and therefore better a signal-to-noise ratio.

6.3.1 Confocal map of the devices

Panels (a) and (b) in Figure 6.2 show room temperature EL confocal maps recorded from the ZnO nanoparticles and the sputtered ZnO heterojunctions, respectively. The bright spots in the confocal image correspond to localized electrically excited luminescence defects. For the ZnO nanoparticles-based device, the EL signal becomes detectable when a forward direct current bias of 35 V is applied across the device. No EL is detected under reverse biasing. However, further increasing the applied voltage over 40 V resulted in electrical breakdown of the devices.

6.3.2 EL and PL of the devices

Panels (c) and (d) in Figure 6.2 show the corresponding EL spectra from the nanoparticles and the sputtered films (blue curves), respectively. Both devices exhibit broad peaks at the red spectral range (at 660 nm and 620 nm) – that is typical to the sub-bandgap defect emission described in chapter 4 and 5. The fact that the EL signal was obtained from a localized spot indicates that recombination occurs on an individual defect site – ideal for generation of non-classical light.

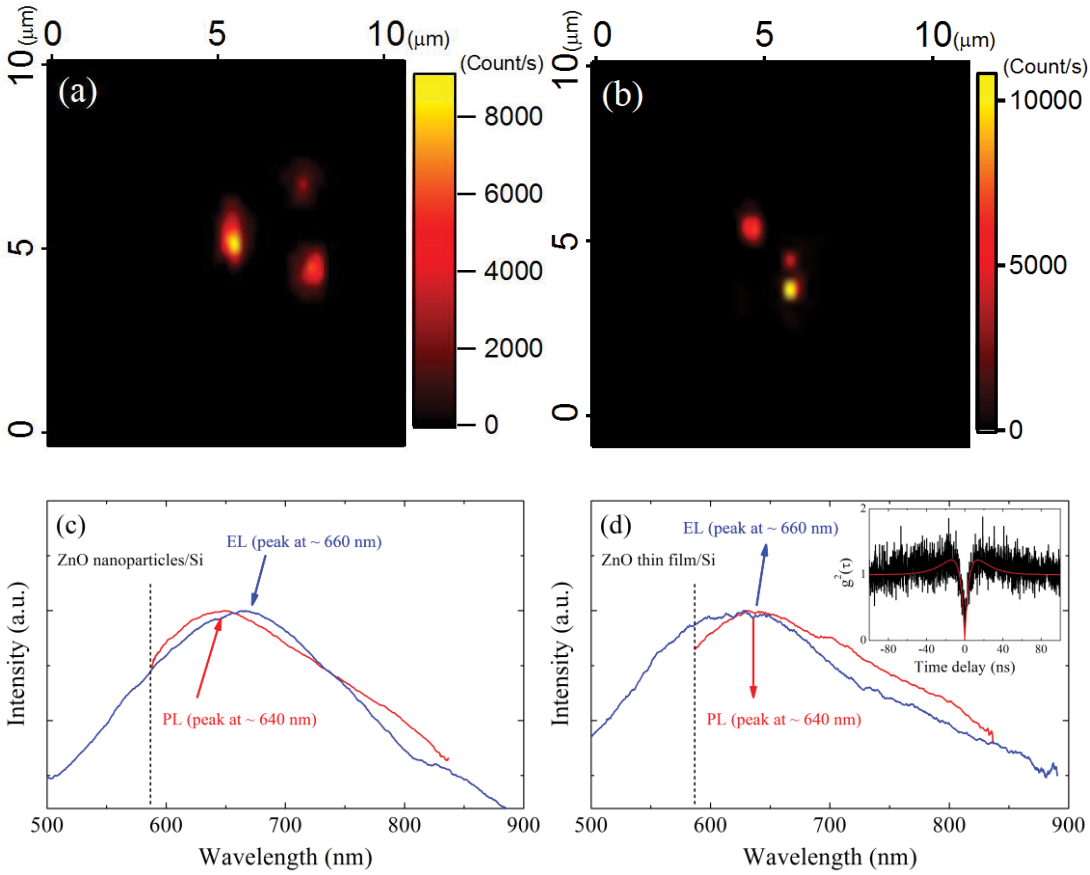

Figure 6.2. EL and PL results of defects in ZnO/Si devices recorded at room temperature. (a) EL confocal maps recorded from the ZnO nanoparticles/Si and (b) ZnO thin film devices, respectively. The bright spots correspond to defect-related color centers in ZnO. (c, d) EL and PL spectra of the devices recorded at room temperature; (c) ZnO nanoparticles/Si, and (d) ZnO thin filn/Si devices. Both devices exhibit orange-red emission ranging from ~ 500 nm to 800 nm when 40 V and 15 V were applied to ZnO nanoparticles/Si and ZnO thin film/Si, respectively. While PL spectra show no difference from both samples, positions of peak wavelength of EL are slightly different, possibly resulting from different defect centers in ZnO. Inset of (d) is the $g^2(\tau)$ of ZnO thin film excited by PL, indicating the presence of a single quantum emitter in the ZnO thin film. The bunching ($g^2(\tau) > 1$) indicates the presence of a metastable state.

Complementary PL spectra from same spots were collected using a 532 nm excitation, with no bias applied to the sample, to access the DL defects in the ZnO. The spectra

are shown in Figure 6.2(c) and 6.2(d) as red curves. Slight spectral shift between the EL and the PL signals can be observed, likely due to different excitation pathways. However, their full width half maximum spectra are similar, indicating that similar defects are addressed. This attribute is unique to ZnO and is highly advantageous because often EL and PL result in excitation of completely different emission spectra, such as in the case of diamond [222], where optical excitation results in emission of negatively charged nitrogen vacancy but electrical excitation triggers the neutrally charged nitrogen vacancy center. Whereas PL depends only on the material's optical properties, EL, which is excited by current injection, is determined by the entire device structure, including the optical and electrical properties of its light emitting layers, electrodes and contacts. The difference between the PL and EL spectra is merely due to the difference in the luminescence excitation mechanisms not different defects. The EL and PL signals can be potentially ascribed to O_i centers or V_{Zn}^- defects [61, 193]. All the studied defects emitted at the same spectral range and had similar linewidth, and they can be generated by controlled atmosphere heat treatment, as shown in our results.

To verify that the ZnO thin film exhibits single photon emission, HBT interferometer was used on the same position of the confocal map in Figure 6.2(b) under a 532 nm laser excitation. Inset of Figure 6.2(d) shows the second order correlation function $g^2(\tau)$ from the ZnO defect center. An antibunching dip at zero delay time ($g^2(\tau) = 0.2$) indicates that the emission originates from a single photon emitter. Because the emitter was measured at high excitation power (~ 2 mW), bunching behavior was also observed, indicative of a three-level system with a shelving, metastable state. The red line is the theoretical fit using a three-level system Eq. 2.6. The fit indicates that the values of the lifetime are $\tau_1 \sim 5$ ns and $\tau_2 \sim 34$ ns.

6.4 Brightness and stability of the devices

Now, the emission saturation from the electrically driven devices is studied. Figure 6.3(a) and 6.3(b) shows the measured count rate as a function of injection current for

the ZnO nanoparticles/Si and the ZnO thin film/Si, respectively. The black dots are experimental values, while the red curves are the fit according to the following equation:

$$C = \frac{C_{Sat}\, I}{I_{Sat} + I} \tag{6.1}$$

where C is the emission count rate at a given injection current (I) and C_{Sat} represents saturation count rates at saturation current (I_{Sat}). From the fitting equation, the saturation count rates are determined to be 7.23 $\times 10^3$ counts/s and 2.07 $\times 10^4$ counts/s with saturation current of 32.4 μA and 6.4 μA for the ZnO nanoparticles/Si and ZnO thin film/Si, respectively. These values are comparable with other electrically driven sources [215, 216].

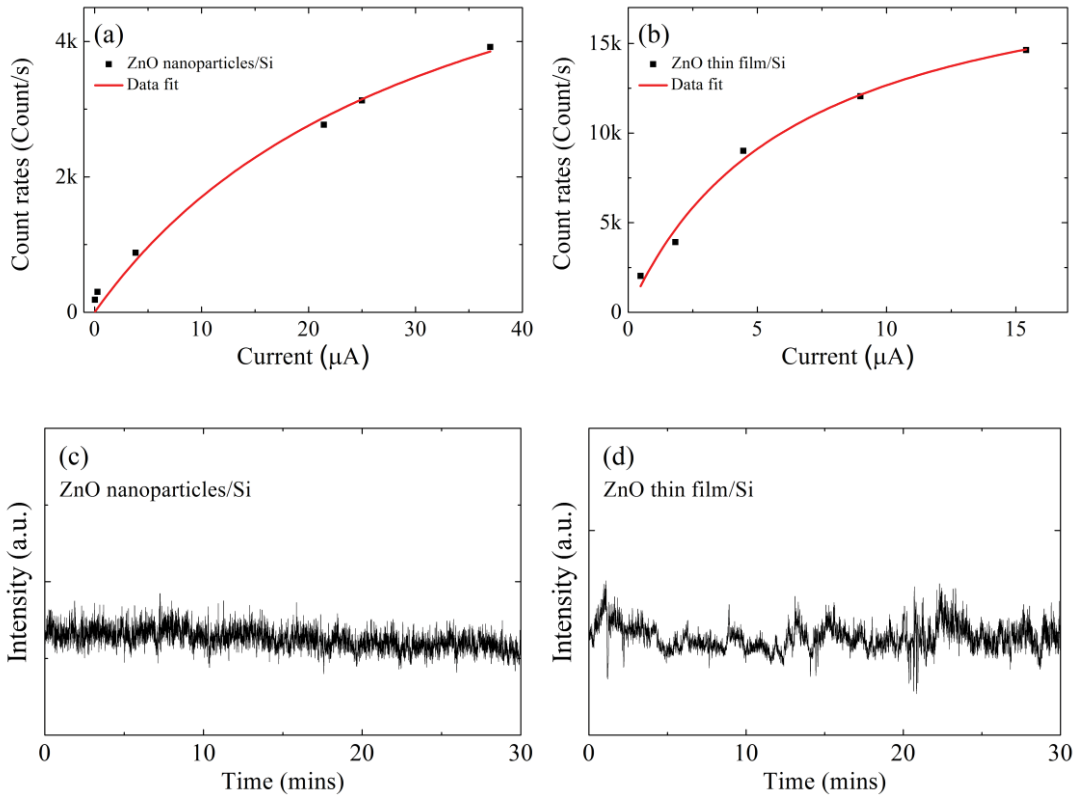

Figure 6.3. (a) Count rate of the EL generated emission as a function of the device current for the ZnO nanoparticles/Si and (b) ZnO thin film/Si devices. The black dots are raw data and red curves are the fitting curve showing saturation behaviors according to the Eq. 6.1 with C_{Sat} = 7.23 × 10^3 counts/s and I_{Sat} = 32.4 μA for ZnO

nanoparticles/Si and C_{Sat} = 2.07 × 10^4 counts/s and I_{Sat} = 6.4 μA for ZnO thin film/Si, respectively. (c) and (d) are the intensity traces recorded from one of the bright spots in the confocal map from the ZnO nanoparticles/Si and the ZnO thin film/Si devices, respectively. Both devices exhibited excellent photostability for more than 30 minutes.

To test the photostability of the studied defects, luminescence intensity traces were measured as a function of applied current. Panels (c) and (d) in Figure 6.3 shows the stability measurements of the EL generated from the ZnO nanoparticles and the ZnO film devices, respectively. These figures show that the emission was persistently stable for more than 30 minutes, indicating that the ZnO/Si devices could be a potential light source for future solid-state quantum photonic applications operating at room temperature. The low count rate is most likely due to low quantum efficiency of the defect responsible for the single photon emission. Compared to even diamond that has only emerged in the last decade, the ZnO system is new in the realm of the quantum world, and many important questions such as the quantum efficiency – are still unknown. Thus, this work will expedite these studies and will highlight this intriguing system to the community.

The fabricated device from the sputtered films and the nanoparticles exhibit slightly different device performances, mainly due to their basic structural dissimilarities: Figure 6.4 shows SEM images of the (a) sputtered ZnO and the (b) ZnO nanoparticles. The nanoparticles have a much higher crystal quality, lower concentration of bulk point defects and impurities due to their short diffusion length during growth and strong surface effect due to their significantly larger surface-to-volume ratio compared to the films. Typically, V_O or Zn_i dominate the emission spectra of the films. A reduction in the number of defects due to the stoichiometric mismatch can be achieved via annealing in an oxygen atmosphere, which concurrently increases the crystallinity of the films, as was done in our work.

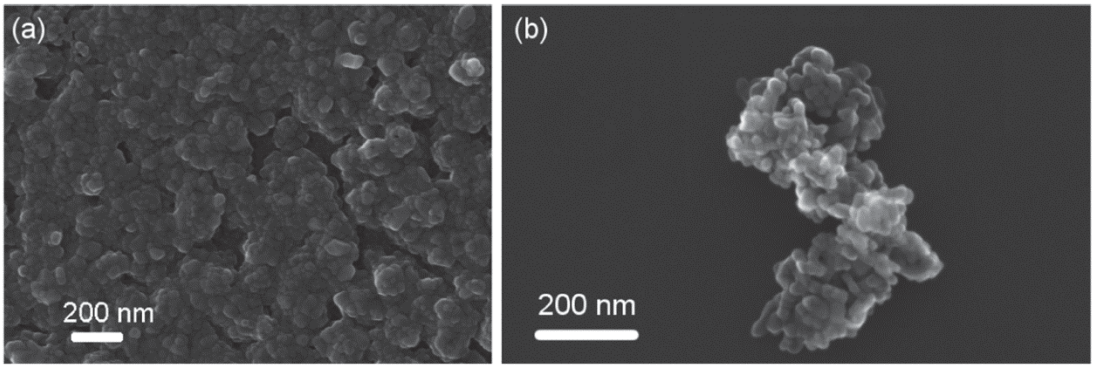

Figure 6.4. (a) SEM image of the sputtered ZnO thin film and (b) ZnO nanoparticles.

There should not be any fundamental issue with generating single photon emission from EL in the ZnO system. These results are pioneering the field, and clearly there is still much scope for improvement. However, EL from localized defects in ZnO has not been achieved to date, and are reported in this work for the first time. Comparing this present work to other known systems, such as GaAs or diamond, it took many decades to record first antibunching measurement from a single defect.

Finally, the potential integration of these electrically driven sources with proper photonic structures is discussed. For instance, to achieve electrically driven ZnO microdisks, one can employ bottom up growth of ZnO on Si through a well-defined lithographic mask. Similar works have been realized recently with gallium nitride microdisk lasers that were grown on Si [227]. Separately, it was shown that ZnO microdisks can be effectively grown bottom up on a substrate of choice [202]. We therefore believe it is viable to grow high quality n-type photonic resonators from ZnO on a p-type Si substrate to achieve electrically driven devices.

6.5 Conclusions

In summary, electrically driven emission from localized ZnO defects integrated within a ZnO/Si heterojunction are reported. The devices were fabricated either from ZnO nanoparticles or from sputtered ZnO. Room temperature I-V characteristics of the diodes confirmed excellent rectifying behavior with the threshold voltages at ~ 18 V

and ~7 V for ZnO nanoparticles and thin film devices, respectively. Defect-related EL at the red spectral range has been achieved under forward bias and it is shown that both devices were stable over 30 minutes, which is crucial for the development of future ZnO based quantum devices. Although the origin of the defects is unknown, they can be reliably and reproducibly engineered in both sputtered films and nanoparticles. Further studies are required to understand the origin of the emission. In combination with the recent progress into ZnO cavities and resonators [104, 202]. These results will be important to realization of cost efficient fabrication of electrically driven, quantum nanophotonic devices employing ZnO as the fundamental building block.

Chapter 7

Observation of whispering gallery modes from hexagonal ZnO microdisks using cathodoluminescence spectroscopy

In the previous chapters, several promising SPSs in ZnO were highlighted and electrical excitation from defects in ZnO has been discussed. The last step is coupling those emitters to optical cavities. Fabrication of n-type ZnO optical resonator on p-type substrate can realize practical nanophotonic devices for quantum photonic technologies. Therefore, in this chapter, ZnO hexagonal microdisks with diameters ranging from 3 μm up to 15 μm were fabricated by the carbothermal reduction method. Apart from other ZnO optical resonators, this ZnO microdisk can be readily engineered when a proper substrate is used.

7.1 Development of ZnO optical resonators for nanophotonics

The development of photonics is now being enabled by semiconductor device technologies such as lasers and detectors. Especially, laser research has met a variety of different laser performance goals and this improvement has revolutionized a wide range of research fields. The interaction between light and semiconductors in a simple manner has made nanophotonics an interesting topic in semiconductor physics.

Among a lot of semiconductors with different structures, wide bandgap semiconductor optical resonators are of great importance in developing paradigms for optoelectronics and LEDs. ZnO is a promising wide bandgap semiconductor for the development of

optical devices in the visible spectral range because of its highly efficient optical emission. ZnO is presently used in a variety of optoelectronic applications, such as LEDs, sensors, piezoelectrics, and transparent semiconductors [6, 203, 228, 229]. In addition, the flexible control over ZnO growth enables bottom up engineering of ZnO micro- and nano-structures with various geometrical shapes and sizes (e.g. tetrapods, tapered nanowires, mushrooms) [68-70]. In particular, there is currently great interest in the bottom up fabrication of ZnO optical resonators that can confine and guide light for applications in photonics and quantum information processing. Thus, the outstanding optical and geometrical characteristics of ZnO make it a promising photonic candidate for optoelectronic devices.

To date, various types of resonators with hexagonal shape have been fabricated and drawn significant attention for optical resonator cavities because of their distinctive geometry and outstanding lasing characteristics. For example, the micro- and nanostructure resonator reveals a FPMs type of resonance, in which the top and bottom planes or the two side facets of the resonators serve as two reflecting mirrors so that the light travels back and forth between two parallel interfaces [118, 230]. Some authors also suggested the cavities formed by ZnO nanostructures showing a FPMs type of resonance [231, 232]. However, this FPMs type of resonators may not provide strong confinement due to the limited reflection at the top and bottom or two opposite side facets. Hence, the performance of lasers based on FPMs may suffer from the low reflectivity of the interface resonator/air.

Conversely, the WGMs, which has been developed in many applications to optics fields, has attracted much interest because it is a very efficient means of luminescence improvement for micro- and nanostructure resonators [233, 234]. As the efficiency of light confinement is subject to the geometrical properties of ZnO, light enhancement based on WGM is much better that FPMs since the light wave propagates circularly around the interface of ZnO/air due to multiple total internal reflections [90]. Since the ZnO refraction indices in the UV and GL region are about 2.4 and 2.0 respectively, the critical angle of the total internal reflection is less than 30°. As a result, the optical

losses can be significantly reduced so that the WGMs can provide an attractive means to increase luminescence efficiency in optical resonators. Among other optical resonators, ZnO microdisks are of a particular interest. Microdisk resonators support propagation of WGMs, enabling technologies like bright LEDs, sensing and low threshold lasers [235-238]. As compared to one-dimensional structures, such as nanowires and nanorods, hexagonal microdisk resonators employing WGMs are promising due to their potential applications in nonlinear optical devices. However, fabrication of microdisks is non-trivial, as they require undercutting the active layer to achieve vertical light confinement.

Recently, numerous works on ZnO micro- and nanostructures with a moderate level of light confinement and increased luminescence efficiency were reported [79, 81, 82]. However, most of the WGMs of ZnO structures are formed on a Si substrate. Since the refractive index of Si is ~ 3.5 in the visible range, which is higher than that of ZnO (~ 2.0). Therefore, efficient light reflection may be difficult as total internal reflections do not happen from low to high refractive index material. Furthermore, while some attributed the emission enhancement to the presence of WGMs, most of previous work showed excitonic WGM is in the UV range [84, 90, 239], which is not suitable for visible applications. In addition, the ZnO structures were not well separated from each other, which make it challenging for realistic applications as WGMs resonators.

In this chapter, bottom up growth of well isolated ZnO microdisks on SiO_2 substrate is demonstrated. The proper substrate is chosen since refractive index of SiO_2 is less than ZnO, producing efficient light enhancement. By controlling the amount of raw materials and the size of the substrate, the ZnO microdisks are grown vertically and sparsely on the substrate. Optical characterization of ZnO microdisks was performed using low temperature (80 K) CL imaging and spectroscopy. The microdisks exhibited CL locally distributed near the hexagonal boundary of the ZnO microdisks. High resolution CL spectra of the ZnO microdisks revealed WGMs emission. The experimentally observed WGMs were in excellent agreement with the predicted theoretical positions calculated using a plane wave model. Raman spectroscopy confirms the high quality of the ZnO material. High resolution CL studies clearly

reveal that the resonators exhibit green emission and clear presence of WGMs with quality factors of ~ 60 and ~ 90 in ZnO microdisks of diameter 5μm and 9 μm, respectively. The position of the WGMs is supported using a plane wave model.

7.2 Growth of ZnO microdisks

Synthesis of the ZnO microdisks was carried out in a conventional horizontal tube furnace. No catalysts, no carrier gases, and low pressure were used in the experiment. All the reactions occurred in the furnace at ambient atmospheres, and 1 μm thick thermally grown SiO_2 on Si (100) wafers (1 cm × 2 cm) were used as substrates for ZnO microdisk fabrication. The setup of the growth of ZnO microdisks is shown in Figure 7.1. The substrates were cleaned with acetone and isopropanol by ultra-sonication. ZnO powders (200 mg) were mixed with graphite powders (200 mg) according to the weight ratio of 1:1 and put into a small boat as a source material. Before the boat was inserted into the horizontal tube, only the tube was pushed into the furnace and rapidly heated up to 1050 °C from the room temperature. Then, the boat filled with the source material was pushed into the center of the horizontal tube under atmospheric condition. Zn vapor was produced through the carbothermal reduction of ZnO powder by graphite, which acts as a reducing agent. With the increase of the concentration of the Zn vapor, Zn atoms condense and form liquid Zn clusters on the substrate and in the quartz boat. At the same time, the Zn vapor was reoxidized by oxygen in air at the nucleation sites to facilitate the formation of ZnO microdisks. After heating for 5 minutes with the substrate at the same temperature, the boat with the source materials was immediately removed from the furnace quickly and finally the system was cooled down to the room temperature in several minutes to limit the vertical growth to less than 10 μm. After the reaction, a large amount of ZnO microdisks were formed on the substrate. The control of source materials and carrier gas influences defect states of ZnO, resulting in different morphology and amount of defects so that it gives rise to different visible luminescence of DL centers.

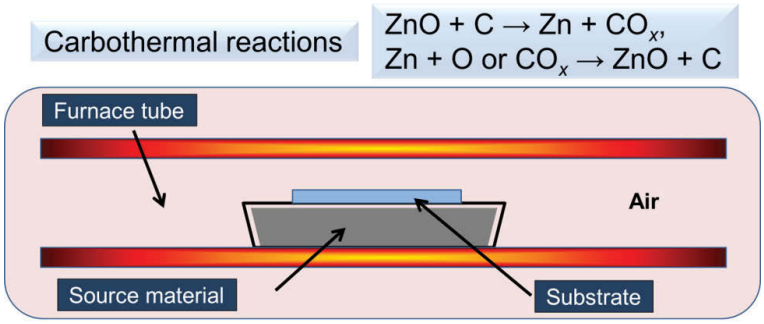

Figure 7.1. ZnO microdisk growth setup in the tube furnace.

7.3 Characterization of ZnO microdisks

The SEM analysis was performed using a Zeiss Supra 55VP SEM high resolution field emission SEM operating in secondary electron mode to examine the morphology and size of the ZnO microdisks. Raman spectroscopy was used to investigate the structural properties of the ZnO microdisk and the spectral range was set from 250 cm^{-1} to 650 cm^{-1} to detect Raman peaks relevant to ZnO. Since the later excitation could pass through the substrate, a bare SiO_2 substrate was also measured to compare with the spectrum of the ZnO microdisk.

CL measurements were carried out at liquid nitrogen temperature (80K) using a Gatan Mono-CL system attached FESEM with an accelerating voltage of 15 kV. The monochromator with the attached Hamamatsu S7011-1007 CCD sensor was used for investigating the detailed WGMs emission with high-resolution CL spectra. Once CL spectra were collected for high resolution of 0.05 nm / pixel, wavelength calibration was performed by measuring atomic spectral lines of mercury or neon lamp after the acquisition of the CL spectra. ZnO microdisks with diagonal width of 5 μm and 9 μm were selected under optical microscopy to investigate WGMs behaviors.

7.4 Observation of WGMs from ZnO microdisks

7.4.1 Structural analysis

An optical resonator is a transparent body of certain shape consisting of a substance with a high refractive index, surrounded by air. Such a structure has the ability to confine and guide light inside the resonator, thus it can be utilized in photonic applications of optical fibers or waveguides. Figure 7.2(a) and 7.2(b) show SEM secondary electron images at 20 kV of the as-grown 5 μm diameter ZnO microdisk. The density of the microdisks changed across the substrate surface (not shown), but isolated ZnO microdisks were always observed due to the lack of nucleation sites and source materials, resulting in the ZnO forming sparsely. Controlled growth of isolated microdisks is vital for future devices fabrication and proper spectroscopy studies. The perfectly hexagonal symmetry of the sample on the top can be clearly seen from the microdisks in Figure 7.2(a). The diameters of the microdisks were in the range of 3 μm up to 15 μm. Figure 7.2(b) shows a side view of SEM image of an individual ZnO microdisk. The diameter of the microdisk reduces from top to bottom and the length of the microdisk is about 5 μm. It can be seen that the top of the microdisk has well defined symmetry and very smooth edge facets that are likely to support WGMs propagation. The use of lower refractive index substrate (SiO_2) than ZnO is efficient for light confinement due to the reduction of light absorption into the substrate.

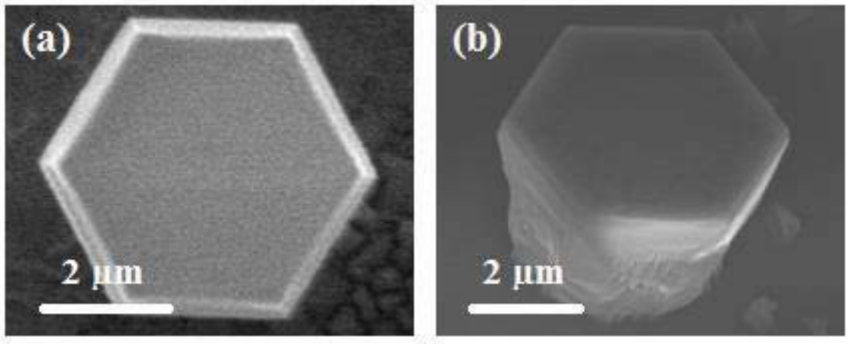

Figure 7.2. (a) Top and (b) side-view SEM secondary electron images of ZnO microdisk at an operating voltage of 20 kV. A well-defined hexagonal shape is clearly visible.

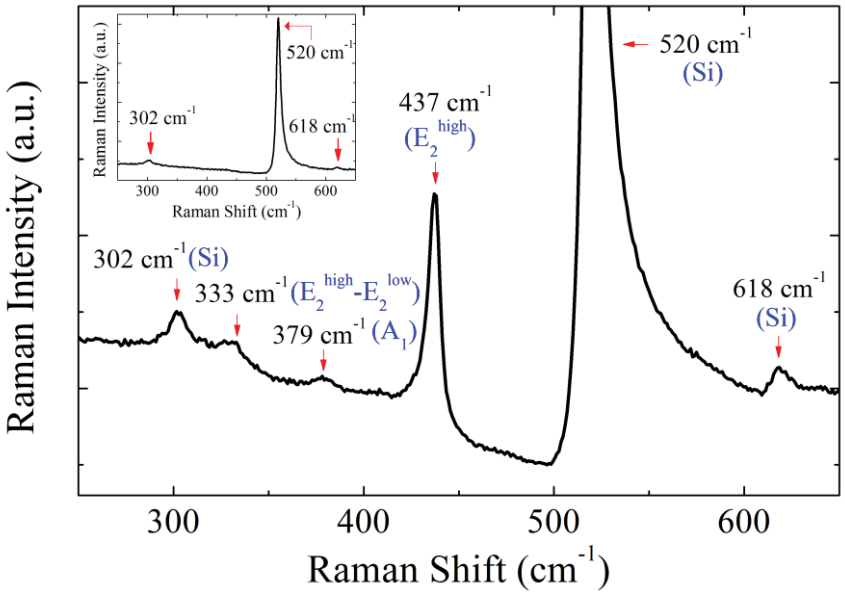

Figure 7.3. Raman spectrum of the ZnO microdisk confirming a high quality wurtzite structure. The Raman peak at 437 cm^{-1} is associated with the hexagonal wurtzite ZnO optical photon E_2^{high} mode. The strong peak at 520 cm^{-1} is associated with the Si substrate.

Figure 7.3 shows the Raman spectrum recorded from the ZnO microdisk using 633 nm line of a Renishaw He-Ne laser. Since the excitation laser source can penetrate into the substrate, a Raman spectrum of a bare substrate was also collected. The inset shows the Raman spectrum of the bare substrate that the peaks are seen at 302 cm^{-1}, 520 cm^{-1}, and 618 cm^{-1}. Thus, one very strong peak at 520 cm^{-1} and two weak peaks at 302 cm^{-1} and 618 cm^{-1} are attributed to the Si substrate which are the transverse optical phonon [240]. Especially, the peak at 618 cm^{-1} is only observed in boron doped Si, which is consistent of the sample properties since the used Si substrate is boron doped. The Raman peak at 437 cm^{-1} with relatively strong intensity is a typical Raman active branch of hexagonal wurtzite ZnO originated from the optical phonon E_2^{high} mode [241, 242]. In addition, other two peaks for the ZnO microdisk at 333 cm^{-1} and 379 cm^{-1} can be assigned to the E_2^{high} – E_2^{low} (multi-phonon process) and A_1 (longitudinal optical phonon) modes, respectively [243]. C. Xu et al. also investigated that the peak at 379 cm^{-1} is also relating to defects in ZnO [244]. The FWHM of the E_2^{high} mode at 437 cm^{-1} is ~ 7 cm^{-1}, narrower than the typical reported values for ZnO structures (~ 12 cm^{-1})

[245, 246]. Thus, the narrow and strong E_2^{high} mode combined with a very weak A_1 mode confirm that the fabricated ZnO microdisks have predominantly wurtzite crystal structure.

7.4.2 Optical properties of ZnO microdisks

To characterize the optical properties of the ZnO microdisks, CL measurement of the samples were carried out at 80 K with an accelerating voltage of 15 kV inside a SEM (FEI Quanta). In order to investigate the CL characteristics, the area in which the microdisks are not densely distributed was chosen. To visualize the light emission from the ZnO microdisk, the spatially resolved CL of the ZnO microdisks was collected by a photomultiplier tube connected to one end of the Oriel MS257 1/4 m monochromators. With proper settings of the grating and the position of the center wavelength, monochromatic CL images at different wavelengths can be obtained. The monochromatic CL image of the vertically grown and isolated hexagonal ZnO microdisk at 530 nm is shown in Figure 7.4(a). As can be seen in the image, the GL is not distributed uniformly across the microdisk, but is locally concentrated at the hexagonal boundary of the microdisk. Figure 7.4(b) shows a CL spectrum of the side and center region, respectively. The beam positions are marked as red and blue circles. The excitonic emission peak at 378 nm (3.28 eV) is almost equal in intensity at the boundary and center of the microdisk. The stronger peak at the green spectral range, centered at around 530 nm is the green emission from the ZnO. As can be seen in Figure 7.4(b), the luminescence intensity of the green emission is significantly stronger near the boundary of the microdisk, likely to be enhanced by the total internal reflections of light within the microdisk. Such an enhancement is often associated with the presence of WGMs, as discussed below. CASINO Monte Carlo modeling of the electron interaction volume at 15 kV shows that the lateral spread of the electron beam in ZnO is $\leq$ 500 nm (represented by a circle in the inset of Figure 7.4(a)) indicating that the increase in CL towards the periphery of the ZnO microdisk is not related to excitation artifacts due to forward scattered electrons [247].

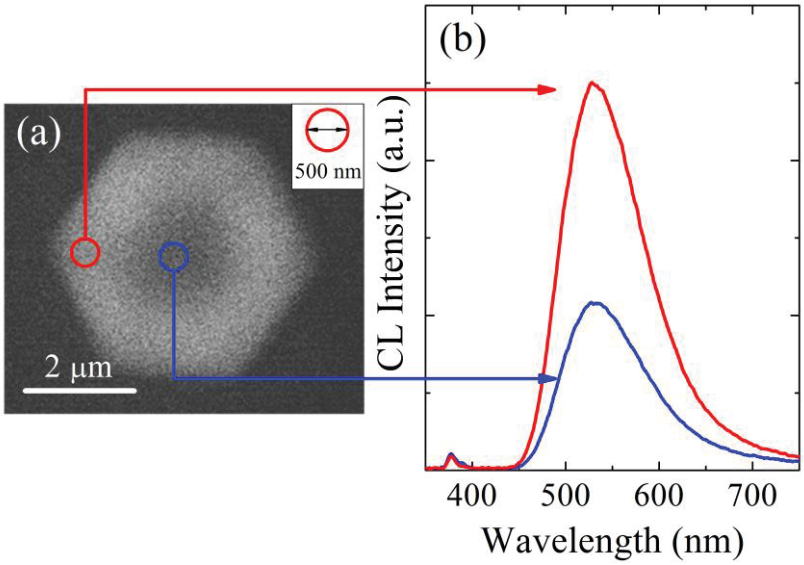

Figure 7.4. (a) Monochromatic CL image of the ZnO microdisk at 530 nm at 15 kV. Inset is 500 nm lateral spread of the interaction volume of the electron beam at 15 kV. (b) Representative CL spectra recorded from the side regions of the microdisk, and the center regions of the ZnO microdisk, respectively. The local excitation spots are indicated by red and blue circles in (a). There is a significant difference of green emission between the side and the center region.

To investigate the CL in more details, high resolution CL spectra (1.5 nm spectral resolution), Hamamatsu CCD detector) from the periphery of the ZnO microdisks were recorded. The typical CL spectra of a 5 μm and a 9 μm microdisks, are shown in Figure 7.5(a) and 7.5(b), respectively. Each CL spectrum clearly shows the evolution of the WGMs. As expected, the disk with larger diameter exhibits narrower spacing between the observed resonator modes. The size dependence of the structured green CL spacing confirms that the enhanced edge emission in our ZnO microdisks is clearly unrelated to increased surface emission widely reported in ZnO nanowires due to surface band bending effects or an increased concentration of surface defects [248, 249]. The energy spacing between the emission peaks from the 5 μm and 9 μm microdisks is in the range 23 – 24 meV and 34 – 40 meV, respectively. These spacing values are significantly smaller than the longitudinal optical phonon energy of 72 meV, indicating they are not related to the vibronic states as reported previously by Reynolds et al. [250].

The spectra were fitted to a sum of multi-peaks using the Lorentzian deconvolution method centered at each resonant wavelength as shown in Figure 7.5(a) and 7.5(b) (fitted red curve). Five and eight Lorentzian distributions reproduced the CL spectra reasonably well in Figure 7.5(a) and Figure 7.5(b) respectively. The dashed lines in Figure 7.5(a) and 7.5(b) represent predicted 5 and 8 discrete optical mode numbers of WGMs located at each resonant peak for small and large microdisks.

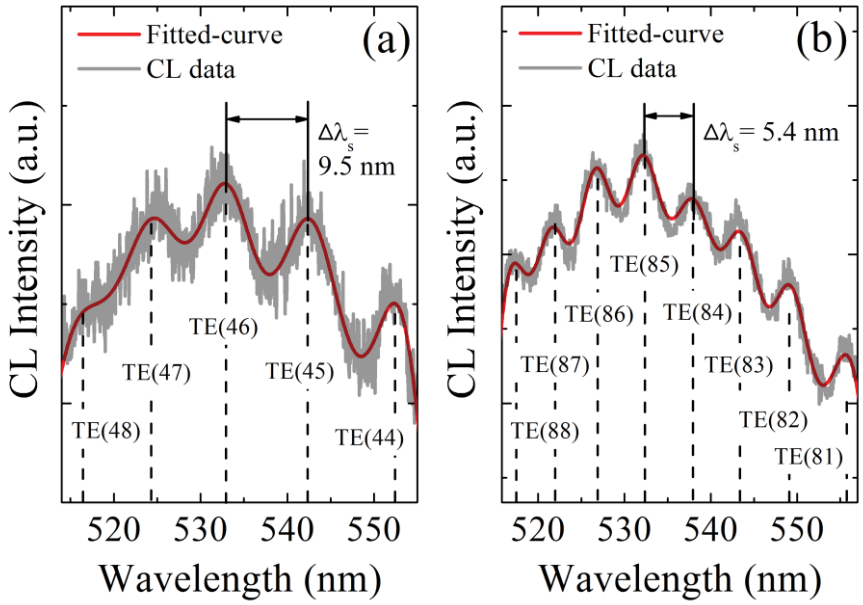

Figure 7.5. (a, b) High resolution CL spectra from the peripheral area of the ZnO microdisks shows a series of peaks corresponding to WGMs with a green emission band using Lorentzian deconvolution method. The integers are the mode numbers for respective resonant mode peaks; (a) 5 μm and (b) 9 μm of the microdisks.

7.4.3 Investigation of the light confinement in ZnO microdisks

Various mechanisms can account for the optical resonance. Since usually the random lasing is caused by multiple scattering in a disordered medium [127], the enhanced light emission from the ZnO microdisk is not attributed to the random lasing as the light emission is observed from only a single ZnO microdisk. In terms of geometrical optics, three kinds of resonant cavity modes are possible, FPMs, quasi-WGMs, and WGMs. As explained before, FPMs is formed by the two opposing interface of the microdisks so the light can travel back and forth between two parallel mirrors. The

observation of this type of mode has been reported by Zhao *et al.* although the cavity size in their work is much larger [230]. The hexagonal-shaped dielectric cavity can also support quasi-WGMs and WGMs. The quasi-WGMs and WGMs are formed when the light ray strikes the boundary at 30° and the boundary at 60° relative to the normal to the boundary surface, respectively. The light is totally reflected and the luminescence intensity is enhanced by the lateral sides of the ZnO microdisks with the critical angle of the total internal reflection (~ 25.8°) at the ZnO/air boundary [251]. Because of small critical angle and the large refractive index of ZnO in the visible spectral range, multiple total internal reflections in the ZnO microdisks are easily achieved. Figure 7.6 shows three possible resonance modes that can be produced in the hexagonal ZnO microdisk indicated by the grey arrows for light reflection or circulation: (a) a FPM, (b) a quasi-WGM, and (c) a WGM.

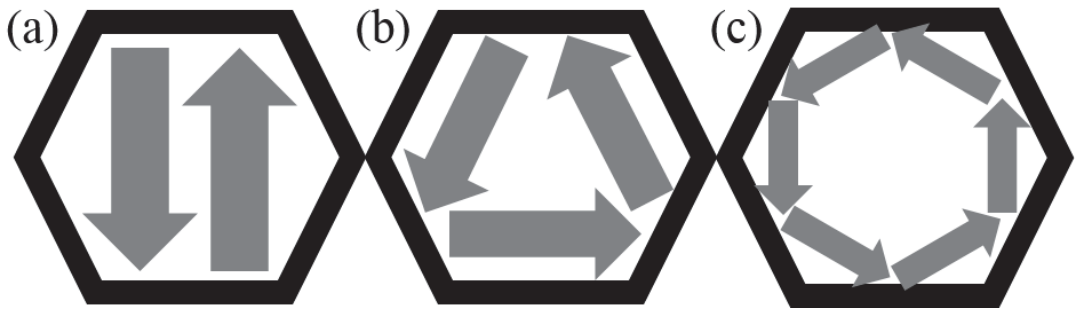

Figure 7.6. Different types of resonance mode in the hexagonal shape of an optical resonator. (a) a FPM, (b) a quasi-WGM, and (c) a WGM.

For optical resonators it is important to analyze the observed resonance to understand the nature of the light confinement. The mode spacing and the mode resonances are representative analysis to show that the ZnO nanostructures support the propagation of WGMs. Firstly, the mode spacing can be analyzed using a classical plane wave model. For possible resonant modes, the mode spacing $\Delta\lambda_S$ is defined as

$$\Delta\lambda_S = \frac{\lambda^2}{L(n - \lambda\frac{dn}{d\lambda})} \tag{7.1}$$

where λ is the resonant wavelength, L is the cavity path length, n is the refractive index of ZnO, and the $dn/d\lambda$ is the Sellmeier's first-order dispersion relation, respectively. For all of the calculations, two different sizes of the ZnO microdisks were chosen (5 μm and 9 μm) to find out which modes were formed to the microdisks. In the case of FPMs, calculated path lengths L are $2\sqrt{3}R_{small}$ = 8660 μm and $2\sqrt{3}R_{large}$ = 15590 μm for 5 μm microdisk and 9 μm, respectively, where R is the radius of the resonator. The calculated mode spacing $\Delta\lambda_S$ for FPMs at 533 nm is about 14.4 nm and 8.0 nm for small and large microdisk. If the resonant modes were quasi-WGMs, the calculated mode spacing can be deduced about 11.1 nm and 6.2 nm for small and large microdisk, respectively. These all values are much larger than the experimentally observed value since experimentally observed mode spacing $\Delta\lambda_S$ is 9.5 nm and 5.4 nm for small and large microdisk, respectively. This indicated that the resonant modes may not be attributed to the FPMs or quasi-WGMs. If the resonant modes were WGMs, the calculated mode spacing is 9.6 nm and 5.3 nm for small and large microdisks according to the above equation, which is almost consistent with the experimentally observed mode space in Figure 7.5.

Secondly, a classical simple plane wave model is used to study the observed modes [76, 84]. The main idea is that the light wave circulates around exploiting the process of multiple total internal reflections and finally interferes with itself when having completed one full circulation within the resonator. Considering the number of the total internal reflections, refractive index, and path length, the mode equation is obtained which describes the resonance model and the number of interference orders of a ZnO microdisk for each resonance mode. The constructive interference can be generated and the standing wave forms if the total phase shift along the path in the microdisk is an integer multiple of 2π [232]. The results of theoretical modeling show that the eigenmodes of such a hexagonal cavity can be numbered by the integer mode number N. For the FPMs, the constructive interference condition is described as follows;

$$\lambda = \frac{2nL}{N} \tag{7.2}$$

where N is the interference order. The integer $N \geq 1$ characterizes the interference order of the resonance, which is in this case identical with the respective optical resonance number. For large mode numbers, a simple plane wave model has been deduced. According to the equation above, the constructive interference at green emission is formed with the resonant wavelength of 525 nm and 528 nm when the integer N is 33 and 59 for small and large microdisks, respectively. As compared to the experimentally observed positions of peaks, FPMs do not fit the resonant peak positions. In addition, the two opposite side surfaces of the microdisks are not perfectly parallel. In such a tapered nanostructure, the top and down surface could not form a proper FPMs resonator and provide good confinement for light transport as the light is transported between these two opposite surfaces for FPMs. Thus, the FPMs barely form in the ZnO microdisks.

Taking into account the polarization-dependent negative phase shift that occurs during the process of the total internal reflection, the constructive interference condition for the WGMs is given by

$$\lambda = \frac{3\sqrt{3}R}{N + \frac{6}{\pi}\arctan(\beta\sqrt{3n(\lambda)^2 - 4})} \tag{7.3}$$

where $n(\lambda)$ is the wavelength-dependent refractive index and the factor β refers to the different polarizations which is equal to n^{-1} and n for the TM and the TE polarization, respectively [76, 90]. As described in Figure 7.6, the light can be assumed to circulate around only within the cross section of the optical resonator. The optical mode patterns can be obtained by solving the above wave equation in its two dimensional form. Hence, two decoupled types of polarizations can occur, namely TE polarized modes (electric field (E) $\perp$ c-axis (c)), and TM polarized modes ($E \parallel c$) in a hexagonal optical resonator. While the electric field is transverse to the longitudinal axis of the resonator for TE modes, the magnetic field is transverse to the longitudinal axis of the resonator in TM modes. In addition, the wavelength-dependent refractive indices at the TM-WGMs polarization and TE-WGMs polarization are expressed as the Sellmeier's dispersion function:

$$n(\lambda)_{TM} = \left(1 + \frac{2.9535\lambda^2}{\lambda^2\text{-}82.30^2} + \frac{0.1660\lambda^2}{\lambda^2\text{-}358.60^2} + \frac{0.1050\lambda^2}{\lambda^2\text{-}1750^2}\right)^{\frac{1}{2}} \tag{7.4}$$

$$n(\lambda)_{TE} = \left(1 + \frac{2.4885\lambda^2}{\lambda^2\text{-}102.30^2} + \frac{0.215\lambda^2}{\lambda^2\text{-}372.60^2} + \frac{0.2550\lambda^2}{\lambda^2\text{-}1850^2}\right)^{\frac{1}{2}} \tag{7.5}$$

where $n(\lambda)_{TM}$ and $n(\lambda)_{TE}$ are refractive indices of ZnO for TM mode and TE mode, respectively [83, 252]. Figure 7.7 shows refractive indices of a ZnO microdisk against wavelength which are based on the equations above. It can be seen that both modes decrease with increasing wavelength, but the refractive index $n(\lambda)_{TM}$ is larger than $n(\lambda)_{TE}$ at the same green wavelength region, resulting in different peak positions from the calculations using the plane wave model.

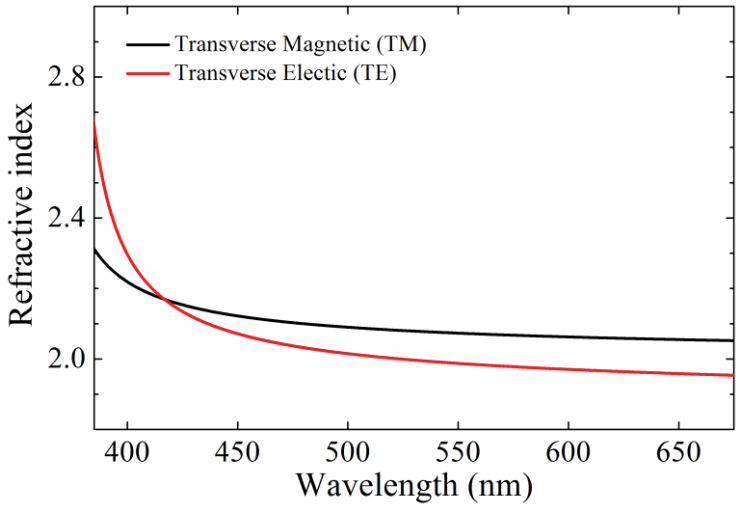

Figure 7.7. Wavelength-dependent refractive indices of a ZnO microdisk were deduced using Sellmeier's dispersion functions.

The peak positions in obtained from the CL spectra are fit to those predicted by Eq. 7.3 as can be seen from Figure 7.5. According to the constructive interference condition for WGMs above, the constructive interferences at green emission were formed with the resonant wavelength of 532 nm when the integer N is 46 and 85 for small and large microdisks, respectively. As compared to the experimentally observed positions of peaks, WGMs model with TE mode satisfied the resonant peak positions.

To check the consistency with other resonant peaks, all of the peak positions in obtained from the CL spectra compared to those calculated by Sellmeier's dispersion function, as can be seen from Figure 7.5(a) and 7.5(b). The solid lines in Figure 7.5(a) and 7.5(b) represent predicted 5 and 8 discrete optical mode numbers located at each resonant peak for small and large microdisks for TE polarization mode. Based on the calculation, the wavelength is gradually varied from 514 to 553 nm with the step of 10 ~ 11 nm for the small microdisk and from 517 to 555 nm with the step of 5 ~ 6 nm for the large microdisk, each corresponding to a refractive index of TE mode, then the resonant wavelengths related to the integer numbers *N* were established. For the small microdisk, the calculated 5 integers are 48, 47, 46, 45, and 44, located at 514 nm, 523 nm, 533 nm, 543 nm, and 553 nm, respectively. The experimentally observed values are 515 nm, 523 nm, 533 nm, 543 nm, and 532 nm, which are in good agreement with the result obtained from the calculated peak positions with error < 1nm to the values obtained. For the large microdisk, the calculated 8 integers are 88, 87, 86, 85, 84, 83, 82 and 81, located at 517 nm, 522 nm, 527 nm, 532 nm, 538 nm, 543 nm, 549 nm and 555 nm, respectively. The experimentally observed values are 517 nm, 522 nm, 527 nm, 532 nm, 538 nm, 543 nm, 549 nm and 555 nm. The observed resonant wavelengths for the large microdisk in experiment also match with the theoretical values very well. Therefore, the WGMs plane wave model also supports that the spatial distribution near hexagonal boundary is due to the WGMs-enhanced luminescence. Theory indicates that both of the optical conduction modes (TM and TE) can exist simultaneously in the resonator. However, the WGMs observed from the ZnO microdisks were mostly TE polarized since typically TM polarized emission is much weaker and broader than TE modes [87]. Thus the TM polarization mode from ZnO is difficult to be detected at ZnO/air interface relative to the TE polarization mode.

The *Q* factor of both sizes of the ZnO microdisks can be calculated from the WGMs emission mode. For a resonant mode, the *Q* factor can be calculated with the formula:

$$Q = \frac{\lambda}{\Delta\lambda} \tag{7.6}$$

where λ and $\Delta\lambda$ are the peak wavelength and its FWHM, respectively. Figure 7.8 shows the CL spectrum of 5 µm ZnO microdisk highlighted with the peak wavelength and its FWHM. According to Figure 7.8, the values of the FWHM of the resonant mode were observed to be about 9.2 nm and 5.5 nm at the wavelength of 532 nm for small and large microdisks, respectively. Therefore, the corresponding Q factors can be estimated to be about ~ 60 and ~ 90 for small and large microdisks, respectively. The relatively low Q factor is mostly due to the poor vertical confinement of light, contribution from losses such as defect absorption, and the light leakage at the air/ZnO interfaces. Moreover, the surface roughness of the cavity can also influence the reflection of light since tapered area of the ZnO microdisks is not sufficiently smooth as shown in Figure 7.2(b).

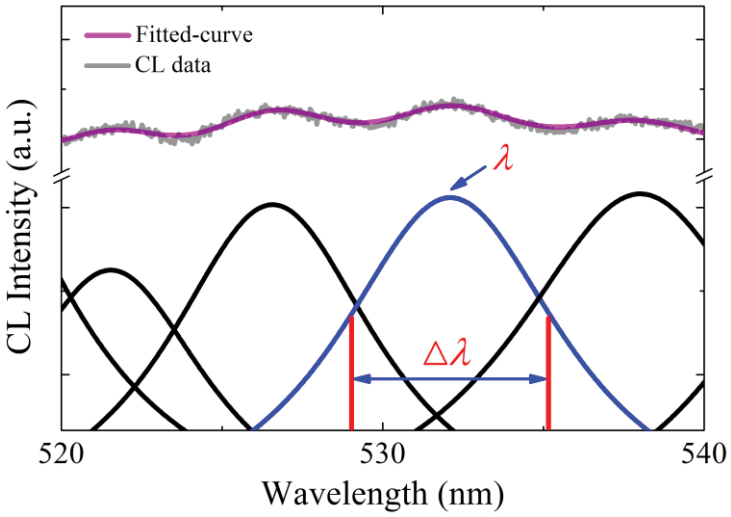

Figure 7.8. CL spectrum of 9 m ZnO microdisk showing the peak wavelength and its FWHM for calculation of the Q factor.

The reflectivity (r) for a hexagonal WGM cavity can be deduced using the expression:

$$Q = \frac{\pi n m D r^{m/4}}{2\lambda(1-r^{m/2})} \sin\frac{2\pi}{m} \tag{7.7}$$

where D is the diagonal of the hexagon and m is the number of the side facets [253]. Based on the experimental Q factor of 90 and 60, the deduced reflectivity is ~ 50 % for the peak at 535 nm, which is reasonable for the total internal reflection at the

ZnO/air boundary considering the cavity loss at the corners, because there may be some energy dissipation at the reflection point caused by the surface defects.

While a hollow metallic resonator is called closed cavity, a dielectric resonator is an open cavity. No energy is radiated from the hollow resonator so that the whole radiation field is restricted inside the metallic cavity. For the hollow resonator, the boundary conditions for the electric and magnetic field lead to a complete suppression of wave propagation outside the resonator, resulting in a discrete set of eigenmodes related to a discrete spectrum of eigenmode energies. However, for the dielectric resonator, due to the continuity conditions for the electric and magnetic field at the boundary of the optical resonator, the radiation field is not completely constrained to the optical resonator itself, but can be extended to infinity. This causes a permanent radiation loss of energy and hence, every possible field distribution decays exponentially with a lifetime, therefore not representing a steady state solution. Further improvement of the device is possible by limiting the vertical growth of the microdisk, therefore creating a properly undercut structure. More precise fabrication control (e.g. use of silica beads) to produce undercut structures will reduce light absorption into the substrate and thus high Q factor is achievable with sharp WGMs resonance peaks.

7.5 Conclusions

In summary, ZnO microdisk resonators were grown vertically and sparsely on SiO_2 substrates without catalysts, templates, and carrier gases. The Raman data shows that the material is predominantly hexagonal ZnO. Monochromatic CL images and spectra of the ZnO microdisks showed that CL is dramatically enhanced at the hexagonal boundary of the ZnO microdisks. High spectral resolution CL measurements revealed WGMs presence with moderate quality factors. Theoretical analysis of the wave propagation inside the resonator confirms that the observed resonances are WGMs. Further studies to realize ZnO resonators with higher quality factors by isolating the top layer through undercut will be of a great importance to improve the ZnO devices.

These results indicate that the ZnO microdisks may be a prime candidate for the advance of microdisk green LEDs and other applications in photonics and quantum information.

Chapter 8

Conclusions and outlook

In summary, this thesis provides the foundations for nanophotonics using ZnO, including the defect-related visible emission, quantum photonics, heterostructure devices, and optical based on ZnO nanostructures. First of all, structural and optical characterization of as-received and annealed ZnO to utilize optoelectronic devices were investigated using several annealing processing and characterization techniques. The effects of annealing on the structural and luminescent properties on ZnO were studied. The annealed ZnO nanoparticles had significant defect-related emission after annealing in O_2 and Zn vapor conditions at high temperature over 700 °C. Defect creation and removal in ZnO is achieved at elevated temperatures. Annealing in O_2 and Zn vapor creates different GL bands and the emissions are attributed to the different defects. High temperature annealing creates other visible luminescence, indicating that the DL band in ZnO has multiple origins.

Secondly, SPSs from ZnO nanoparticles and sputtered thin films are presented through PL and HBT measurements. ZnO clearly shows quantum behavior and bright fluorescence with high count rates. The emitters are stable under optical exciation, thus can be used for quantum photonic applications. Surface termination by hydrogen doping and PMMA coating influences the density of emitters and stability. The origin of the emitters has not been determined yet, but our measurements suggested that the emitters could be localized charge traps.

After single photon emission from ZnO was successfully observed under the optical excitation and electrical excitation from defects in ZnO is discussed. To engineer electrical excitation, ZnO/Si heterostructures were fabricated and light emission from the devices is successfully achieved under the forward bias. Electrically driven SPSs from ZnO are not observed, but the EL is bright and stable. Further studies to increase

the efficiency and density of light emission can contribute to the SPSs under the electrical excitation.

Finally, cavity effects exhibiting WGMs emission are observed. Because of the WGMs, luminescence spectra of visible region are amplified. Enhanced light emissions are observed from GL peak from ZnO optical cavities with moderate Q factors. Achievement of optical cavity with high Q factor should be able to provide a good platform for future nanophotonic applications.

Outlook

Even though ZnO attracts a considerable interest across nanophotonics and material science, there are still important issues that are in need of further investigation before this material can be used in practical devices. New ideas for fabrication techniques are required to achieve high Q factor with a proper undercut, especially in the red area ranging from 1.5 eV to 2 eV, which has emerged ZnO SPSs so far. So far, SPSs in ZnO has been only observed by thermal annealing process at 500 ^{o}C in air since the particular processes reduces V_O and produce V_{Zn} as mentioned in Section 2.2. Other annealing or doping processes can generate SPSs more efficiently and increase the probability of SPSs observation. ZnO nanostructures that exhibit WGMs and lasing emission can be generated by carbothermal reduction or chemical vapor deposition of ZnO with graphite. By changing the synthesis parameters, different colors of WGMs and lasing can be realized based on what structures need to be obtained, such as nanodisks, nanoneedles, and nanowires. For example, positioning a substrate at high temperature (> 1000 °C) could form ZnO microdisk, but ZnO nanowires could be fabricated by placing a substrate at low temperature (~ 650 °C) [254]. It also determines different reaction temperatures, resulting in different light emission. Dedicated studies to correlate between growth conditions, SPSs generation and device performance will be a crucial step in developing ZnO nanophotonic technologies.

Size-tunable ZnO nanostructure with flexible substrate would provide different cavity modes and then the resonant wavelength can be optimized to emit SPSs in the cavities. Rather than changing the resonant wavelength, lower excitation wavelengths (~ 400 nm) in cryogenic temperature could also provide visible emission at the green spectral range, so confocal scanning using blue laser can excite different position of single emitters. Moreover, ZnO that hosts single emitters should be integrated with proper p-type heterostructure of ZnO to generate EL.

Recently, Konidakis et al. presented ZnO nanolayers synthesized inside the capillaries of a photonic crystal fiber [255]. The periodic photonic crystal structure confines the light propagation through the fiber, thus light loss can be reduced. This structure can

be potentially used in an innovative approach to fabricate ZnO cavities, exploiting lasing properties such as random lasers. Hybrid structures of ZnO/GaN heterojunction can develop different emission depending on the ZnO structures or schematics. This electrical excitation also can offer WGMs ASE, which can open the door for this use as fundamental building blocks in quantum photonics. Further optimization in synthesis of ZnO nanostructures and device engineering will pave the way to employ ZnO in 21th century quantum photonic technologies.

Appendix A. CL system correction

For accurate CL measurements, the collected data have to be corrected for the response of the system in intensity and wavelength. Since the OceanOptics spectrometer has a wide wavelength range from ~ 200 nm to ~ 1000 nm, effects of the optical absorption of the light by the optical fiber and mirror need to be considered after collection of CL data. An Oriel 63358 Quartz Tungsten Halogen calibrated lamp of known spectral profile was used for CL intensity calibration. The system intensity calibration curve is calculated according to the following equation:

$$\text{Corrected response curve} = \frac{\text{Normalized standard intensity}}{\text{Normalized measured intensity}} \qquad \text{(A.1)}$$

Figure A.1(a) shows the measured intensity as a function of wavelength as well as the standard irradiance curve. Figure A.1(b) is the calculated response curve from the equation above.

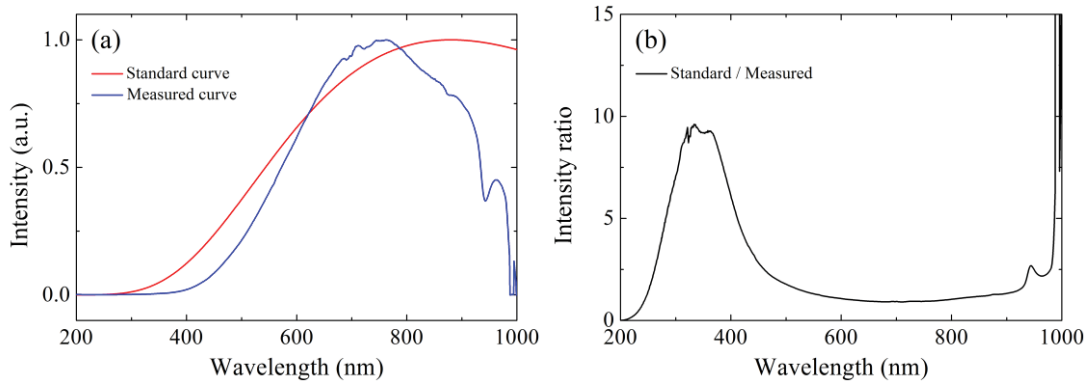

Figure A.1. (a) CL spectra of the tungsten halogen lamp (red curve) and the standard irradiance using the OceanOptics detector (blue curve). (b) System optics response curve calculated from Eq. A.1.

A result of the CL spectrum using the Hamamatsu CCD shows CL intensity against pixel, so pixel to wavelength calibration is needed. In addition, CL spectra obtained from the Hamamatsu CCD covers narrow wavelength range of the emission with the large number of gratings (~ 50 nm, 1800 lines/mm), wavelength calibration for CL spectral analysis was performed by measuring atomic spectral lines of neon lamp after

the acquisition of the ZnO spectra for visible luminescence. Figure 3.7 shows CL spectra of a neon lamp as well as the calculated wavelength calibration curve using the Hamamatsu CCD. No intensity calibration is required for the range of 50 nm using the Hamamatsu CCD.

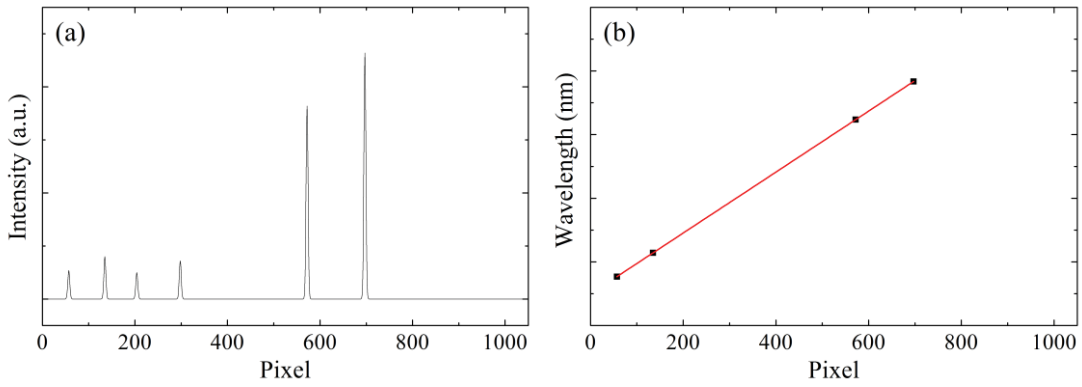

Figure A.2. Wavelength calibration for the Hamamatsu CCD with the center wavelength of 530 nm. (a) CL spectrum of the mercury lamp. (b) A linear wavelength calibration curve to convert the unit from pixel to wavelength.

CL emission peaks show a symmetric Gaussian or Lorentzian distribution in energy. Thus, the wavelength calibration is converted to energy unit (eV) according to the equation:

$$\text{Photon energy in eV} = \frac{1239.84}{\lambda\,(nm)}. \tag{A.2}$$

The measured CL intensity also needs to be corrected to have equal steps in ΔeV by multiplying $I(\lambda)$ by λ^2 because the spectrometer measures photons per second in a Δ nm interval in λ.

$$\frac{\Delta E}{\Delta \lambda} = \frac{d}{d\lambda}\left(\frac{hc}{\lambda}\right) = -\frac{hc}{\lambda^2}, \qquad I(eV)\cdot\Delta eV = I(\lambda)\cdot\Delta\lambda\cdot\lambda^2 \tag{A.3}$$

Appendix B. Normalization of the $g^2(\tau)$

The normalization of the $g^2(\tau)$ is obtained by the following equation:

$$g^2{}_{Norm}(\tau) = \frac{c(\tau)}{C_1 C_2 tw} \tag{B.1}$$

where $c(\tau)$ is the recorded coincident count rate, C_1 and C_2 are the count rates from each APD, t is the integration time, and w is width of the time bin. After the normalization is done, background correction needs to be considered. Generally, background emission is collected by moving the laser source few microns away from the bright spots, which does not show an antibunching behavior. The background-corrected $g^2(\tau)$ is given by

$$g^2{}_{Corr}(\tau) = \frac{g^2{}_{Norm}(\tau) - (1-\rho^2)}{\rho^2}, \text{ where } \rho = \frac{S}{S+B} \tag{B.2}$$

and S is the count rate from the bright spot and B is the count rate from the background. Since the bright spots may have different emission intensity (count rates), the term ρ is measured every time for each measurement.

Appendix C. List of Publications

Refereed journal publications

S. Choi, C. Ton-That, M. R. Phillips, and I. Aharonovich, "*Observation of whispering gallery modes from hexagonal ZnO microdisks using cathodoluminescence spectroscopy*", Applied Physics Letters, 103, 171102 (2013)

S. Choi, B. C. Johnson, S. Castelletto, C. Ton-That, M. R. Phillips, and I. Aharonovich, "*Single photon emission from ZnO nanoparticles*", Applied Physics Letters, 104, 261101 (2014)

K. S. Chan, C. Ton-That, L. Vines, **S. Choi**, M. R. Phillips, B. G. Svensson, C. Jagadish and J. Wong-Leung, "*Effects of high temperature annealing on defects and luminescence properties in H implanted ZnO*", Journal of Applied Physics D: Applied Physics, 47, 342001 (2014)

S. Choi, A. M. Berhane, A. Gentle, C. Ton-That, M. R. Phillips, and I. Aharonovich, "*Electroluminescence from localized defects in zinc oxide – toward electrically driven single photon sources at room temperature*", ACS Applied Materials & Interfaces, 7, 10, 5619 - 5623 (2015)

S. Choi, M. R. Phillips, I. Aharonovich, S. Pornsuwa, B. C. C Cowie, and C. Ton-That, "*Photophysics of point defects in ZnO nanoparticles*", Advanced Optical Materials, 3, 6, 827 (2015)

A. M. Berhane, **S. Choi**, H. Kato, T. Makino, N. Mizhochi, S. Yamasaki and I. Aharonovich, "*Electrical excitation of silicon-vacancy centers in single crystal diamond*", Applied Physics Letters, 106, 171102 (2015)

S. Khachadorian, R. Gillen, **S. Choi**, C. Ton-That, J. Maultzsch, M. R. Phillips, A. Kliem and A. Hoffmann, "*Effects of annealing on optical and structural properties of zinc oxide nanocrystals*", Physica Staus Solidi B: Basic Solid State Physics, 252, 11, 2620 – 2625 (2015)

S. Choi and I. Aharonovich, "*Zinc oxide nanophotonics*", Nanophotonics, 4, 1, 437 – 458 (2015)

Conference and workshop presentations

S Choi et al., "*Fabrication and optical properties of ZnO microdisk for whispering-gallery mode lasing applications*", International Conference on Nanoscience and Nanotechnology (ICONN), 2014, Adelaide, Australia

S Choi et al., "*Zinc oxide nanophotonics*", Australian Nanotechnology Network (ANN) Early Career Workshop, 2014, Sydney, Australia

S Choi et al., "*Zinc oxide nanophotonics*", Australian Nanotechnology Network (ANN) Early Career Workshop, 2015, Sydney, Australia

S Choi et al., "*Single photon emission from ZnO and its electroluminescence – promising approach for fabrication of quantum light emitting diodes*", 2015, European Materials Research Society (EMRS), Warsaw, Poland

S. Choi et al., "*Photophysics of point defects in zinc oxide nanoparticles*", 2015, Society of Photographic Instrumentation Engineers (SPIE.) Micro+Nano Materials, Devices, and Applications, Sydney, Australia.

S Choi et al., "*Single photon emission and electroluminescence from defects in ZnO*", International Conference on Nanoscience and Nanotechnology (ICONN), 2016, Canberra, Australia

Bibliography

1. S. Choi and I. Aharonovich, *Zinc Oxide Nanophotonics*, Nanophotonics, **4**, 437-458 (2015).

2. A. Janotti and C. G. Van de Walle, *Fundamentals of zinc oxide as a semiconductor*, Reports on progress in Physics, **72**, 126501 (2009).

3. M. Willander, O. Nur, Q. Zhao, L. Yang, M. Lorenz, B. Cao, J. Z. Pérez, C. Czekalla, G. Zimmermann and M. Grundmann, *Zinc oxide nanorod based photonic devices: recent progress in growth, light emitting diodes and lasers*, Nanotechnology, **20**, 332001 (2009).

4. C. H. Ahn, Y. Y. Kim, D. C. Kim, S. K. Mohanta and H. K. Cho, *A comparative analysis of deep level emission in ZnO layers deposited by various methods*, Journal of Applied Physics, **105**, 13502 (2009).

5. W. Liu, S. Gu, J. Ye, S. Zhu, S. Liu, X. Zhou, R. Zhang, Y. Shi, Y. Zheng and Y. Hang, *Blue-yellow ZnO homostructural light-emitting diode realized by metalorganic chemical vapor deposition technique*, Applied physics letters, **88**, 092101 (2006).

6. R. Konenkamp, R. C. Word and C. Schlegel, *Vertical nanowire light-emitting diode*, Applied physics letters, **85**, 6004-6006 (2004).

7. Ü. Özgür, Y. I. Alivov, C. Liu, A. Teke, M. Reshchikov, S. Doğan, V. Avrutin, S.-J. Cho and H. Morkoc, *A comprehensive review of ZnO materials and devices*, Journal of Applied Physics, **98**, 041301 (2005).

8. A. Djurišić, A. Ng and X. Chen, *ZnO nanostructures for optoelectronics: material properties and device applications*, Progress in Quantum Electronics, **34**, 191-259 (2010).

9. S. Studenikin, M. Cocivera, W. Kellner and H. Pascher, *Band-edge photoluminescence in polycrystalline ZnO films at 1.7 K*, Journal of Luminescence, **91**, 223-232 (2000).

10. Y. Fu, J. Luo, X. Du, A. Flewitt, Y. Li, G. Markx, A. Walton and W. Milne, *Recent developments on ZnO films for acoustic wave based bio-sensing and microfluidic applications: a review*, Sensors and Actuators B: Chemical, **143**, 606-619 (2010).

11. A. J. Morfa, B. C. Gibson, M. Karg, T. J. Karle, A. D. Greentree, P. Mulvaney and S. Tomljenovic-Hanic, *Single-photon emission and quantum characterization of zinc oxide defects*, Nano letters, **12**, 949-954 (2012).

12. N. Jungwirth, Y. Pai, H. Chang, E. MacQuarrie and G. Fuchs, *A single-molecule approach to ZnO defect studies: single photons and single defects*, arXiv preprint arXiv:1402.1773 (2014).

13. Q. Wan, Q. Li, Y. Chen, T.-H. Wang, X. He, J. Li and C. Lin, *Fabrication and ethanol sensing characteristics of ZnO nanowire gas sensors*, Applied physics letters, **84**, 3654-3656 (2004).

14. B. Lounis and M. Orrit, *Single-photon sources*, Reports on progress in Physics, **68**, 1129 (2005).

15. A. J. Shields, *Semiconductor quantum light sources*, Nature Photonics, **1**, 215-223 (2007).

16. J. L. O'Brien, A. Furusawa and J. Vučković, *Photonic quantum technologies*, Nature Photonics, **3**, 687-695 (2009).

17. H. Gibbs, G. Khitrova and S. Koch, *Exciton-polariton light-semiconductor coupling effects*, Nature Photonics, **5**, 273-273 (2011).

18. J. Reithmaier, G. Sęk, A. Löffler, C. Hofmann, S. Kuhn, S. Reitzenstein, L. Keldysh, V. Kulakovskii, T. Reinecke and A. Forchel, *Strong coupling in a single quantum dot–semiconductor microcavity system*, Nature, **432**, 197-200 (2004).

19. M. Humar, M. Ravnik, S. Pajk and I. Muševič, *Electrically tunable liquid crystal optical microresonators*, Nature Photonics, **3**, 595-600 (2009).

20. F. Vollmer and S. Arnold, *Whispering-gallery-mode biosensing: label-free detection down to single molecules*, Nature methods, **5**, 591-596 (2008).

21. C. Jagadish and S. J. Pearton, *Zinc oxide bulk, thin films and nanostructures: processing, properties, and applications*, Elsevier, (2011).

22. L. Schmidt-Mende and J. L. MacManus-Driscoll, *ZnO–nanostructures, defects, and devices*, Materials today, **10**, 40-48 (2007).

23. M. Lorenz, A. Rahm, B. Cao, J. Zúñiga-Pérez, E. M. Kaidashev, N. Zhakarov, G. Wagner, T. Nobis, C. Czekalla and G. Zimmermann, *Self-organized growth of ZnO-based nano-and microstructures*, physica status solidi (b), **247**, 1265-1281 (2010).

24. D. Bagnall, Y. Chen, Z. Zhu, T. Yao, S. Koyama, M. Y. Shen and T. Goto, *Optically pumped lasing of ZnO at room temperature*, Applied physics letters, **70**, 2230-2232 (1997).

25. S. Yu, C. Yuen, S. Lau, W. I. Park and G.-C. Yi, *Random laser action in ZnO nanorod arrays embedded in ZnO epilayers*, Applied physics letters, **84**, 3241-3243 (2004).

26. M. Araki, H. Koyama and N. Koshida, *Controlled electroluminescence spectra of porous silicon diodes with a vertical optical cavity*, Applied physics letters, **69**, 2956-2958 (1996).

27. H. Yokoyama, K. Nishi, T. Anan, H. Yamada, S. Brorson and E. Ippen, *Enhanced spontaneous emission from GaAs quantum wells in monolithic microcavities*, Applied physics letters, **57**, 2814-2816 (1990).

28. D. C. Look, *Recent advances in ZnO materials and devices*, Materials Science and Engineering: B, **80**, 383-387 (2001).

29. S. B. Ogale, *Thin films and heterostructures for oxide electronics*, Springer Science & Business Media, (2006).

30. J. Ye, S. Gu, S. Zhu, S. Liu, R. Zhang, Y. Shi and Y. Zheng, *Electroluminescent and transport mechanisms of n-ZnO/p-Si heterojunctions*, Applied physics letters, **88**, 182112-182112-182113 (2006).

31. Y. I. Alivov, J. Van Nostrand, D. C. Look, M. Chukichev and B. Ataev, *Observation of 430 nm electroluminescence from ZnO/GaN heterojunction light-emitting diodes*, Applied physics letters, **83**, 2943-2945 (2003).

32. M. S. Silberberg, R. Duran, C. G. Haas and A. D. Norman, *Chemistry: The molecular nature of matter and change*, McGraw-Hill New York, (2006).

33. P. Lawaetz, *Stability of the wurtzite structure*, Physical Review B, **5**, 4039 (1972).

34. Y. Varshni, *Temperature dependence of the energy gap in semiconductors*, Physica, **34**, 149-154 (1967).

35. U. Rössler, *Energy bands of hexagonal II-VI semiconductors*, Physical Review, **184**, 733 (1969).

36. D. C. Look, B. Claflin, Y. I. Alivov and S.-J. Park, *The future of ZnO light emitters*, Physica Status Solidi-A-Applied Research, **201**, 2203-2212 (2004).

37. C.-L. Zhang, W.-N. Zhou, Y. Hang, Z. Lü, H.-D. Hou, Y.-B. Zuo, S.-J. Qin, F.-H. Lu and S.-L. Gu, *Hydrothermal growth and characterization of ZnO crystals*, Journal of Crystal Growth, **310**, 1819-1822 (2008).

38. W. Shan, B. Little, A. Fischer, J. Song, B. Goldenberg, W. Perry, M. Bremser and R. Davis, *Binding energy for the intrinsic excitons in wurtzite GaN*, Physical Review B, **54**, 16369 (1996).

39. M. Lannoo, *Point defects in semiconductors I: theoretical aspects*, Springer Science & Business Media, (2012).

40. S. T. Pantelides, *Deep centers in semiconductors*, CRC Press, (1992).

41. A. Janotti and C. G. Van de Walle, *Native point defects in ZnO*, Physical Review B, **76**, 165202 (2007).

42. C. G. Van de Walle and J. Neugebauer, *First-principles calculations for defects and impurities: Applications to III-nitrides*, Journal of Applied Physics, **95**, 3851-3879 (2004).

43. C. F. Klingshirn, A. Waag, A. Hoffmann and J. Geurts, *Zinc oxide: from fundamental properties towards novel applications*, Springer Science & Business Media, (2010).

44. B. Meyer, H. Alves, D. Hofmann, W. Kriegseis, D. Forster, F. Bertram, J. Christen, A. Hoffmann, M. Straßburg and M. Dworzak, *Bound exciton and donor–acceptor pair recombinations in ZnO*, physica status solidi (b), **241**, 231-260 (2004).

45. L. E. Greene, M. Law, J. Goldberger, F. Kim, J. C. Johnson, Y. Zhang, R. J. Saykally and P. Yang, *Low-temperature wafer-scale production of ZnO nanowire arrays*, Angewandte Chemie International Edition, **42**, 3031-3034 (2003).

46. M. Gomi, N. Oohira, K. Ozaki and M. Koyano, *Photoluminescent and structural properties of precipitated ZnO fine particles*, Japanese Journal of Applied Physics, **42**, 481 (2003).

47. L. Wu, Y. Wu, X. Pan and F. Kong, *Synthesis of ZnO nanorod and the annealing effect on its photoluminescence property*, Optical Materials, **28**, 418-422 (2006).

48. A. Djurišić, Y. Leung, K. Tam, Y. Hsu, L. Ding, W. Ge, Y. Zhong, K. Wong, W. Chan and H. Tam, *Defect emissions in ZnO nanostructures*, Nanotechnology, **18**, 095702 (2007).

49. N. Alvi, K. Ul Hasan, O. Nur and M. Willander, *The origin of the red emission in n-ZnO nanotubes/p-GaN white light emitting diodes*, Nanoscale research letters, **6**, 1-7 (2011).

50. B. Lin, Z. Fu and Y. Jia, *Green luminescent center in undoped zinc oxide films deposited on silicon substrates*, Applied physics letters, **79**, 943-945 (2001).

51. M. Liu, A. Kitai and P. Mascher, *Point defects and luminescence centres in zinc oxide and zinc oxide doped with manganese*, Journal of Luminescence, **54**, 35-42 (1992).

52. D. Li, Y. Leung, A. Djurišić, Z. Liu, M. Xie, S. Shi, S. Xu and W. Chan, *Different origins of visible luminescence in ZnO nanostructures fabricated by the chemical and evaporation methods*, Applied physics letters, **85**, 1601-1603 (2004).

53. K. Maeda, M. Sato, I. Niikura and T. Fukuda, *Growth of 2 inch ZnO bulk single crystal by the hydrothermal method*, Semiconductor science and technology, **20**, S49 (2005).

54. C. Rauch, W. Gehlhoff, M. Wagner, E. Malguth, G. Callsen, R. Kirste, B. Salameh, A. Hoffmann, S. Polarz and Y. Aksu, *Lithium related deep and shallow acceptors in Li-doped ZnO nanocrystals*, Journal of Applied Physics, **107**, 024311 (2010).

55. R. Cox, D. Block, A. Hervé, R. Picard, C. Santier and R. Helbig, *Exchange broadened, optically detected ESR spectra for luminescent donor-acceptor pairs in li doped ZnO*, Solid State Communications, **25**, 77-80 (1978).

56. K. Vanheusden, C. Seager, W. t. Warren, D. Tallant and J. Voigt, *Correlation between photoluminescence and oxygen vacancies in ZnO phosphors*, Applied physics letters, **68**, 403-405 (1996).

57. D. C. Reynolds, D. C. Look, B. Jogai and H. Morkoc, *Similarities in the bandedge and deep-centre photoluminescence mechanisms of ZnO and GaN*, Solid State Communications, **101**, 643-646 (1997).

58. R. Dingle, *Luminescent transitions associated with divalent copper impurities and the green emission from semiconducting zinc oxide*, Physical review letters, **23**, 579 (1969).

59. K. Vanheusden, W. Warren, C. Seager, D. Tallant, J. Voigt and B. Gnade, *Mechanisms behind green photoluminescence in ZnO phosphor powders*, Journal of Applied Physics, **79**, 7983-7990 (1996).

60. R. Kuhnert and R. Helbig, *Vibronic structure of the green photoluminescence due to copper impurities in ZnO*, Journal of Luminescence, **26**, 203-206 (1981).

61. X. Wang, L. Vlasenko, S. Pearton, W. Chen and I. A. Buyanova, *Oxygen and zinc vacancies in as-grown ZnO single crystals*, Journal of Physics D: Applied Physics, **42**, 175411 (2009).

62. O. Neitzke, A. Morfa, J. Wolters, A. W. Schell, G. n. Kewes and O. Benson, *Investigation of Line Width Narrowing and Spectral Jumps of Single Stable Defect Centers in ZnO at Cryogenic Temperature*, Nano letters (2015).

63. I. Aharonovich, S. Castelletto, D. Simpson, C. Su, A. Greentree and S. Prawer, *Diamond-based single-photon emitters*, Reports on progress in Physics, **74**, 076501 (2011).

64. I. Aharonovich, S. Castelletto, D. Simpson, A. Greentree and S. Prawer, *Photophysics of chromium-related diamond single-photon emitters*, Physical Review A, **81**, 043813 (2010).

65. Y. Shen, T. M. Sweeney and H. Wang, *Zero-phonon linewidth of single nitrogen vacancy centers in diamond nanocrystals*, Physical Review B, **77**, 033201 (2008).

66. J. Serrano, F. Manjón, A. Romero, A. Ivanov, M. Cardona, R. Lauck, A. Bosak and M. Krisch, *Phonon dispersion relations of zinc oxide: Inelastic neutron scattering and ab initio calculations*, Physical Review B, **81**, 174304 (2010).

67. J. Wolters, N. Sadzak, A. W. Schell, T. Schröder and O. Benson, *Measurement of the ultrafast spectral diffusion of the optical transition of nitrogen vacancy centers in nano-size diamond using correlation interferometry*, Physical review letters, **110**, 027401 (2013).

68. Z. Zhang, H. Yuan, Y. Gao, J. Wang, D. Liu, J. Shen, L. Liu, W. Zhou, S. Xie and X. Wang, *Large-scale synthesis and optical behaviors of ZnO tetrapods*, Applied physics letters, **90**, 153116-153116-153113 (2007).

69. P. Yang, H. Yan, S. Mao, R. Russo, J. Johnson, R. Saykally, N. Morris, J. Pham, R. He and H.-J. Choi, *Controlled growth of ZnO nanowires and their optical properties*, Advanced Functional Materials, **12**, 323 (2002).

70. B. Wang, X. Jin, H. Wu and Z. Zheng, *Whispering gallery and Fabry–Pérot modes enhanced luminescence from individual ZnO micro mushroom*, Journal of Applied Physics, **113**, 034313 (2013).

71. E. Peter, P. Senellart, D. Martrou, A. Lemaître, J. Hours, J. Gérard and J. Bloch, *Exciton-photon strong-coupling regime for a single quantum dot embedded in a microcavity*, Physical review letters, **95**, 067401 (2005).

72. P. T. Snee, Y. Chan, D. G. Nocera and M. G. Bawendi, *Whispering-Gallery-Mode Lasing from a Semiconductor Nanocrystal/Microsphere Resonator Composite*, Advanced Materials, **17**, 1131-1136 (2005).

73. R. Chen, B. Ling, X. W. Sun and H. D. Sun, *Room Temperature Excitonic Whispering Gallery Mode Lasing from High-Quality Hexagonal ZnO Microdisks*, Advanced Materials, **23**, 2199-2204 (2011).

74. J. Dai, C. Xu, K. Zheng, C. Lv and Y. Cui, *Whispering gallery-mode lasing in ZnO microrods at room temperature*, Applied physics letters, **95**, 241110 (2009).

75. X. Zhang, X. Zhang, J. Xu, X. Shan, J. Xu and D. Yu, *Whispering gallery modes in single triangular ZnO nanorods*, Optics letters, **34**, 2533-2535 (2009).

76. T. Nobis, E. M. Kaidashev, A. Rahm, M. Lorenz and M. Grundmann, *Whispering gallery modes in nanosized dielectric resonators with hexagonal cross section*, Physical review letters, **93**, 103903 (2004).

77. T. Nobis, A. Rahm, C. Czekalla, M. Lorenz and M. Grundmann, *Optical whispering gallery modes in dodecagonal zinc oxide microcrystals*, Superlattices and Microstructures, **42**, 333-336 (2007).

78. R. S. Moirangthem, P.-J. Cheng, P. C.-H. Chien, B. T. H. Ngo, S.-W. Chang, C.-H. Tien and Y.-C. Chang, *Optical cavity modes of a single crystalline zinc oxide microsphere*, Optics express, **21**, 3010-3020 (2013).

79. D. J. Gargas, M. C. Moore, A. Ni, S.-W. Chang, Z. Zhang, S.-L. Chuang and P. Yang, *Whispering gallery mode lasing from zinc oxide hexagonal nanodisks*, ACS nano, **4**, 3270-3276 (2010).

80. Y. Yang, J. Dong, N. Wang and G. Yang, *Whispering gallery mode enhanced luminescence from an individual ZnO micro-and nanoscaled optical resonator*, Journal of Applied Physics, **109**, 093511 (2011).

81. J. Liu, Q. M. Ngo, K. H. Park, S. Kim, Y. H. Ahn, J.-Y. Park, K. H. Koh and S. Lee, *Optical waveguide and cavity effects on whispering-gallery mode resonances in a ZnO nanonail*, Applied physics letters, **95**, 221105 (2009).

82. D. Wang, H. Seo, C.-C. Tin, M. Bozack, J. Williams, M. Park and Y. Tzeng, *Lasing in whispering gallery mode in ZnO nanonails*, Journal of Applied Physics, **99**, 093112-093112-093114 (2006).

83. J. Liu, S. Lee, Y. Ahn, J.-Y. Park, K. H. Koh and K. H. Park, *Identification of dispersion-dependent hexagonal cavity modes of an individual ZnO nanonail*, Applied physics letters, **92**, 263102 (2008).

84. C. Czekalla, C. Sturm, R. Schmidt-Grund, B. Cao, M. Lorenz and M. Grundmann, *Whispering gallery mode lasing in zinc oxide microwires*, Applied physics letters, **92**, 241102 (2008).

85. G. Dai, Y. Zhang, R. Liu, Q. Wan, Q. Zhang, A. Pan and B. Zou, *Visible whispering-gallery modes in ZnO microwires with varied cross sections*, Journal of Applied Physics, **110**, 033101 (2011).

86. H. Dong, Z. Chen, L. Sun, W. Xie, H. H. Tan, J. Lu, C. Jagadish and X. Shen, *Single-crystalline hexagonal ZnO microtube optical resonators*, Journal of Materials Chemistry, **20**, 5510-5515 (2010).

87. J. Dai, C. Xu, R. Ding, K. Zheng, Z. Shi, C. Lv and Y. Cui, *Combined whispering gallery mode laser from hexagonal ZnO microcavities*, Applied physics letters, **95**, 191117 (2009).

88. S. S. Kim, Y.-J. Kim, G.-C. Yi and H. Cheong, *Whispering-gallery-modelike resonance of luminescence from a single hexagonal ZnO microdisk*, Journal of Applied Physics, **106**, 094310 (2009).

89. Y. Yang, Y. Zhang, N. Wang, C. Wang, B. Li and G. Yang, *ZnO nanocone: Application in fabrication of the smallest whispering gallery optical resonator*, Nanoscale, **3**, 592-597 (2011).

90. C. Kim, Y.-J. Kim, E.-S. Jang, G.-C. Yi and H. H. Kim, *Whispering-gallery-modelike-enhanced emission from ZnO nanodisk*, (2006).

91. T. Voss, G. T. Svacha, E. Mazur, S. Müller, C. Ronning, D. Konjhodzic and F. Marlow, *High-order waveguide modes in ZnO nanowires*, Nano letters, **7**, 3675-3680 (2007).

92. H.-Y. Li, S. Ruhle, R. Khedoe, A. Koenderink and D. Vanmaekelbergh, *Polarization, microscopic origin, and mode structure of luminescence and lasing from single ZnO nanowires*, Nano letters, **9**, 3515-3520 (2009).

93. S. H. Lee, T. Goto, H. Miyazaki, J. Chang and T. Yao, *Optical resonant cavity in a nanotaper*, Nano letters, **10**, 2038-2042 (2010).

94. X. Xu, F. S. Brossard, D. A. Williams, D. P. Collins, M. J. Holmes, R. A. Taylor and X. Zhang, *Cavity modes of tapered ZnO nanowires*, New Journal of Physics, **12**, 083052 (2010).

95. M. A. Zimmler, J. Bao, F. Capasso, S. Müller and C. Ronning, *Laser action in nanowires: Observation of the transition from amplified spontaneous emission to laser oscillation*, Applied physics letters, **93**, 051101 (2008).

96. H. Dong, S. Sun, L. Sun, W. Zhou, L. Zhou, X. Shen, Z. Chen, J. Wang and L. Zhang, *Thermodynamic-effect-induced growth, optical modulation and UV lasing of hierarchical ZnO Fabry–Pérot resonators*, Journal of Materials Chemistry, **22**, 3069-3074 (2012).

97. S. Rühle, L. Van Vugt, H.-Y. Li, N. Keizer, L. Kuipers and D. Vanmaekelbergh, *Nature of sub-band gap luminescent eigenmodes in a ZnO nanowire*, Nano letters, **8**, 119-123 (2008).

98. D. Thomas, *The exciton spectrum of zinc oxide*, Journal of Physics and Chemistry of Solids, **15**, 86-96 (1960).

99. M. Zamfirescu, A. Kavokin, B. Gil, G. Malpuech and M. Kaliteevski, *ZnO as a material mostly adapted for the realization of room-temperature polariton lasers*, Physical Review B, **65**, 161205 (2002).

100. J. Hopfield and D. Thomas, *Polariton absorption lines*, Physical review letters, **15**, 22 (1965).

101. C. F. Klingshirn, *Semiconductor optics*, Springer Science & Business Media, (2012).

102. J. Lagois, *Depth-dependent eigenenergies and damping of excitonic polaritons near a semiconductor surface*, Physical Review B, **23**, 5511 (1981).

103. A. Toropov, O. Nekrutkina, T. Shubina, T. Gruber, C. Kirchner, A. Waag, K. Karlsson, P.-O. Holtz and B. Monemar, *Temperature-dependent exciton polariton photoluminescence in ZnO films*, Physical Review B, **69**, 165205 (2004).

104. L. K. van Vugt, S. Rühle, P. Ravindran, H. C. Gerritsen, L. Kuipers and D. Vanmaekelbergh, *Exciton polaritons confined in a ZnO nanowire cavity*, Physical review letters, **97**, 147401 (2006).

105. L. Sun, Z. Chen, Q. Ren, K. Yu, L. Bai, W. Zhou, H. Xiong, Z. Q. Zhu and X. Shen, *Direct observation of whispering gallery mode polaritons and their dispersion in a ZnO tapered microcavity*, Physical review letters, **100**, 156403 (2008).

106. L. Sun, Z. Chen, Q. Ren, K. Yu, W. Zhou, L. Bai, Z. Zhu and X. Shen, *Polarized photoluminescence study of whispering gallery mode polaritons in ZnO microcavity*, physica status solidi (c), **6**, 133-136 (2009).

107. J. Dai, C. Xu, X. Sun and X. Zhang, *Exciton-polariton microphotoluminescence and lasing from ZnO whispering-gallery mode microcavities*, Applied physics letters, **98**, 161110 (2011).

108. L. Sun, H. Dong, W. Xie, Z. An, X. Shen and Z. Chen, *Quasi-whispering gallery modes of exciton-polaritons in a ZnO microrod*, Optics express, **18**, 15371-15376 (2010).

109. C. Xu, X. W. Sun, C. Yuen, B. Chen, S. Yu and Z. L. Dong, *Ultraviolet amplified spontaneous emission from self-organized network of zinc oxide nanofibers*, Applied physics letters, **86**, 011118 (2005).

110. Y. T. Shih, M. K. Wu, W. C. Li, H. Kuan, J. R. Yang, M. Shiojiri and M. J. Chen, *Amplified spontaneous emission from ZnO in n-ZnO/ZnO nanodots–SiO2 composite/p-AlGaN heterojunction light-emitting diodes*, Nanotechnology, **20**, 165201 (2009).

111. C. Czekalla, T. Nobis, A. Rahm, B. Cao, J. Zúñiga-Pérez, C. Sturm, R. Schmidt-Grund, M. Lorenz and M. Grundmann, *Whispering gallery modes in zinc oxide micro-and nanowires*, physica status solidi (b), **247**, 1282-1293 (2010).

112. B. Y. Lee, M. G. Sung, H. Lee, S. Namgung, S. Y. Park, D. S. Choi and S. Hong, *Integrated devices based on networks of nanotubes and nanowires*, NPG Asia Materials, **2**, 103-111 (2010).

113. F. Xu, Y. Shen, L. Sun, H. Zeng and Y. Lu, *Enhanced photocatalytic activity of hierarchical ZnO nanoplate-nanowire architecture as environmentally safe and facilely recyclable photocatalyst*, Nanoscale, **3**, 5020-5025 (2011).

114. H. Cao, J. Y. Xu, Y. Ling, A. L. Burin, E. W. Seeling, X. Liu and R. P. Chang, *Random lasers with coherent feedback*, Selected Topics in Quantum Electronics, IEEE Journal of, **9**, 111-119 (2003).

115. S. Yu, C. Yuen, S. Lau, Y. Wang, H. Lee and B. Tay, *Ultraviolet amplified spontaneous emission from zinc oxide ridge waveguides on silicon substrate*, Applied physics letters, **83**, 4288-4290 (2003).

116. H. Cao, Y. Zhao, S. Ho, E. Seelig, Q. Wang and R. Chang, *Random laser action in semiconductor powder*, Physical review letters, **82**, 2278 (1999).

117. Z. Tang, G. K. Wong, P. Yu, M. Kawasaki, A. Ohtomo, H. Koinuma and Y. Segawa, *Room-temperature ultraviolet laser emission from self-assembled ZnO microcrystallite thin films*, Applied physics letters, **72**, 3270-3272 (1998).

118. M. H. Huang, S. Mao, H. Feick, H. Yan, Y. Wu, H. Kind, E. Weber, R. Russo and P. Yang, *Room-temperature ultraviolet nanowire nanolasers*, Science, **292**, 1897-1899 (2001).

119. Y.-Y. Lai, J.-W. Chen, T.-C. Chang, Y.-H. Chou and T.-C. Lu, *Manipulation of exciton and photon lasing in a membrane-type ZnO microcavity*, Applied physics letters, **106**, 131106 (2015).

120. H. Yan, J. Johnson, M. Law, R. He, K. Knutsen, J. R. McKinney, J. Pham, R. Saykally and P. Yang, *ZnO nanoribbon microcavity lasers*, Advanced Materials, **15**, 1907-1911 (2003).

121. L. K. Van Vugt, S. Rühle and D. Vanmaekelbergh, *Phase-correlated nondirectional laser emission from the end facets of a ZnO nanowire*, Nano letters, **6**, 2707-2711 (2006).

122. C. Zhang, Z. Dong, G. You, S. Qian and H. Deng, *Multiphoton route to ZnO nanowire lasers*, Optics letters, **31**, 3345-3347 (2006).

123. R. Hauschild, H. Lange, H. Priller, C. Klingshirn, R. Kling, A. Waag, H. Fan, M. Zacharias and H. Kalt, *Stimulated emission from ZnO nanorods*, Physica Status Solidi B Basic Research, **243**, 753 (2006).

124. J. M. Szarko, J. K. Song, C. W. Blackledge, I. Swart, S. R. Leone, S. Li and Y. Zhao, *Optical injection probing of single ZnO tetrapod lasers*, Chemical physics letters, **404**, 171-176 (2005).

125. Y. Leung, W. Kwok, A. Djurišić, D. Phillips and W. Chan, *Time-resolved study of stimulated emission in ZnO tetrapod nanowires*, Nanotechnology, **16**, 579 (2005).

126. K. Govender, D. S. Boyle, P. O'Brien, D. Binks, D. West and D. Coleman, *Room-temperature lasing observed from ZnO nanocolumns grown by aqueous solution deposition*, Advanced Materials, **14**, 1221-1224 (2002).

127. M. Berry, N. Bloembergen, N. Erez, D. Greenberger and E. Wolf, *Progress in Optics*, Elsevier, (2007).

128. D. S. Wiersma, *The physics and applications of random lasers*, Nature physics, **4**, 359-367 (2008).

129. H. Cao, Y. Zhao, H. Ong, S. Ho, J. Dai, J. Wu and R. Chang, *Ultraviolet lasing in resonators formed by scattering in semiconductor polycrystalline films*, Applied physics letters, **73**, 3656-3658 (1998).

130. J. Fallert, R. J. Dietz, J. Sartor, D. Schneider, C. Klingshirn and H. Kalt, *Co-existence of strongly and weakly localized random laser modes*, Nature Photonics, **3**, 279-282 (2009).

131. S. P. Lau, H. Yang, S. F. Yu, C. Yuen, E. S. Leong, H. Li and H. H. Hng, *Flexible ultraviolet random lasers based on nanoparticles*, Small, **1**, 956-959 (2005).

132. H. Cao, J. Xu, E. Seelig and R. Chang, *Microlaser made of disordered media*, Applied physics letters, **76**, 2997-2999 (2000).

133. S. Choi, A. M. Berhane, A. Gentle, C. Ton-That, M. R. Phillips and I. Aharonovich, *Electroluminescence from Localized Defects in Zinc Oxide: Toward Electrically Driven Single Photon Sources at Room Temperature*, ACS applied materials & interfaces, **7**, 5619-5623 (2015).

134. H. Ohta, K.-i. Kawamura, M. Orita, M. Hirano, N. Sarukura and H. Hosono, *Current injection emission from a transparent p–n junction composed of p-SrCu2O2/n-ZnO*, Applied physics letters, **77**, 475-477 (2000).

135. M. C. Jeong, B. Y. Oh, M. H. Ham, S. W. Lee and J. M. Myoung, *ZnO-Nanowire-Inserted GaN/ZnO Heterojunction Light-Emitting Diodes*, Small, **3**, 568-572 (2007).

136. H.-C. Chen, M.-J. Chen, M.-K. Wu, W.-C. Li, H.-L. Tsai, J.-R. Yang, H. Kuan and M. Shiojiri, *UV electroluminescence and structure of n-ZnO/p-GaN heterojunction LEDs grown by atomic layer deposition*, Quantum Electronics, IEEE Journal of, **46**, 265-271 (2010).

137. Z. Kyaw, W. Jianxiong, K. Dev, S. T. Tan, Z. Ju, Z.-H. Zhang, Y. Ji, N. Hasanov, W. Liu and X. W. Sun, *Room-temperature larger-scale highly ordered nanorod imprints of ZnO film*, Optics express, **21**, 26846-26853 (2013).

138. J. You, X. Zhang, S. Zhang, H. Tan, J. Ying, Z. Yin, Q. Zhu and P. K. Chu, *Electroluminescence behavior of ZnO/Si heterojunctions: Energy band alignment and interfacial microstructure*, Journal of Applied Physics, **107**, 083701 (2010).

139. J. Bao, M. A. Zimmler, F. Capasso, X. Wang and Z. Ren, *Broadband ZnO single-nanowire light-emitting diode*, Nano letters, **6**, 1719-1722 (2006).

140. O. Lupan, T. Pauporte and B. Viana, *Low-Voltage UV-Electroluminescence from ZnO-Nanowire Array/p-GaN Light-Emitting diodes*, Advanced Materials, **22**, 3298-3302 (2010).

141. J. Mares, M. Falanga, A. Thompson, A. Osinsky, J. Xie, B. Hertog, A. Dabiran, P. Chow, S. Karpov and W. Schoenfeld, *Hybrid CdZnO/GaN quantum-well light emitting diodes*, Journal of Applied Physics, **104**, 093107 (2008).

142. A. Osinsky, J. Dong, M. Kauser, B. Hertog, A. Dabiran, P. Chow, S. Pearton, O. Lopatiuk and L. Chernyak, *MgZnO/AlGaN heterostructure light-emitting diodes*, Applied physics letters, **85**, 4272 (2004).

143. W. I. Park and G. C. Yi, *Electroluminescence in n-ZnO Nanorod Arrays Vertically Grown on p-GaN*, Advanced Materials, **16**, 87-90 (2004).

144. P. Klason, M. Rahman, Q.-H. Hu, O. Nur, R. Turan and M. Willander, *Fabrication and characterization of p-Si/n-ZnO heterostructured junctions*, Microelectronics Journal, **40**, 706-710 (2009).

145. H. Chen, M. Chen, Y. Huang, W. Sun, W. Li, J. Yang, H. Kuan and M. Shiojiri, *White-light electroluminescence from n-ZnO/p-GaN heterojunction light-emitting diodes at reverse breakdown bias*, Electron Devices, IEEE Transactions on, **58**, 3970-3975 (2011).

146. N. Alvi, S. U. Ali, S. Hussain, O. Nur and M. Willander, *Fabrication and comparative optical characterization of n-ZnO nanostructures (nanowalls, nanorods,*

nanoflowers and nanotubes)/p-GaN white-light-emitting diodes, Scripta Materialia, **64**, 697-700 (2011).

147. J. Dai, C. X. Xu and X. W. Sun, *ZnO-Microrod/p-GaN Heterostructured Whispering-Gallery-Mode Microlaser Diodes*, Advanced Materials, **23**, 4115-4119 (2011).

148. W. Lee, M.-C. Jeong and J.-M. Myoung, *Evolution of the morphology and optical properties of ZnO nanowires during catalyst-free growth by thermal evaporation*, Nanotechnology, **15**, 1441 (2004).

149. Y. Yan, X. Wang, H. Chen, L. Zhou, X. Cao and J. Zhang, *Synthesis of ZnO nanotowers controlled by a reagent's vapour pressure*, Journal of Physics D: Applied Physics, **46**, 155304 (2013).

150. C. G. Van de Walle, *Hydrogen as a cause of doping in zinc oxide*, Physical review letters, **85**, 1012 (2000).

151. J. Goldstein, D. E. Newbury, P. Echlin, D. C. Joy, A. D. Romig Jr, C. E. Lyman, C. Fiori and E. Lifshin, *Scanning electron microscopy and X-ray microanalysis: a text for biologists, materials scientists, and geologists*, Springer Science & Business Media, (2012).

152. M. R. Phillips, *Cathodoluminescence microscopy and spectroscopy of opto-electronic materials*, Microchimica Acta, **155**, 51-58 (2006).

153. https://www.auburn.edu/~duinedu/epr/1_theory.pdf.

154. A. Kohan, G. Ceder, D. Morgan and C. G. Van de Walle, *First-principles study of native point defects in ZnO*, Physical Review B, **61**, 15019 (2000).

155. N. Garces, L. Wang, L. Bai, N. Giles, L. Halliburton and G. Cantwell, *Role of copper in the green luminescence from ZnO crystals*, Applied physics letters, **81**, 622-624 (2002).

156. H. Yang, S. Lau, S. Yu, A. Abiyasa, M. Tanemura, T. Okita and H. Hatano, *High-temperature random lasing in ZnO nanoneedles*, Applied physics letters, **89**, 011103-011103-011103 (2006).

157. Y. Gu, I. L. Kuskovsky, M. Yin, S. Obrien and G. Neumark, *Quantum confinement in ZnO nanorods*, Applied physics letters, **85**, 3833-3835 (2004).

158. S. Polarz, A. Roy, M. Merz, S. Halm, D. Schröder, L. Schneider, G. Bacher, F. E. Kruis and M. Driess, *Chemical Vapor Synthesis of Size-Selected Zinc Oxide Nanoparticles*, Small, **1**, 540-552 (2005).

159. R. K. Sendi and S. Mahmud, *Impact of sintering temperature on the structural, electrical, and optical properties of doped ZnO nanoparticle-based discs*, Applied Surface Science, **261**, 128-136 (2012).

160. B. E. Warren, *X-ray Diffraction*, Courier Corporation, (1969).

161. R. Yogamalar, R. Srinivasan, A. Vinu, K. Ariga and A. C. Bose, *X-ray peak broadening analysis in ZnO nanoparticles*, Solid State Communications, **149**, 1919-1923 (2009).

162. B. G. Yacobi and D. B. Holt, *Cathodoluminescence microscopy of inorganic solids*, Springer, (1990).

163. Y. Chen, G. Kothiyal, J. Singh and P. K. Bhattacharya, *Absorption and photoluminescence studies of the temperature dependence of exciton life time in lattice-matched and strained quantum well systems*, Superlattices and Microstructures, **3**, 657-664 (1987).

164. A. Pöppl and G. Völkel, *ESR and Photo-ESR Investigations of Zinc Vacancies and Interstitial Oxygen Ions in Undoped ZnO Ceramics*, physica status solidi (a), **125**, 571-581 (1991).

165. A. B. Djurišić, Y. H. Leung, W. C. Choy, K. W. Cheah and W. K. Chan, *Visible photoluminescence in ZnO tetrapod and multipod structures*, Applied physics letters, **84**, 2635-2637 (2004).

166. C. Geisler and G. Simmons, *High temperature induced EPR signals in zinc oxide*, Physics Letters, **11**, 111-112 (1964).

167. G. Neumann, in *Current Topics in Materials Science*, edited by E. Kaldis, North-Holland, Amsterdam, 1981, pp. 269.

168. L. Larina, N. Tsvetkov, J. Yang, K.-S. Lim and O. Shevaleevskiy, *Electron paramagnetic resonance studies of shallow donors behavior in hydrogenated ZnO films*, ECS Transactions, **28**, 161-167 (2010).

169. J. Smith and W. Vehse, *ESR of electron irradiated ZnO confirmation of the F< sup>+</sup> center*, Physics Letters A, **31**, 147-148 (1970).

170. P. Erhart and K. Albe, *Diffusion of zinc vacancies and interstitials in zinc oxide*, Applied physics letters, **88**, 201918 (2006).

171. G. Neumann, in *Current Topics in Materials Science*, edited by E. Kaldis, North-Holland , Amsterdam, 1981, pp. 279.

172. D. Galland and A. Herve, *ESR spectra of the zinc vacancy in ZnO*, Physics Letters A, **33**, 1-2 (1970).

173. L. Hu, J. Huang, H. He, L. Zhu, S. Liu, Y. Jin, L. Sun and Z. Ye, *Dual-donor (Zn i and VO) mediated ferromagnetism in copper-doped ZnO micron-scale polycrystalline films: a thermally driven defect modulation process*, Nanoscale, **5**, 3918-3930 (2013).

174. D. M. Murphy, in *Metal Oxide Catalysis*, edited by S. D. Jackson and J. S. J. Hargreaves, Wiley VCH Verlag GmbH & Co. KGaA, Weinheim, Germany, 2008, pp. 150.

175. J. Chiou, J. Jan, H. Tsai, C. Bao, W.-F. Pong, M.-H. Tsai, I.-H. Hong, R. Klauser, J. Lee and J. Wu, *Electronic structure of ZnO nanorods studied by angle-dependent x-ray absorption spectroscopy and scanning photoelectron microscopy*, Applied physics letters, **84**, 3462-3464 (2004).

176. A. P. Singh, R. Kumar, P. Thakur, N. Brookes, K. Chae and W. Choi, *NEXAFS and XMCD studies of single-phase Co doped ZnO thin films*, Journal of Physics: Condensed Matter, **21**, 185005 (2009).

177. J. Chiou, K. Kumar, J. Jan, H. Tsai, C. Bao, W.-F. Pong, F. Chien, M.-H. Tsai, I.-H. Hong and R. Klauser, *Diameter dependence of the electronic structure of ZnO nanorods determined by x-ray absorption spectroscopy and scanning photoelectron microscopy*, Applied physics letters, **85**, 3220-3222 (2004).

178. C. Dong, C. Persson, L. Vayssieres, A. Augustsson, T. Schmitt, M. Mattesini, R. Ahuja, C. Chang and J.-H. Guo, *Electronic structure of nanostructured ZnO from x-ray absorption and emission spectroscopy and the local density approximation*, Physical Review B, **70**, 195325 (2004).

179. Y. Kim and S. Kang, *Investigation of photoluminescence mechanisms of ZnO through experimental and first-principles calculation methods*, Acta Materialia, **59**, 126-132 (2011).

180. S. Krishnamurthy, C. McGuinness, L. Dorneles, M. Venkatesan, J. Coey, J. Lunney, C. Patterson, K. Smith, T. Learmonth and P.-A. Glans, *Soft-x-ray*

spectroscopic investigation of ferromagnetic Co-doped ZnO, Journal of Applied Physics, **99**, 08M111 (2006).

181. E. Lavrov, J. Weber, F. Börrnert, C. G. Van de Walle and R. Helbig, *Hydrogen-related defects in ZnO studied by infrared absorption spectroscopy*, Physical Review B, **66**, 165205 (2002).

182. G. Xing, X. Fang, Z. Zhang, D. Wang, X. Huang, J. Guo, L. Liao, Z. Zheng, H. Xu and T. Yu, *Ultrathin single-crystal ZnO nanobelts: Ag-catalyzed growth and field emission property*, Nanotechnology, **21**, 255701 (2010).

183. L. Zhang, L. Yin, C. Wang, N. Lun, Y. Qi and D. Xiang, *Origin of visible photoluminescence of ZnO quantum dots: defect-dependent and size-dependent*, The Journal of Physical Chemistry C, **114**, 9651-9658 (2010).

184. A. Van Dijken, J. Makkinje and A. Meijerink, *The influence of particle size on the luminescence quantum efficiency of nanocrystalline ZnO particles*, Journal of Luminescence, **92**, 323-328 (2001).

185. L. L. Lem, M. R. Phillips and C. Ton-That, *Controlling the visible luminescence in hydrothermal ZnO*, Journal of Luminescence, **154**, 387-391 (2014).

186. M. R. Phillips, K. E. McBean, G. McCredie and C. Ton-That, (European Materials Research Society, Warsaw, Poland, 2009).

187. J. Vechten, *Handbook of Semiconductors Vol. 3: Materials and Preparation*, Amsterdam, (1980).

188. M. R. Phillips, H. Telg, S. O. Kucheyev, O. Gelhausen and M. Toth, *Cathodoluminescence efficiency dependence on excitation density in n-type gallium nitride*, Microscopy and Microanalysis, **9**, 144-151 (2003).

189. S. Kucheyev, M. Toth, M. Phillips, J. Williams and C. Jagadish, *Effects of excitation density on cathodoluminescence from GaN*, Applied physics letters, **79**, 2154-2156 (2001).

190. M. Reshchikov and R. Korotkov, *Analysis of the temperature and excitation intensity dependencies of photoluminescence in undoped GaN films*, Physical Review B, **64**, 115205 (2001).

191. R. Singh, R. Molnar, M. Ünlü and T. Moustakas, *Intensity dependence of photoluminescence in GaN thin films*, Applied physics letters, **64**, 336-338 (1994).

192. J. Müllhaüser, O. Brandt, H. Yang and K. Ploog, *Exciton luminescence of single-crystal GaN,* presented at the MRS Proceedings, **395**, 607, (1995).

193. M. Willander, O. Nur, J. R. Sadaf, M. I. Qadir, S. Zaman, A. Zainelabdin, N. Bano and I. Hussain, *Luminescence from zinc oxide nanostructures and polymers and their hybrid devices*, Materials, **3**, 2643-2667 (2010).

194. M. Reshchikov, H. Morkoc, B. Nemeth, J. Nause, J. Xie, B. Hertog and A. Osinsky, *Luminescence properties of defects in ZnO*, Physica B: Condensed Matter, **401**, 358-361 (2007).

195. G. Shambat, B. Ellis, A. Majumdar, J. Petykiewicz, M. A. Mayer, T. Sarmiento, J. Harris, E. E. Haller and J. Vučković, *Ultrafast direct modulation of a single-mode photonic crystal nanocavity light-emitting diode*, Nature communications, **2**, 539 (2011).

196. L. Childress and R. Hanson, *Diamond NV centers for quantum computing and quantum networks*, MRS bulletin, **38**, 134-138 (2013).

197. E. Neu, D. Steinmetz, J. Riedrich-Möller, S. Gsell, M. Fischer, M. Schreck and C. Becher, *Single photon emission from silicon-vacancy colour centres in chemical vapour deposition nano-diamonds on iridium*, New Journal of Physics, **13**, 025012 (2011).

198. T. Müller, C. Hepp, B. Pingault, E. Neu, S. Gsell, M. Schreck, H. Sternschulte, D. Steinmüller-Nethl, C. Becher and M. Atatüre, *Optical signatures of silicon-vacancy spins in diamond*, Nature communications, **5** (2014).

199. M. J. Holmes, K. Choi, S. Kako, M. Arita and Y. Arakawa, *Room-temperature triggered single photon emission from a III-nitride site-controlled nanowire quantum dot*, Nano letters, **14**, 982-986 (2014).

200. S. Castelletto, B. Johnson, V. Ivády, N. Stavrias, T. Umeda, A. Gali and T. Ohshima, *A silicon carbide room-temperature single-photon source*, Nature materials, **13**, 151-156 (2014).

201. F. Li, L. Orosz, O. Kamoun, S. Bouchoule, C. Brimont, P. Disseix, T. Guillet, X. Lafosse, M. Leroux and J. Leymarie, *From excitonic to photonic polariton condensate in a ZnO-based microcavity*, Physical review letters, **110**, 196406 (2013).

202. K. J. Pooley, J. H. Joo and E. L. Hu, *Constrained, aqueous growth of three-dimensional single crystalline zinc oxide structures*, APL Materials, **2**, 012111 (2014).

203. A. Menzel, K. Subannajui, F. Güder, D. Moser, O. Paul and M. Zacharias, *Multifunctional ZnO-Nanowire-Based Sensor*, Advanced Functional Materials, **21**, 4342-4348 (2011).

204. T.-T. Cuong and W. Leigh, *Characteristics of point defects in the green luminescence from Zn-and O-rich ZnO*, (2012).

205. C. Bradac, T. Gaebel, N. Naidoo, M. Sellars, J. Twamley, L. Brown, A. Barnard, T. Plakhotnik, A. Zvyagin and J. Rabeau, *Observation and control of blinking nitrogen-vacancy centres in discrete nanodiamonds*, Nature nanotechnology, **5**, 345-349 (2010).

206. P. Siyushev, V. Jacques, I. Aharonovich, F. Kaiser, T. Müller, L. Lombez, M. Atatüre, S. Castelletto, S. Prawer and F. Jelezko, *Low-temperature optical characterization of a near-infrared single-photon emitter in nanodiamonds*, New Journal of Physics, **11**, 113029 (2009).

207. K.-M. Fu, C. Santori, P. Barclay and R. Beausoleil, *Conversion of neutral nitrogen-vacancy centers to negatively charged nitrogen-vacancy centers through selective oxidation*, Applied physics letters, **96**, 121907 (2010).

208. B. Grotz, M. V. Hauf, M. Dankerl, B. Naydenov, S. Pezzagna, J. Meijer, F. Jelezko, J. Wrachtrup, M. Stutzmann and F. Reinhard, *Charge state manipulation of qubits in diamond*, Nature communications, **3**, 729 (2012).

209. K. Ip, M. Overberg, Y. Heo, D. Norton, S. Pearton, C. Stutz, S. Kucheyev, C. Jagadish, J. Williams and B. Luo, *Hydrogen incorporation, diffusivity and evolution in bulk ZnO*, Solid-State Electronics, **47**, 2255-2259 (2003).

210. P. Lommens, P. F. Smet, C. de Mello Donega, A. Meijerink, L. Piraux, S. Michotte, S. Mátéfi-Tempfli, D. Poelman and Z. Hens, *Photoluminescence properties of Co 2+-doped ZnO nanocrystals*, Journal of Luminescence, **118**, 245-250 (2006).

211. D. Englund, D. Fattal, E. Waks, G. Solomon, B. Zhang, T. Nakaoka, Y. Arakawa, Y. Yamamoto and J. Vučković, *Controlling the spontaneous emission rate of single quantum dots in a two-dimensional photonic crystal*, Physical review letters, **95**, 013904 (2005).

212. C. Santori, D. Fattal, J. Vučković, G. S. Solomon and Y. Yamamoto, *Indistinguishable photons from a single-photon device*, Nature, **419**, 594-597 (2002).

213. S. Deshpande, A. Das and P. Bhattacharya, *Blue single photon emission up to 200 K from an InGaN quantum dot in AlGaN nanowire*, Applied physics letters, **102**, 161114 (2013).

214. I. Aharonovich and E. Neu, *Diamond nanophotonics*, Advanced Optical Materials, **2**, 911-928 (2014).

215. S. Deshpande, T. Frost, A. Hazari and P. Bhattacharya, *Electrically pumped single-photon emission at room temperature from a single InGaN/GaN quantum dot*, Applied physics letters, **105**, 141109 (2014).

216. M. Nothaft, S. Höhla, F. Jelezko, N. Frühauf, J. Pflaum and J. Wrachtrup, *Electrically driven photon antibunching from a single molecule at room temperature*, Nature communications, **3**, 628 (2012).

217. Z. Yuan, B. E. Kardynal, R. M. Stevenson, A. J. Shields, C. J. Lobo, K. Cooper, N. S. Beattie, D. A. Ritchie and M. Pepper, *Electrically driven single-photon source*, Science, **295**, 102-105 (2002).

218. A. Nowak, S. Portalupi, V. Giesz, O. Gazzano, C. Dal Savio, P.-F. Braun, K. Karrai, C. Arnold, L. Lanco and I. Sagnes, *Deterministic and electrically tunable bright single-photon source*, Nature communications, **5** (2014).

219. O. Hayden, A. B. Greytak and D. C. Bell, *Core–Shell Nanowire Light-Emitting Diodes*, Advanced Materials, **17**, 701-704 (2005).

220. F. Qian, Y. Li, S. Gradecak, D. Wang, C. J. Barrelet and C. M. Lieber, *Gallium nitride-based nanowire radial heterostructures for nanophotonics*, Nano letters, **4**, 1975-1979 (2004).

221. C.-Y. Chang, F.-C. Tsao, C.-J. Pan, G.-C. Chi, H.-T. Wang, J.-J. Chen, F. Ren, D. Norton, S. Pearton and K.-H. Chen, *Electroluminescence from ZnO nanowire/polymer composite pn junction*, Applied physics letters, **88**, 173503 (2006).

222. N. Mizuochi, T. Makino, H. Kato, D. Takeuchi, M. Ogura, H. Okushi, M. Nothaft, P. Neumann, A. Gali and F. Jelezko, *Electrically driven single-photon source at room temperature in diamond*, Nature Photonics, **6**, 299-303 (2012).

223. P. Chen, X. Ma and D. Yang, *Ultraviolet electroluminescence from ZnO/p-Si heterojunctions*, Journal of Applied Physics, **101**, 053103-053103-053104 (2007).

224. M.-C. Jeong, B.-Y. Oh, M.-H. Ham and J.-M. Myoung, *Electroluminescence from ZnO nanowires in n-ZnO film/ZnO nanowire array/p-GaN film heterojunction light-emitting diodes*, Applied physics letters, **88**, 202105-202105-202103 (2006).

225. I.-S. Jeong, J. H. Kim and S. Im, *Ultraviolet-enhanced photodiode employing n-ZnO/p-Si structure*, Applied physics letters, **83**, 2946-2948 (2003).

226. S. Mridha and D. Basak, *Ultraviolet and visible photoresponse properties of n-ZnO/p-Si heterojunction*, Journal of Applied Physics, **101**, 083102-083102-083105 (2007).

227. M. Athanasiou, R. Smith, B. Liu and T. Wang, *Room temperature continuous–wave green lasing from an InGaN microdisk on silicon*, Scientific reports, **4** (2014).

228. C. Pan, L. Dong, G. Zhu, S. Niu, R. Yu, Q. Yang, Y. Liu and Z. L. Wang, *High-resolution electroluminescent imaging of pressure distribution using a piezoelectric nanowire LED array*, Nature Photonics, **7**, 752-758 (2013).

229. K. Nomura, H. Ohta, K. Ueda, T. Kamiya, M. Hirano and H. Hosono, *Thin-film transistor fabricated in single-crystalline transparent oxide semiconductor*, Science, **300**, 1269-1272 (2003).

230. D. Zhao, Y. Liu, D. Shen, Y. Lu, L. Zhang and X. Fan, *Structure and photoluminescence properties of ZnO microrods*, Journal of Applied Physics, **94**, 5605-5608 (2003).

231. J. Zapien, Y. Jiang, X. Meng, W. Chen, F. Au, Y. Lifshitz and S. Lee, *Room-temperature single nanoribbon lasers*, Applied physics letters, **84**, 1189-1191 (2004).

232. N. Wang, Y. Yang and G. Yang, *Fabry–Pérot and whispering gallery modes enhanced luminescence from an individual hexagonal ZnO nanocolumn*, Applied physics letters, **97**, 041917 (2010).

233. S. Shopova, G. Farca, A. Rosenberger, W. Wickramanayake and N. Kotov, *Microsphere whispering-gallery-mode laser using< equation>< font face='verdana'> HgTe</equation> quantum dots*, Applied physics letters, **85**, 6101-6103 (2004).

234. H.-Y. Ryu, S.-H. Kim, H.-G. Park, J.-K. Hwang, Y.-H. Lee and J.-S. Kim, *Square-lattice photonic band-gap single-cell laser operating in the lowest-order whispering gallery mode*, Applied physics letters, **80**, 3883-3885 (2002).

235. S. Chang, N. B. Rex, R. K. Chang, G. Chong and L. J. Guido, *Stimulated emission and lasing in whispering-gallery modes of GaN microdisk cavities*, Applied physics letters, **75**, 166-168 (1999).

236. X. Liu, W. Fang, Y. Huang, X. Wu, S. Ho, H. Cao and R. Chang, *Optically pumped ultraviolet microdisk laser on a silicon substrate*, Applied physics letters, **84**, 2488-2490 (2004).

237. H. Dong, Z. Chen, L. Sun, J. Lu, W. Xie, H. H. Tan, C. Jagadish and X. Shen, *Whispering gallery modes in indium oxide hexagonal microcavities*, Applied physics letters, **94**, 173115-173115-173113 (2009).

238. K. Srinivasan, M. Borselli, O. Painter, A. Stintz and S. Krishna, *Cavity Q, mode volume, and lasing threshold in small diameter AlGaAs microdisks with embedded quantum dots*, Optics express, **14**, 1094-1105 (2006).

239. K. Okazaki, T. Shimogaki, K. Fusazaki, M. Higashihata, D. Nakamura, N. Koshizaki and T. Okada, *Ultraviolet whispering-gallery-mode lasing in ZnO micro/nano sphere crystal*, Applied physics letters, **101**, 211105 (2012).

240. M. Willander, L. Yang, A. Wadeasa, S. Ali, M. Asif, Q. Zhao and O. Nur, *Zinc oxide nanowires: controlled low temperature growth and some electrochemical and optical nano-devices*, Journal of Materials Chemistry, **19**, 1006-1018 (2009).

241. Z. Wang, F. Wang, L. Wang, Y. Jia and Q. Sun, *First-principles study of negative thermal expansion in zinc oxide*, Journal of Applied Physics, **114**, 063508 (2013).

242. S.-H. Jeong, J.-K. Kim and B.-T. Lee, *Effects of growth conditions on the emission properties of ZnO films prepared on Si (100) by rf magnetron sputtering*, Journal of Physics D: Applied Physics, **36**, 2017 (2003).

243. H. Fan, R. Scholz, F. Kolb, M. Zacharias, U. Gösele, F. Heyroth, C. Eisenschmidt, T. Hempel and J. Christen, *On the growth mechanism and optical properties of ZnO multi-layer nanosheets*, Applied Physics A, **79**, 1895-1900 (2004).

244. C. Xu and X. Sun, *Characteristics and growth mechanism of ZnO whiskers fabricated by vapor phase transport*, Japanese Journal of Applied Physics, **42**, 4949 (2003).

245. A.-J. Cheng, Y. Tzeng, H. Xu, S. Alur, Y. Wang, M. Park, T.-h. Wu, C. Shannon, D.-J. Kim and D. Wang, *Raman analysis of longitudinal optical phonon-*

plasmon coupled modes of aligned ZnO nanorods, Journal of Applied Physics, **105**, 073104 (2009).

246. T. Jeong, M. Han, C. Youn and Y. Park, *Raman scattering and photoluminescence of As ion-implanted ZnO single crystal*, Journal of Applied Physics, **96**, 175-179 (2004).

247. D. Drouin, A. R. Couture, D. Joly, X. Tastet, V. Aimez and R. Gauvin, *CASINO V2. 42-A fast and easy-to-use modeling tool for scanning electron microscopy and microanalysis users*, Scanning, **29**, 92-101 (2007).

248. M. Foley, C. Ton-That and M. R. Phillips, *Cathodoluminescence inhomogeneity in ZnO nanorods*, Applied physics letters, **93**, 243104-243104-243103 (2008).

249. W. Dake and R. Nicholas, *Photoluminescence of Zinc Oxide nanowires: the effect of surface band bending*, ISRN Condensed Matter Physics, **2012** (2012).

250. D. Reynolds, D. C. Look and B. Jogai, *Fine structure on the green band in ZnO*, Journal of Applied Physics, **89**, 6189-6191 (2001).

251. V. Ursaki, A. Burlacu, E. Rusu, V. Postolake and I. Tiginyanu, *Whispering gallery modes and random lasing in ZnO microstructures*, Journal of Optics A: Pure and Applied Optics, **11**, 075001 (2009).

252. X. Sun and H. Kwok, *Optical properties of epitaxially grown zinc oxide films on sapphire by pulsed laser deposition*, Journal of Applied Physics, **86**, 408-411 (1999).

253. A. K. Bhowmik, *Polygonal optical cavities*, Applied optics, **39**, 3071-3075 (2000).

254. Y.-J. Zeng, Z.-Z. Ye, W.-Z. Xu, L.-P. Zhu and B.-H. Zhao, *Well-aligned ZnO nanowires grown on Si substrate via metal–organic chemical vapor deposition*, Applied Surface Science, **250**, 280-283 (2005).

255. I. Konidakis, M. Androulidaki, G. Zito and S. Pissadakis, *Growth of ZnO nanolayers inside the capillaries of photonic crystal fibres*, Thin Solid Films, **555**, 76-80 (2014).